



HAL
open science

Highly integrated photovoltaic micro-concentrator for space applications

Victor Vareilles

► **To cite this version:**

Victor Vareilles. Highly integrated photovoltaic micro-concentrator for space applications. Electronics. INSA de Lyon, 2023. English. NNT : 2023ISAL0106 . tel-04752155

HAL Id: tel-04752155

<https://theses.hal.science/tel-04752155v1>

Submitted on 24 Oct 2024

HAL is a multi-disciplinary open access archive for the deposit and dissemination of scientific research documents, whether they are published or not. The documents may come from teaching and research institutions in France or abroad, or from public or private research centers.

L'archive ouverte pluridisciplinaire **HAL**, est destinée au dépôt et à la diffusion de documents scientifiques de niveau recherche, publiés ou non, émanant des établissements d'enseignement et de recherche français ou étrangers, des laboratoires publics ou privés.



N°d'ordre NNT : 2023ISAL0106

**THESE de DOCTORAT DE L'INSA LYON,
membre de l'Université de Lyon**

**École Doctorale N° 160
EEA Électronique, Électrotechnique et Automatique**

Spécialité de doctorat : Électronique, micro et nanoélectronique, optique et laser

Soutenue publiquement le 15/12/2023, par :

Victor VAREILLES

**Highly integrated photovoltaic micro-concentrator for
space applications**

**Micro-concentrateur photovoltaïque hautement intégré
pour les applications spatiales**

Devant le jury composé de :

CUMINAL Yvan
KAMINSKI-CACHOPO Anne
DOMINGUEZ-DOMINGUEZ César
RIVALLANT Samuel
AMARA Mohamed
VESCHETTI Yannick

Maître de conférence HDR (IES Montpellier)
Professeure des Universités (Grenoble INP)
Professeur adjoint (IES Madrid)
Professeur des Universités (ISAE Toulouse)
Chargé de recherche HDR (INL, INSA Lyon)
Directeur de recherche HDR (Heliup)

Rapporteur
Rapporteure
Examineur
Examineur
Directeur de thèse
Co-directeur de thèse

HELMERS Henning
VOARINO Philippe

Docteur, Expert (Fraunhofer ISE, Freiburg)
Ingénieur Docteur HDR (CEA)

Invité
Invité

Référence : TH1032_VAREILLES Victor

L'INSA Lyon a mis en place une procédure de contrôle systématique via un outil de détection de similitudes (logiciel Compilatio). Après le dépôt du manuscrit de thèse, celui-ci est analysé par l'outil. Pour tout taux de similarité supérieur à 10%, le manuscrit est vérifié par l'équipe de FEDORA. Il s'agit notamment d'exclure les auto-citations, à condition qu'elles soient correctement référencées avec citation expresse dans le manuscrit.

Par ce document, il est attesté que ce manuscrit, dans la forme communiquée par la personne doctorante à l'INSA Lyon, satisfait aux exigences de l'Établissement concernant le taux maximal de similitude admissible.

Département FEDORA – INSA Lyon - Ecoles Doctorales

SIGLE	ECOLE DOCTORALE	NOM ET COORDONNEES DU RESPONSABLE
CHIMIE	CHIMIE DE LYON https://www.edchimie-lyon.fr Sec. : Renée EL MELHEM Bât. Blaise PASCAL, 3e étage secretariat@edchimie-lyon.fr	M. Stéphane DANIELE C2P2-CPE LYON-UMR 5265 Bâtiment F308, BP 2077 43 Boulevard du 11 novembre 1918 69616 Villeurbanne directeur@edchimie-lyon.fr
E.E.A.	ÉLECTRONIQUE, ÉLECTROTECHNIQUE, AUTOMATIQUE https://edeea.universite-lyon.fr Sec. : Stéphanie CAUVIN Bâtiment Direction INSA Lyon Tél : 04.72.43.71.70 secretariat.edeea@insa-lyon.fr	M. Philippe DELACHARTRE INSA LYON Laboratoire CREATIS Bâtiment Blaise Pascal, 7 avenue Jean Capelle 69621 Villeurbanne CEDEX Tél : 04.72.43.88.63 philippe.delachartre@insa-lyon.fr
E2M2	ÉVOLUTION, ÉCOSYSTÈME, MICROBIOLOGIE, MODÉLISATION http://e2m2.universite-lyon.fr Sec. : Bénédicte LANZA Bât. Atrium, UCB Lyon 1 Tél : 04.72.44.83.62 secretariat.e2m2@univ-lyon1.fr	Mme Sandrine CHARLES Université Claude Bernard Lyon 1 UFR Biosciences Bâtiment Mendel 43, boulevard du 11 Novembre 1918 69622 Villeurbanne CEDEX sandrine.charles@univ-lyon1.fr
EDISS	INTERDISCIPLINAIRE SCIENCES-SANTÉ http://ediss.universite-lyon.fr Sec. : Bénédicte LANZA Bât. Atrium, UCB Lyon 1 Tél : 04.72.44.83.62 secretariat.ediss@univ-lyon1.fr	Mme Sylvie RICARD-BLUM Institut de Chimie et Biochimie Moléculaires et Supramoléculaires (ICBMS) - UMR 5246 CNRS - Université Lyon 1 Bâtiment Raulin - 2ème étage Nord 43 Boulevard du 11 novembre 1918 69622 Villeurbanne Cedex Tél : +33(0)4 72 44 82 32 sylvie.ricard-blum@univ-lyon1.fr
INFOMATHS	INFORMATIQUE ET MATHÉMATIQUES http://edinfomaths.universite-lyon.fr Sec. : Renée EL MELHEM Bât. Blaise PASCAL, 3e étage Tél : 04.72.43.80.46 infomaths@univ-lyon1.fr	M. Hamamache KHEDDOUCI Université Claude Bernard Lyon 1 Bât. Nautibus 43, Boulevard du 11 novembre 1918 69 622 Villeurbanne Cedex France Tél : 04.72.44.83.69 hamamache.kheddouci@univ-lyon1.fr
Matériaux	MATÉRIAUX DE LYON http://ed34.universite-lyon.fr Sec. : Yann DE ORDENANA Tél : 04.72.18.62.44 yann.de-ordenana@ec-lyon.fr	M. Stéphane BENAYOUN Ecole Centrale de Lyon Laboratoire LTDS 36 avenue Guy de Collongue 69134 Ecully CEDEX Tél : 04.72.18.64.37 stephane.benayoun@ec-lyon.fr
MEGA	MÉCANIQUE, ÉNERGÉTIQUE, GÉNIE CIVIL, ACOUSTIQUE http://edmega.universite-lyon.fr Sec. : Stéphanie CAUVIN Tél : 04.72.43.71.70 Bâtiment Direction INSA Lyon mega@insa-lyon.fr	M. Jocelyn BONJOUR INSA Lyon Laboratoire CETHIL Bâtiment Sadi-Carnot 9, rue de la Physique 69621 Villeurbanne CEDEX jocelyn.bonjour@insa-lyon.fr
ScSo	ScSo* https://edsciencessociales.universite-lyon.fr Sec. : Mélina FAVETON INSA : J.Y. TOUSSAINT Tél : 04.78.69.77.79 melina.faveton@univ-lyon2.fr	M. Bruno MILLY Université Lumière Lyon 2 86 Rue Pasteur 69365 Lyon CEDEX 07 bruno.milly@univ-lyon2.fr

*ScSo : Histoire, Géographie, Aménagement, Urbanisme, Archéologie, Science politique, Sociologie, Anthropologie

Contents

Remerciements/Acknowledgements	iv
Abstract	v
Résumé	vi
Glossary	vii
1 Introduction	1
1.1 Space photovoltaic power generation.....	1
1.2 Space environment and constraints	1
1.3 Standard space rigid photovoltaic array	2
1.4 Space micro-concentration	5
1.4.1 Micro-concentrator module description.....	5
1.4.2 Micro-concentration figures of merit	6
1.4.3 Pros and cons.....	7
1.5 Space concentration state of the art	8
1.6 Highly integrated micro-concentrator design	12
1.7 Design problematic	13
2 Micro-solar cells capillary self-alignment	15
2.1 Introduction.....	15
2.2 Requirements for micro-solar cells alignment and assembly	15
2.3 State of the art of self-alignment processes	16
2.3.1 Micro-springs	16
2.3.2 Shape recognition	16
2.3.3 Magnetic force.....	17
2.3.4 Surface tension-driven self-alignment	17
2.4 State of the art of surface tension-driven self-alignment processes.....	18
2.4.1 Droplet	18
2.4.1.1 Basic wetting theory.....	18
2.4.1.2 Droplet nature	18
2.4.1.3 Droplet confinement	19
2.4.1.4 Droplet deposition	20
2.4.2 Receiving pad.....	21
2.4.3 Component and component feeding.....	22
2.4.4 Conclusion of the state of the art	23
2.5 Experimental process.....	24
2.5.1 Receiving pads.....	25

2.5.2	Solder stencil-printing.....	26
2.5.3	Solar cells initial placement.....	27
2.5.4	Means of characterisation.....	27
2.6	Simulation models.....	28
2.6.1	Analytical model.....	28
2.6.2	Numerical model.....	30
2.7	Results.....	31
2.7.1	Solder volume influence.....	31
2.7.2	Initial displacement influence.....	33
2.7.3	Solder paste influence.....	36
2.7.4	Poor substrate wettability influence.....	37
2.7.5	Pad size and initial displacement combined influence.....	38
2.8	Conclusion.....	40
3	Structural deflection and its impact on optical performances	43
3.1	Introduction.....	43
3.2	Determination of the bending stiffness of the concentrator.....	43
3.2.1	Introduction.....	43
3.2.2	Method.....	45
3.2.2.1	Sandwich theory.....	45
3.2.2.2	Determination of the stiffness of a stabilised aluminium honeycomb with finite element method.....	46
3.2.2.3	Simulation of 4-point bending tests.....	47
3.2.3	Experiments.....	51
3.2.3.1	Samples preparation.....	51
3.2.3.2	Set-up and test procedure.....	53
3.2.4	Results and discussion.....	54
3.2.4.1	Comparison of the experiments and models.....	54
3.2.4.2	Choice of the most interesting configurations.....	56
3.3	Thermally induced deflection of the micro-concentrator array.....	56
3.3.1	Determination of the acceptance angle of the concentrator.....	57
3.3.2	Design of experiments.....	57
3.3.3	Experimental curvature measurements.....	58
3.3.4	Finite element model building.....	59
3.3.4.1	Overview of the FEM model.....	59
3.3.4.2	Materials properties.....	61
3.3.5	Comparison between the experimental deflection and the simulations..	65
3.3.6	Updated model for space materials and environment.....	69
3.4	In-flight bending influence on the optical performances.....	70
3.5	Conclusion.....	72
4	Prototype manufacturing and characterisation	73
4.1	Introduction.....	73
4.2	Optics manufacturing.....	73
4.2.1	Structure lamination.....	73
4.2.2	Silicone moulding.....	73
4.2.3	Silver deposition.....	74
4.3	Front glass manufacturing.....	75
4.3.1	Screen printed tracks.....	75

4.3.2	Soldering with self-alignment	78
4.3.3	Wire-bonding	79
4.3.4	Assembly	79
4.3.5	Manufacturing summary	80
4.4	Electro-optical characterisations.....	81
4.4.1	Current-tension measurements	81
4.4.2	Optical losses analysis	87
4.5	Conclusion	90
5	Conclusion & outlook	91
	References	97
	Appendices	105
A	In-plane capillary forces analytical model	105
B	Micro-solar cells reflow processes	107
C	Comparison between the two screens used to manufacture the prototypes front glasses	107
D	Prototype micro-solar cells placement accuracy	108
E	List of scientific contributions	109
	Résumé détaillé	111
	Introduction.....	111
	Auto-alignement de micro-cellules solaires.....	112
	Influence de la déflexion structurelle sur les performances optiques du concentrateur	115
	Fabrication et caractérisation opto-électrique de prototypes	119
	Conclusion et perspectives	123

Remerciements/Acknowledgements

Je voudrais tout d'abord remercier tous ceux qui m'ont aidé de près ou de loin au CEA pendant ces 3 ans. La liste est longue, dans le désordre et probablement incomplète mais la voici : Julien, Jérôme, Fabien, Nicolas, Rémi, Daniel, Baptiste, Marion, Clément, Carine, Mathieu, Romain, Romain, Romain...

Mention spéciale à mes chers collègues doctorants de l'incontestable meilleur bureau du bâtiment. Merci Karim, Tatiana, Ichrak, Baptiste, Nicolas, Mathieu, Julie, Benjamin, Carla, Antoine, Lucie, Dylan, Vincent, Océane, Nathalie, Julien, Félicia et Shyrnah. A ceux qui sont déjà partis je souhaite une excellente continuation et de nouvelles aventures, à ceux qui sont encore là de profiter de ces trois ans. A tous je souhaite de retrouver ou de conserver l'ambiance formidable de ce bureau, dans lequel j'ai passé de très bons moments. En particulier merci Anderson pour ton accueil et ton accompagnement dans mes débuts pour un début de thèse en douceur.

Toujours dans ce bureau je n'oublie évidemment pas Jean-Baptiste. Merci pour ta pédagogie et ton expertise qui m'ont énormément aidé. Merci aussi pour tes gâteaux que j'ai plus ou moins mérité.

Pour finir je tiens à remercier l'ensemble de mes encadrants qui ont su me faire confiance et me donner beaucoup d'autonomie. Mohamed et Yannick, vos conseils et avis ont toujours été précieux et m'ont permis d'avancer. Philippe, merci beaucoup pour tout le temps et l'énergie que tu as consacré à m'accompagner pendant cette thèse et pour avoir toujours été là en cas de problème. J'espère avoir l'occasion de retravailler avec vous trois.

I had the great opportunity to work with people from ISE in Freiburg, especially with the self-alignment collab people. Big thanks to Henning, Maike and Frank, it was a pleasure working with you all. Very special thanks to Elisa, I enjoyed us working together and I hope we get to pick hundreds of micro-cells again.

I would also like to thank everyone who helped me or just gave me a warm welcome: Gerald, Alex, Juan, Maryam, Armin, Aris, Oli, Tobias and anyone whom I might have forgotten. I had a great time at ISE, I look forward to going back.

Abstract

Space power generation is currently booming with the recent projects of satellites constellations and the diversification of space applications. This trend is driven by a demand for low-cost power. Micro-concentrator photovoltaics (micro-CPV) proposes to focus the light on small solar cells with a cheap optical system, reducing the cell cost of a solar array. However, this technology faces the challenges of mass and volume limitations in space. This thesis work revolves around an innovative micro-concentrator design patented in 2020. This design uses an array of hexagonal mirrors embedded into an aluminium honeycomb. The micro-solar cells are bonded on a glass substrate, in turn placed atop the mirror network. This forms a monolithic, compact, rigid and lightweight structure that can exceed 100 W.m^{-2} , with a geometric concentration of 26X.

First of all, because of the down-scaling of the solar cells (less than 1 mm^2), thousands of small components must be precisely placed on the glass substrate. To reach a high throughput and a placement accuracy of about $30 \text{ }\mu\text{m}$, capillary self-alignment is a promising technique. It is based on the capillary forces of a liquid pulling the cell onto a receiving pad. Experiments and simulations were performed to understand the influence of the liquid volume, the pad size and the initial placement of the cell, allowing to reach an accuracy of $\pm 30 \text{ }\mu\text{m}$ for 140 cells.

Second of all, the concentrator structure will be submitted to high thermomechanical constraints during the spacecraft take-off, solar array deployment and operation. In particular, due to the asymmetric nature of the concentrator and the temperature variation, the structure is expected to bend, modifying the angle of incidence of the sunlight and inducing mechanical stress. This will lead to a decrease of the electrical performances and to system failure at worst. Experiments and simulations were performed to conduct a parametric study of the thermomechanical behaviour as a function of its geometry. This lead to design guidelines, allowing to minimise the stress and the curvature of the concentrator, while keeping the mass constraints in mind.

Finally, the first prototypes of the design were fabricated. Several interconnection designs were tested both indoors and outdoors. First outdoor measurements yielded a power conversion efficiency of 21%. The alignment tolerance between the cell and the mirror was also studied, revealing a tolerance of $50 \text{ }\mu\text{m}$ in the substrate plane to avoid optical losses exceeding 5% of the maximum power output.

Résumé

La demande de production d'électricité dans l'espace connaît actuellement une forte augmentation avec les projets récents de constellations de satellites ainsi que la diversification des applications spatiales. Cette tendance est fortement marquée par des problématiques de faibles coûts. La micro-concentration photovoltaïque propose de diminuer le prix des cellules solaires en concentrant la lumière sur des cellules de taille inférieure au millimètre à l'aide d'un système optique peu coûteux. Cependant, cette technologie doit relever les défis posés par les contraintes de masse et de volume dans l'espace. Cette thèse s'articule autour d'un design de micro-concentrateur innovant, breveté en 2020. Ce concept est basé sur un réseau de miroirs hexagonaux intégrés dans un nid d'abeille en aluminium. Les cellules solaires sont fixées sur un substrat en verre, lui-même placé sur le réseau optique. L'ensemble ainsi constitué est monolithique, compact, léger et rigide. Avec une concentration géométrique de $26\times$, le système peut atteindre $100\text{ W}\cdot\text{m}^{-2}$. Dans un premier temps, en raison de la miniaturisation des cellules solaires, des milliers de petits composants doivent être positionnés avec une précision de quelques dizaines de microns pour former 1 m^2 de module. Pour atteindre une haute cadence d'assemblage et la précision requise, l'auto-alignement capillaire est une solution prometteuse. Cette technique est basée sur l'utilisation des forces capillaires d'un liquide afin de ramener un composant au centre d'un récepteur. Une campagne expérimentale ainsi que des simulations ont été effectuées afin de déterminer l'influence du volume de liquide, de la taille des récepteurs et du positionnement initial des cellules, permettant d'atteindre une précision de $\pm 30\text{ }\mu\text{m}$ sur 140 cellules positionnées. D'autre part, au cours du décollage de l'engin spatial, du déploiement des panneaux et de leur fonctionnement, le concentrateur va être soumis à d'importantes contraintes thermomécaniques. En particulier, en raison de l'asymétrie de la structure et des variations de température, la structure va se courber, modifiant l'angle d'incidence des rayons du soleil et générant des contraintes mécaniques. Ceci aura pour effet de diminuer les performances électriques du système, voire de provoquer la rupture de certains éléments. Des expériences et des simulations ont été menées afin d'effectuer une étude paramétrique du comportement thermomécanique de la structure en fonction de sa géométrie. Grâce à cette étude, des directives de design ont été définies afin de limiter la courbure du concentrateur et les contraintes mécaniques tout en minimisant sa masse. Enfin, les premiers prototypes de ce design ont été fabriqués. Différents designs d'interconnexions des cellules ont été testés et les performances électriques des prototypes mesurées à l'intérieur et à l'extérieur. Un premier rendement module de 21% a été obtenu en extérieur. Une étude de la puissance délivrée en fonction du désalignement d'une cellule avec le miroir a été menée, indiquant une tolérance de $50\text{ }\mu\text{m}$ de déplacement dans le plan du substrat afin que les pertes optiques n'excèdent pas 5% de la puissance maximale obtenue.

Glossary

Photovoltaics & Space

AA	Acceptance Angle
ARC	Anti-Reflective Coating
AM0	Air Mass 0
CPV	Concentrator PhotoVoltaics
AM1.5D	Air Mass 1.5 Direct
AM1.5G	Air Mass 1.5 Global
CTM	Cell-to-module ratio
DNI	Direct Normal Irradiance
FF	Fill Factor
GEO	GEostationnary Orbit
I_{sc}	Short-circuit current
IV	Current-tension
LEO	Low earth Orbit
MEO	Medium Earth Orbit
micro-CPV	Micro-concentrator Photovoltaics
MJSC	Multi Junction Solar Cell
PCE	Power Conversion Efficiency
POE	Primary Optical Element
PV	PhotoVoltaics
PVA	PhotoVoltaic Array
SOE	Secondary Optical Element
STCs	Standard Testing Conditions
UV	Ultra-violet
BOL	Beginning Of Life
EOL	End Of Life
V_{oc}	Open-circuit voltage
1J	Single-junction solar cell
3J	Triple-junction solar cell

Self-alignment

CPH	Components Per Hour
P&P	Pick and Place
PVD	Physical Vapour Deposition

Mechanics

3D	Three-Dimensional
CTE	Coefficient of Thermal Expansion
CFRP	Carbon Fibres Reinforced Polymer
<i>D</i>	Bending stiffness
DMA	Dynamic Mechanical Analysis
DOE	Design of Experiments
DSC	Differential Scanning Calorimetry
<i>E</i>	Young's modulus
FEM	Finite Element Method
<i>G</i>	Shear modulus
<i>I</i>	Second moment of inertia
T_g	Glass transition temperature

1 Introduction

1.1 Space photovoltaic power generation

Since the early day of space exploration, the applications of spacecrafts have become more diverse and mainly include telecommunications, monitoring and defence [1]. The number of spacecrafts has boomed in the last years and is expected to keep increasing with the recent projects of satellites constellations. Regardless of its application or size, a spacecraft requires power to operate. PhotoVoltaic (PV) power generation is the historical choice and was initially developed to power space exploration missions. In 1954, *Bell Laboratory* announces the invention of the first practical silicon solar cell, more than a century after the discovery of the photovoltaic effect by Edmond Becquerel. Only four years later in 1958, the first solar powered satellite *Vanguard I* is launched. At the time, those silicon cells adapted for space have an efficiency of about 8-10% [2]. Nowadays, other technologies like batteries or Radioisotope Thermoelectric Generator (RTG) are also used. RTGs produce electricity by converting the heat generated by radioactive materials decay [3]. Depending of the mission of the spacecraft, one technology or the other may be more or less suitable. For missions not further away from the sun than Mars, photovoltaic solution is the preferred choice [4]. Sunlight is steadily and widely available and is not subject to seasonal variations like on Earth. A mission powered by PhotoVoltaic Arrays (PVAs) can then be autonomous energy-wise for a large time span of about 30 years. However, as the spacecrafts gets further away from the sun, the incoming solar irradiance decreases, from 1367 W.m^{-2} around the Earth to only 50 W.m^{-2} around Jupiter [4]. Not only is the solar irradiance and thus the available power much lower, the solar cells also are less efficient under such conditions. For short time missions with a low irradiance, batteries can be enough. For longer duration, the power density becomes too low and relying solely on batteries would make the spacecraft too heavy and thus costly. RTGs can then be used as a complement.

Nevertheless, most missions stay close to the Earth and use solar power. The International Space Station, launched in 1998 is still powered by solar panels to this day, even if some were replaced with more recent technologies. Very recently, the James Webb telescope launched in 2021 is powered by solar energy. Its expected life is around 20 years. Its solar panels power the various cameras and telecommunication system on board.

1.2 Space environment and constraints

Compared to terrestrial devices, spacecrafts are subjected to extremely harsh conditions that vary a lot depending on the mission. In particular, PVAs are directly exposed to the

environmental conditions. Their design must take them into account to define a viable device.

In the absence of atmosphere, spacecrafts only rely on thermal radiation for thermal management. PVAs can be submitted to high (150°C) or low (-180°C) temperature depending on the received irradiance. In both cases, all the components of the PVAs must withstand and operate under such conditions. Moreover, the temperature can quickly vary over a large amplitude. As an example, in Low Earth Orbit (LEO), the temperature goes from -120°C to +120°C in 90 min [5]. LEO is an orbit between 200 and 2,000 km. This high amplitude thermal cycling can have a dreadful impact on the PVAs in the long run. The repeated stress caused by the expansion and contraction of different materials can lead to failure of electrical connections or interfaces degradation [6]. Overall, thermal cycling and extreme temperatures put a lot of constraints on the material choices for spacecrafts.

In space, without the protection of strong magnetic field like on Earth, PVAs are exposed to high energy radiations, mainly UV light, electrons and protons. UV tends to degrade the optical properties of polymer encapsulant, decreases the PCE of the array [7]. High energy electrons and protons cause ionisation and displacement of atoms in the solar cells materials lattices [8]. These radiations slowly decrease the performances of solar cells and are still studied extensively [9]. Thus, the performances of PVAs are often compared at Beginning Of Life (BOL), prior to flight and End Of Life (EOL), after operation. Depending on the mission length and location, the expected radiation dose varies [10] and so does the EOL performances [11]. This must be kept in mind when designing PVAs, since it will need to power the spacecraft even at EOL with degraded performances.

For space applications, mass and volume are highly limited resources, hence the achievement of a high power output with a light and small system is critical. As a matter of fact, launching 1 kg into space can cost several thousand euros depending on the mission [12]. Therefore, reducing the cost of a space solar array can be meaningless if it implies a mass or volume increase.

There are other environmental constraints that will not be discussed further as they are not relevant to the topics studied in this thesis. For information purposes, such constraints include vacuum, plasmas, micrometeoroids and debris impacts.

1.3 Standard space rigid photovoltaic array

All the environmental and costs constraints explained before have led to the development of what is the standard space PVA today. Figure 1.1 shows a scheme of such a structure. To increase the PCE and thus reduce the PVA mass and volume needed, triple-junction (3J) solar cells are typically used instead of silicon ones, by far the most common on Earth. Most of the time, the cells are protected from the radiations by an individual thin cover glass. The glass is about 100 μm thick and is cerium doped to provide radiation hardness [13]. They are glued to

the cell using silicone. The cell/glass structure is known as Cover glass Interconnected Cells (CIC) and is shown in Fig. 1.1.

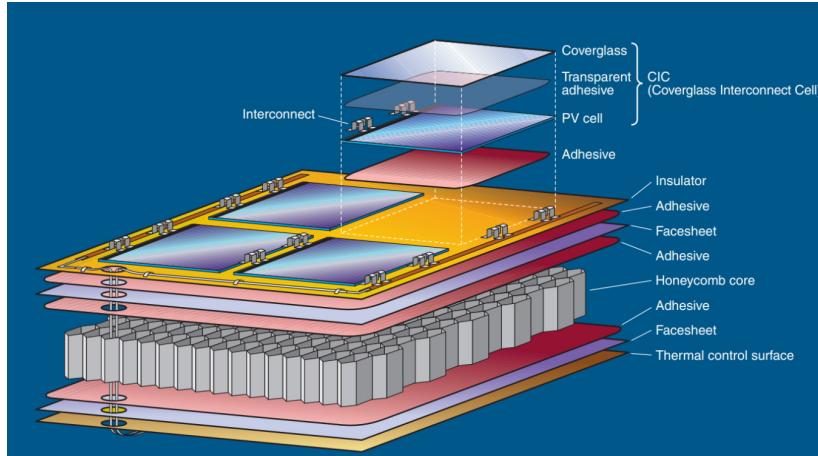


Figure 1.1: Scheme of the standard flat rigid space photovoltaic panel. From [14].

The cells themselves are placed on a composite sandwich structure. The sandwich is composed of an aluminium honeycomb core in the middle and two carbon fibres composites sheets on its top and bottom. The core provides high shear and compressive stiffness and strength. The sheets provides bending stiffness and strength. The aluminium honeycomb and carbon fibres composites are both chosen for their high mechanical properties and low mass. Because carbon fibres are a poor electrical insulator, polyimide sheets are added on the carbon fibres.

To produce 3J cells, III-V materials are grown on Ge substrates. Such commercial cells achieve a high PCE of about 29% at BOL [15] and have a high radiation hardness compared to silicon cells. However, 3J III-V cells are much more expensive than silicon cells because of the rare materials cost and their complex manufacturing process [16].

In the end, they represent a large part of the overall cost of the PVA [17]. Typical 3J space solar cells are about a few dozens of square centimetres.

A scheme of both a single-junction (1J) silicon and a 3J III-V solar cells are displayed in Fig. 1.2.

A 1J solar cell can only absorb the photons with an energy E_p higher than its band gap E_g . If $E_p < E_g$, the photon passes through the material and is lost. When the photon is absorbed, it creates an electron-hole pair by giving enough energy to an electron to move from the valence band to the conduction band. If $E_p > E_g$, the electron energy will quickly decrease to reach the edge of the band gap with an energy E_g . In practice, this means that the energy $E_p - E_g$ is lost.

Also, the voltage delivered by the solar cell does not exceed its band gap. To sum up, the 1J cell efficiency is limited because it can only absorb a part of the solar spectrum and the electron excited by the photon can only be collected with an energy smaller than the band gap. In the case of a 3J cell, each junction absorbs a specific part of the solar spectrum. More photons are absorbed and the voltage delivered is equal to the sum of the voltage delivered

by each sub cell. The efficiency of the solar cell can be much higher. As an example, the theoretical efficiency limit of solar cells is about 33% for 1J [18] and 60% for multi-junction solar cells [19].

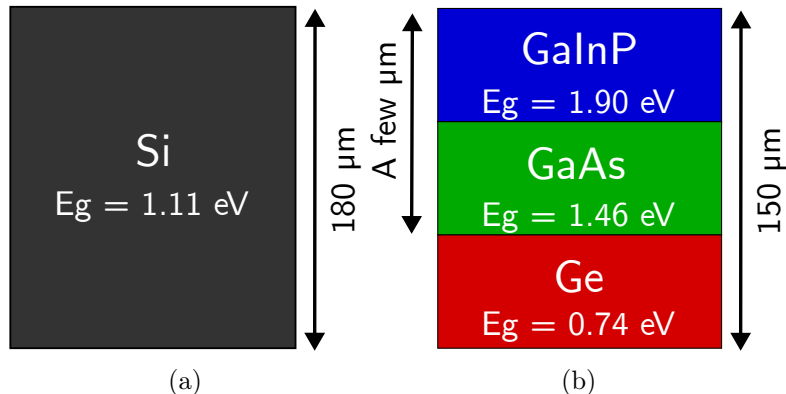


Figure 1.2: Scheme of the architecture of a single-junction (a) and a triple-junction (b) solar cell. The band gap energies and the thicknesses are given for guidance only.

Figure 1.3 shows the equivalent electrical scheme for a 1J and a 3J solar cell. A 1J cell can be modelled as a diode with a series (R_s) and a parallel or shunt (R_{sh}) resistor. The current I as a function of the voltage V and the temperature T is written as in Eq. (1.1), considering that $\exp(qV/nkt)$ is much greater than 1. I_0 is the dark saturation current, I_L is the photo-generated current, q the elementary charge, n the ideality factor and k the Boltzmann constant.

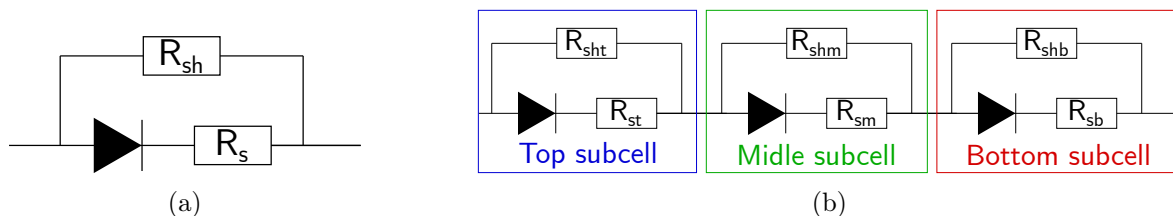


Figure 1.3: Electrical scheme of a single-junction (a) and a triple-junction solar cell (b).

It is important to remark that the irradiance conditions can strongly influence the cell operation. At low irradiance, the parasitic shunt current becomes significant compared to the collected current, resulting in high performance drops. On top of that, edge recombination on the cell edges become significant as well, decreasing the V_{oc} of the cell.

$$I = I_L - I_0 \exp \left[\frac{q(V + IR_s)}{nkT} \right] - \frac{V + IR_s}{R_{sh}} \quad (1.1)$$

A 3J can be modelled as three 1J cells in series. As a consequence, the current delivered by the three subcells is identical and the current delivered by the whole cell is limited by the subcell with the lowest current. Additionally, the voltage delivered by the whole cell is about equal to the sum of the band gap of each subcell. Compared to a 1J solar cell, 3J cells deliver

a lower current and a higher voltage. To avoid power losses, each subcell must be precisely balanced so that they all deliver the same current.

Figure 1.4 shows a scheme of a typical current-voltage (IV) curve of a module. The open circuit voltage (V_{oc}) is the voltage at which the current is nil. The short circuit current (I_{sc}) is the current at a nil voltage. From the IV curve, the power-voltage curve can be deduced, also displayed in Fig. 1.4. The power reaches a maximum for a voltage V_{mp} and a current I_{mp} . This point is called P_{mpp} . The fill factor (FF) of the module is defined by the ratio of $S_1 = V_{mp} \times I_{mp}$ and $S_2 = V_{oc} \times I_{sc}$ presented on the graph. It is calculated thanks to Eq. (1.2).

$$FF = \frac{V_{mp} \times I_{mp}}{V_{oc} \times I_{sc}} \quad (1.2)$$

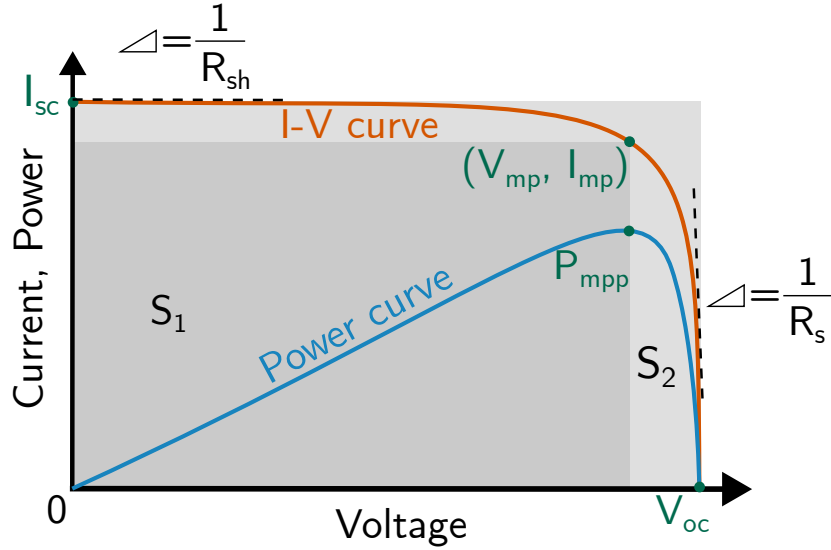


Figure 1.4: Scheme of an IV curve and associated figures of merit.

1.4 Space micro-concentration

1.4.1 Micro-concentrator module description

A micro-concentrator has a slightly more complex architecture than flat panels. According to the IEC norm [20], it is made of interconnected cells and an optical system. As its name suggests, micro-CPV uses sub-millimetre solar cells. The cells interconnections are derived from micro-electronics technologies and include soldering, welding and wire-bonding. The optics rely on a Primary Optic Element (POE) to focus the incoming light. The POE can be either refractive (*e.g.* Fresnel lenses) or reflective (*e.g.* parabolic mirrors). A smaller Secondary Optic Element (SOE) can be added to increase the concentration ratio or to improve the acceptance angle of the concentrator module. A few examples of concentrator designs are presented in Fig. 1.5, including two refractive (Fig. 1.5(a) and Fig. 1.5(b)) and two reflective (Fig. 1.5(c) and Fig. 1.5(d)) designs.

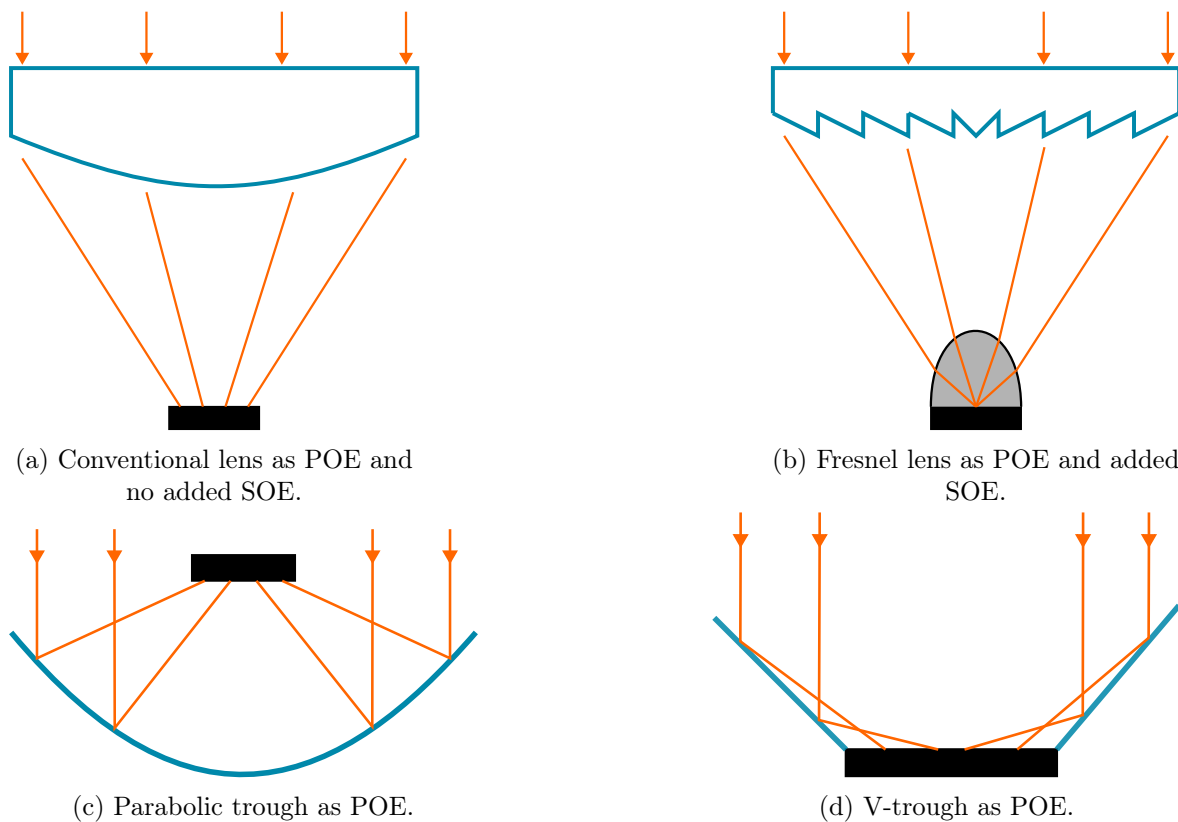


Figure 1.5: Examples of refractive (a, b) and reflective (c, d) concentrator designs.

1.4.2 Micro-concentration figures of merit

PV modules electrical and optical characterisation are performed at controlled temperature and irradiance. The Standard Testing Conditions (STCs) correspond to a temperature of 25°C and a standard irradiance that depends on the application. Terrestrial applications use the AM1.5 spectrum ($1000 \text{ W}\cdot\text{m}^{-2}$)[21], space applications use the AM0 spectrum ($1367 \text{ W}\cdot\text{m}^{-2}$)[22]. Unless specified otherwise, all the figures of merit presented further in this section are defined under STCs.

The Power Conversion Efficiency (PCE), sometimes noted η of a PV module describes the part of the power input that is effectively converted to electricity. It is defined as the ratio of the electrical power output and the total received power.

The cell-to-module ratio (CTM) is the ratio of the PCE of the concentrator module and the PCE of the cell. It can be used to assess how well the full concentrator module is designed and build, without taking the influence of the PCE of the cell itself into account.

Concentrator modules are also characterised and defined by specific figures of merit. In the following, we will consider a single micro-solar cell and the corresponding optical unit used to collect the light and focus it onto the micro-solar cell. The geometric concentration is defined as the ratio of the light receiver (solar cell) area over the light collecting area (optical

unit). It does not take into account any optical losses and thus does not fully describes the actual irradiance under which the solar cell is placed.

To describe the incident light optical losses, the optical efficiency is used. It is defined as the ratio of the irradiance received by the cell and the irradiance received by the optical unit.

The Acceptance Angle (AA) is defined as the angle of incidence of the light for which the module generates 90% of its maximum power output. Thus, a high AA means that the module is less sensitive to variations of the angle of incidence of the light. As a rule of thumb, a concentrator with a higher concentration rate will have a lower AA. One should bear in mind that trackers usually have an alignment accuracy of about 0.1° .

In space, mass and volume constraints are represented by the mass specific power in $W.kg^{-1}$ and the volume specific power in $W.m^{-3}$. They are defined as the power output of the module divided by its mass, respectively its volume.

1.4.3 Pros and cons

As mentioned earlier, III-V solar cells represent about 50% of the total cost of a space PVA [17]. By reducing the solar cell size for the same light collecting area, micro-concentration concepts represent an interesting way to decrease the cell cost as less III-V materials are needed.

Besides, not only did micro-concentration proved viable in space, but is also demonstrated higher radiation resistance compared to standard flat panels [23, 24]. Thus, the EOL efficiency of a space micro-concentrator can be expected to be higher than for a flat array. A smaller PVA can then be used, reducing the overall costs.

Another positive effect of concentration is the increase of the voltage of the device, hence an efficiency increase. The open-circuit voltage V_{oc} scales with the logarithm of the concentration ratio X (see Eq. (1.3)), so the efficiency increase becomes significant with high concentration, provided that there is no degradation of the fill factor, for example because of increased resistive losses. The short circuit current density J_{sc} is proportional to the irradiance and can then be defined by Eq. (1.4).

$$V_{oc}(X) = V_{oc}(1 \text{ sun}) + \frac{nkT}{q} \ln(X) \quad (1.3)$$

$$J_{sc}(X) = J_{sc}(1 \text{ sun}) \times X \quad (1.4)$$

An often-mentioned drawback of PV concentration is the difficult thermal management. The higher incoming irradiance results in a higher cell and module temperature that sometimes requires a passive or active cooling system. This is incompatible with space applications since the cooling system increases the mass and volume of the module. Either way, convection cooling cannot be used in space. Even so, a higher operating temperature decreases the voltage output. Micro-concentration significantly improves the thermal dissipation of the module and

decreases its operating temperature compared to larger scale concentrators [25, 26]. Coupled with a low to moderate concentration and an appropriate design, micro-scaling can remove the need for added thermal dissipation [27].

As previously described, the CTM represents the complete chain losses of a concentrator. Ritou *et al* [28] demonstrated that the down scaling of concentrators reduces the losses, improving the PCE.

Notwithstanding, one cannot stress the pros of micro-CPV without also presenting its flaws. Adding an optical system results in a mass and volume increase, even if micro-concentration limits it compared to standard concentration.

Moreover, compared to flat PVA, many small components must be precisely put together to form the final concentrator. For low concentration, the amount of component is higher than for high concentration, but the manufacturing tolerances are also higher. Nevertheless, this added complexity can increase the manufacturing cost.

Lastly, micro-CPV relies on direct normal irradiance. This makes CPV difficult to use in environment with dust (*e.g.* the surface of the Moon or Mars) or clouds (*e.g.* Venus atmosphere). Besides, micro-CPV tends to have a higher cell operating temperature than flat PVAs. It becomes a problem for missions with high irradiance, closer to the sun. Bermudez *et al* studied the viability of CPV in space. The technology was deemed viable for 18 missions out of 33 considered [29].

1.5 Space concentration state of the art

CPV is a flight-tested technology that has proven his reliability in harsh space conditions. The first flight experiments featuring concentrators was the Photovoltaic Array Space Power Diagnostics Plus (PASP+) mission in 1994 [23]. Various PV technologies were tested, included two concentrator design, one with mini-dome lenses (see Table 1.1) and the other one with Cassegrainian mirrors. The mini-dome were coated to shield the cells form UV and atomic oxygen. It operated at a concentration of 100X [30]. During its 373 days mission, the spacecraft was put in an environment with a high electron radiation dose. After a year, the CPV module presented the smallest performances degradation of the tested arrays, with a power decrease of 7% [24]. Later on, a Fresnel lenses CPV was manufactured to be cheaper than the mini-dome lenses [23].

The first spacecraft primarily powered by concentration was the AstroEdgeTM, launched in 1998. It featured a reflective design with a low concentration of 1.5X. Large reflectors were put on the side of a flat rigid solar array. However, deployment failure occurred and the goals of the mission could not be met. It is important to note that this failure was not due to the concentrator system but to the payload [31]. A picture of one its concentrator design is displayed in Table 1.1.

Deep Space 1 was launched in 1998. Its instruments and ion-propulsion were powered

during 38 months [32], proving the reliability of CPV in deep space environment. The CPV modules, called SCARLET, used linear Fresnel lenses, focusing the sunlight on $10 \times 40 \text{ mm}^2$ solar cells. The system operated at a geometric concentration ratio of 7.14X. A picture of the array can be found in Table 1.1. This low concentration coupled with the linear geometry of the design provided a high acceptance angle. Only 5% power losses were measured over 1° rotation in the direction parallel to the cells and 3° rotation in the transverse direction [32]. To reduce the stowed volume of the array, an in-flight deployment step was necessary [33]. After this successful mission, the SCARLET design was modified to provide an even lower stowed volume. In the Stretched Lens Array (SLA) concentrator, foldable silicone lenses are used so that the array is flat before deployment [34]. The cells were placed on a metal substrate, sturdier than glass and useful for heat dissipation. The SLA was flight-tested in 2011 on the TacSat-4 mission [35]. A high radiation hardness was demonstrated thanks to its high radiation-shielding thickness [36]. However, some silicone lenses experienced damage. An improved meshed version of the lenses was developed but has not been tested yet [37]. Nonetheless, the initial design is claimed to have a specific power of 180 W.kg^{-1} , much higher than standard flat PV arrays [38].

In 2002, a new reflective concentrator design was launched in orbit aboard the Galaxy XI satellite. The Hughes 702 design was similar to the AstroEdge one, with a concentration ratio of 1.7X [39]. A view of the satellite with its PVAs is shown in Table 1.1. The CPV array experienced quick performances degradation due to contamination of the reflectors. Nowadays, the contamination is attributed to outgassing of contaminants due to the high temperature of the array [40]. This design was then slightly modified to reduce the operating temperature of the concentrator from 125 to 75°C . This was achieved in the CellSaver design manufactured by Orbital-ATK [41]. In this version, the thermal load is lightened by increasing the thermal radiation area. The edge reflectors are made of titanium sheets with a silver and dielectric coating, providing a high reflectivity and a radiation hardness. The reflectors can be folded and deploy on their own [42]. The CellSaver design was tested in 2004 for a duration of nine months. Over this duration, the power and temperature of the array was monitored. No sign of early degradation like on the Hughes design was observed [42]. A more recent version of the CellSaver design is visible in Table 1.1.

Overall, few concentrators have been flight-tested between 1994 and 2004, reaching a Technology Readiness Level (TRL) of 9 but remaining limited to experiments or scientific applications. Nonetheless, the reliability of CPV in space was demonstrated and these systems proved especially well-suited to harsh radiations environments. A good potential to reduce the cell cost and improve the efficiency is also to be noted. Relatively low concentration ratios are preferred, not exceeding 10X except for the PASP+ experiments. High optical efficiency were reported, ranging from 85% to 91.5%. However, even if most missions suffered no major issues, concern arose from optics contamination on the Galaxy XI spacecraft. The long term reliability of systems, especially optics, has not been tested in actual space conditions as missions duration did not exceed three years. The cell operating temperatures were also

rather high, decreasing the PCE and accelerating ageing. Furthermore, the added mass of this optics did not allow to top the specific power of standard rigid arrays (80 W.kg^{-1} , [38]) not exceeding 75 W.kg^{-1} for the PASP+. The cell cost reduction was not enough compared to the additional mass and design complexity of concentration to drive more reliability tests and space certification. The concentration approach was somewhat left behind after 2004, unable to compete with the cheaper and safer CIC solution. But, in the recent years, CPV technologies have known a revival thanks to the promises of micro-CPV. Besides, with the dramatic increase of space power generation demand, the current 3J III-V solar cells production is not enough for every space craft to be provided with cells. Moreover, CPV is a promising solution for deep space missions with a very low irradiance. Focusing the light helps getting closer to standard irradiance conditions, avoiding the cell performance drops and degradation described earlier. In this new context, innovative designs are under development with higher levels of integration, increasing the specific power and improving the thermal managements for higher performances and reliability [25].

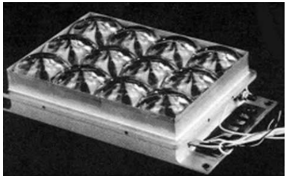
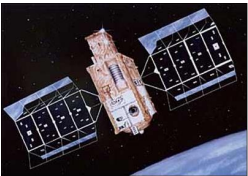
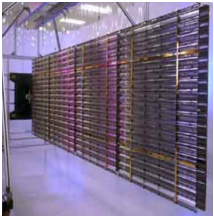

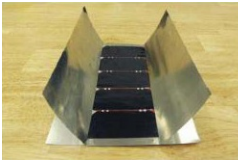
Satellite	APEX	NRO STEX	Deep space 1	Galaxy XI	Cell Saver
Picture					
Year	1994	1998	1998	2000	2004
Concentration	100	1.5	7.5	1.7	2
Specific power (W/kg at BOL)	75	70	48	60	NA
TRL	9	9	9	9	9

Table 1.1: Summary of the main characteristics of flight-tested concentrators.

1.6 Highly integrated micro-concentrator design

Based on the state of the art of space micro-CPV, an innovative design was proposed by A. Bermudez-Garcia, P. Voarino and O. Raccurt and patented in December 2020 [43]. This design is presented in Fig. 1.6.

Design/Institute	Specific power (W/kg)	Concentration	TRL	Year
All flight-tested	<75	1.5-100	9	1994-2004
NRL/Semprius	/	20	5	2016
Pennsylvania University	111	18.4	5	2019
CEA-Liten	100	26	5	2020

Table 1.2: Summary of the main characteristics of flight-tested and latest under development concentrators.

The concentrating optics are a network of quasi-regular hexagonal mirrors embedded into a aluminium honeycomb structure. There is one mirror in each individual honeycomb cell. The micro-solar cells are bonded onto a glass substrate. The substrate itself is placed and bonded atop the honeycomb structure. The honeycomb acts as a lightweight mechanical support for the glass and the optics, fixing the distance between them. The glass protects the cells from radiations with minimum optical losses. In this configuration, the sunlight first passes through the glass, then is reflected by the mirrors and focused on the micro-cells. To ensure the stability and mechanical strength of this structure, it is bonded to a sandwich structure, made of an aluminium honeycomb core glued between two Carbon Fibres Reinforced Polymer (CFRP) layers. The geometric concentration is equal to 26X. The materials of the design are space standards, chosen for their high stiffness and strength to mass ratio.

A reflective system was chosen over a refractive one for the following reasons. First, it is achromatic and reduces spectral matching issues that would decrease the current of the MJSCs [44, 45]. Second, mirrors can have a short focal distance and therefore a high compactness, improving the $W.m^{-3}$ of the concentrator. Third, mirrors are lighter than lenses because they are concave instead of convex, reducing the amount of material and improving the $W.kg^{-1}$ of the structure. Finally, reflective designs have the highest optical efficiency reported (97%).

No SOE is needed and the optical path is short, which helps reducing the optical losses.

The thermal management is not expected to be a problem. The concentration ratio is moderate and the glass substrate acts as a good heat radiator (about 0.9 emissivity).

Since the glass substrate must be relatively thick (a few hundreds of μm) to support the cells and the cells are not facing the sun, a high radiation resistance is expected. This means that for a long mission, the EOL performances will be higher than standard CIC assembly, reducing the quantity of PVAs needed to reach the same power output. Nonetheless, a balance between the improved radiation hardness and added mass due to the cover glass thickness must be found. This structure is monolithic and fully integrated, no other support or alignment step is needed in flight, reducing the failure risks. The upper stage (glass, honeycomb and CFRP)

is very thin, at 3 mm.

Finally, the hexagonal mirrors network fully covers the solar panel, increasing its filling ratio compared to standard CIC assembly. In the end, the specific power of the design could realistically reach 100 W.kg^{-1} . This is higher than flight-tested concentrators and close to more recent designs estimations (see Table 1.2). Most importantly, this design includes mechanical support so no additional mass is expected. Besides, the higher but moderate geometric concentration compared to the Pennsylvania University approach should provide lower cell costs.

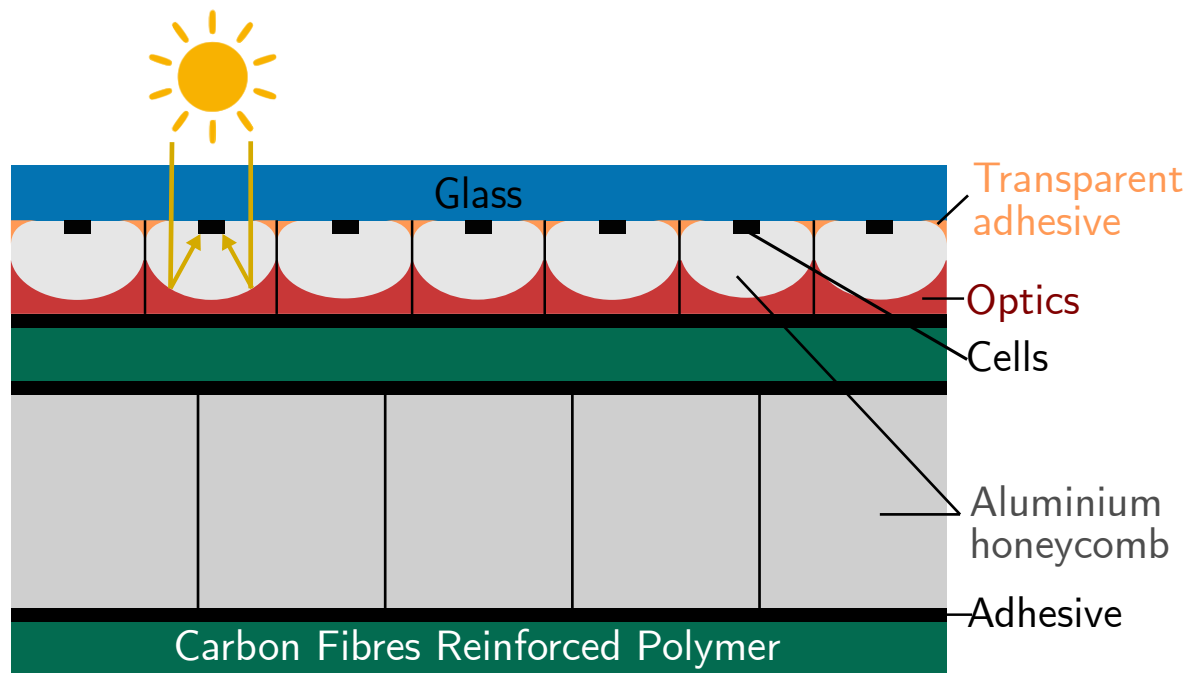


Figure 1.6: Scheme of the concentrator design.

1.7 Design problematic

As mentioned earlier, this design was patented during the course of a previous PhD thesis, in 2020. On top of defining the structure, the optics were designed, a manufacturing process was defined and the resulting optics were characterised. As expected, more aspects of the concentrator still need to be studied.

Indeed, despite its advantages, the design is of course not without flaws. Using micro-solar cells with a low concentrator factor means that a lot of small components must be precisely aligned with the optics, especially since there is no alignment step once the glass substrate is bonded on the honeycomb. With the concentration ratio of 26X and considering 1 mm^2 cells, there are about $50,000 \text{ cells.m}^{-2}$. Those cells should be precisely placed on the glass (a few tens of microns), and the glass precisely placed on the honeycomb. Furthermore, the whole alignment process must be done at a high speed to reduce manufacturing time and costs. Standard assembly techniques from the microelectronics field like pick & place machines struggle to maintain a high throughput and a high accuracy at the same time. An interesting

solution that could combine both is the self-alignment approach, allowing to use the pick & place machines at their maximum speed without sacrificing accuracy or reliability. This would decrease manufacturing time and thus cost, increasing the competitiveness of micro-CPV.

Moreover, the module will have to withstand harsh conditions during the aircraft take-off, the panels deployment and finally when operating. Due to vibrations and large temperature spans, high mechanical stress is expected, particularly in the glass. Besides, the structure will bend when the temperature changes, decreasing its optical performances. The combined effects will induce electrical performances decrease and could even be responsible for system failure. At the same time, the geometry of the concentrator must be carefully tuned to avoid such issues without increasing the mass of the design.

Finally, the concentrator manufacturing itself is a major concern because of its novelty. There is no precedent and a first prototype must be fabricated at this stage of its study.

1. The first and current chapter presented the space environmental constraints, the current standard PVA design, space micro-CPV systems and the innovative micro-concentrator design for space applications that was studied in details during the course of this thesis.
2. The second chapter focuses on the accurate placement of the micro-solar cells on their cover glass using self-alignment. In particular, a state of the art of the current self-alignment technologies is presented. Based on it, a process to be studied was defined. Then, capillary self-alignment experiments are described and the results analysed. Finally, simulations of the process are explained and compared to the experiments.
3. The third chapter deals with the thermomechanical behaviour of the concentrator structure. More precisely, the bending stiffness and the temperature-dependent curvature of the design as a function of the thickness of its layers was studied. Bending tests and curvature measurements were performed experimentally and modelled. Finally, the influence of the in-flight curvature of the structure on its optical performances was estimated.
4. The fourth chapter tackles the manufacturing and electrical characterisations of the first prototypes of the micro-concentrator. First, the different prototype designs and their characteristics are described and explained. Then, the electrical performances of the design was measured by indoor, outdoor and dark current-tension measurements.

2 Micro-solar cells capillary self-alignment

2.1 Introduction

As mentioned earlier, precise assembly and alignment of the micro-solar cells are crucial. Positioning errors of a few dozens of microns are enough to decrease the CPV performance [46]. The assembly speed itself is also a major concern, as a slower process would result in higher fabrication costs which would lead the concept to a lack of economic competitiveness to cheap flat silicon panels. A promising solution, also studied in the micro-electronics field is self-alignment. In this chapter, the state of the art of self-alignment assembly is presented first. In particular, surface tension-driven techniques are put under the spotlight. Second, the best suited technique for micro-solar cells is identified. Third, an experimental campaign on the influence of solder volume and pad size is presented and the results discussed. Finally, the results from capillary forces simulations are displayed and explained.

2.2 Requirements for micro-solar cells alignment and assembly

To some extent, the assembly and alignment of micro-solar cells for concentration is similar to chip assembly in micro-electronics. In both cases, many sub-millimetre scale components must be quickly and precisely positioned on a substrate. In the case of the studied design, the micro-solar cells are $885 \times 685 \times 190 \mu\text{m}$ cuboids. The electrical connections of the cells are on both sides (front and rear). The assembly requirements are the following:

- The translation, out-of-plane rotation and in-plane rotation of the cell will have an impact on its performances and should be controlled precisely [46].
- Further interconnections between the cells cannot be prevented, so non-conductive adhesives cannot be used.
- A strong bond between the cell and the substrate must be made.
- The assembly should withstand the high temperatures encountered in space (about 100°C)
- The process should not degrade the optical performances of the glass

Pick & Place (P&P) seems to be the right option for micro-solar cells assembly. Indeed, it is a standard process for micro-electronics and can reach high precision (up to a few microns) and high throughput (thousands of components per hour). It is already used in CPV manufacturing [47]. However, a trade-off must be made between the placement accuracy and the throughput. To reach a high accuracy, several image recognition steps are necessary: the machine must check how a component is handled and where to place it on the substrate using

cameras. Both those steps slow the process down. It is possible to remove the recognition steps at the cost of placement accuracy. To decrease the manufacturing costs of CPV modules further, this limitation must be broken. As a consequence, a new assembly process with higher accuracy and throughput must be developed. A promising solution is based on self-alignment. As its name suggests, it gathers different processes reaching placement accuracy of up to a micron [48] with a high throughput. It has already proven effective for the manufacturing of micro-concentrators [49, 50].

2.3 State of the art of self-alignment processes

2.3.1 Micro-springs

Micro-springs can be used to bring and maintain a component in front of its receptor [51]. However, it is not suitable for our application as it would require adding non-transparent springs on the glass. Due to vibrations during deployment and take-off of the spacecraft, the cells could also be detached from the substrate, as no strong bond is made.

2.3.2 Shape recognition

Another promising way to self-align components in a massively parallel fashion is to use shape recognition. A scheme of the principle is shown in Fig. 2.1. This technique consists of carving receptors which have the inverse shape of the components into the substrate. The following step is to place the components in the receptors cavities. There are several ways to do so, but the most interesting and parallel one consists of placing the components and the substrates into a fluid medium with agitation. The components are then moving in a random way in the medium, but get trapped in the receptors. The drawbacks are that more components than receptors are needed if one wants to place one atop every receptor. The time needed to reach this state also depends on the numbers of components compared to the number of receptors. Furthermore, cubic components, like solar cells, risk being flipped over. Nevertheless, this is a massively parallel process, theoretically allowing a high throughput with an accuracy depending on the receptors dimensions tolerances. It is worth noting that this technique has been used to make micro-concentrators in the framework of the MOSAIC project with a 400X concentration ratio [52] and another project supported by LG electronics with a concentration ratio of about 5X [53]. It is also currently in use in the micro electronics field [54].

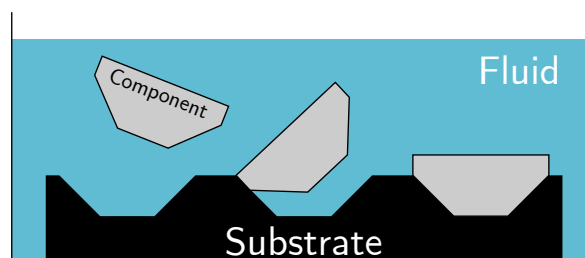


Figure 2.1: Principle of self-alignment based on shape recognition.

2.3.3 Magnetic force

As the name suggests, magnetic self-assembly proposes to use magnetic force to self-align dies on a wafer. The preparation of the substrate itself is quite complex: magnetic pads need to be made on the substrate, using deposition techniques. Adding interconnections on the substrate requires additional steps. The dies themselves need to be prepared in the same way. During the assembly step, the substrate is fixed and the dies are floating above it. Vibrations are added to favour the correct positioning. Thanks to the polarities, the dies are positioned with the right orientation in a parallel process and held by the magnetic forces. This assembly technique was studied in [55]. Due to its complexity, we chose not to study it further, a simpler solution being more desirable. A scheme of this process flow is presented in Fig. 2.2.

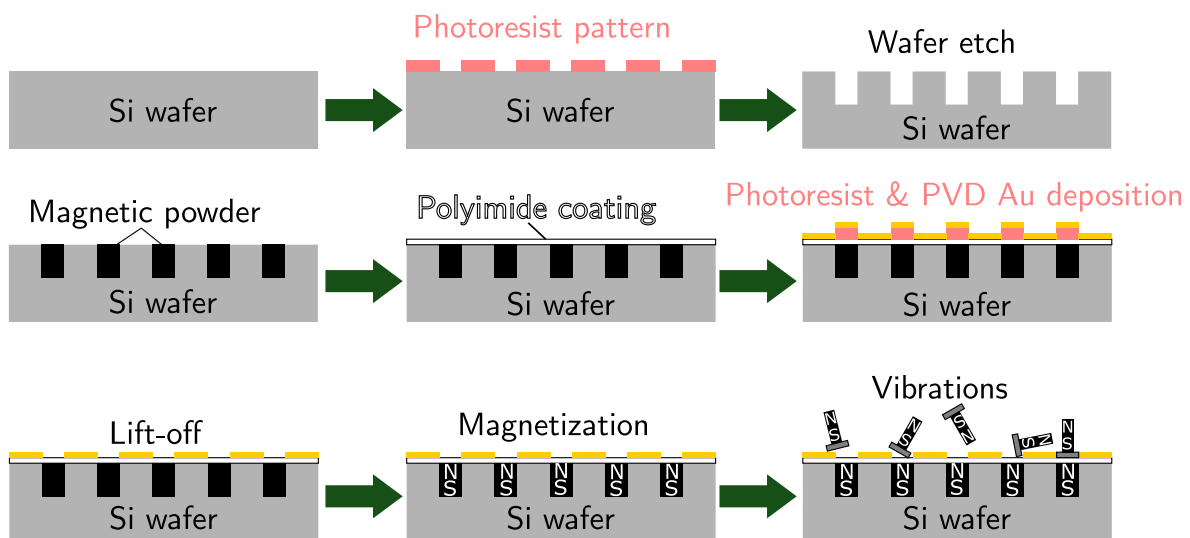


Figure 2.2: Scheme of a self-alignment process based on magnetic forces.

2.3.4 Surface tension-driven self-alignment

At the millimetre scale or below, capillary forces are the dominant ones. Surface tension-driven self-alignment is based on the minimisation of the surface tension of a droplet (see Fig. 2.3). For a droplet confined to a well-defined area, the surface tension reaches a minimum when the droplet is at the centre of the area. If a die is placed on top of the droplet, it is brought to the centre of the area as well.

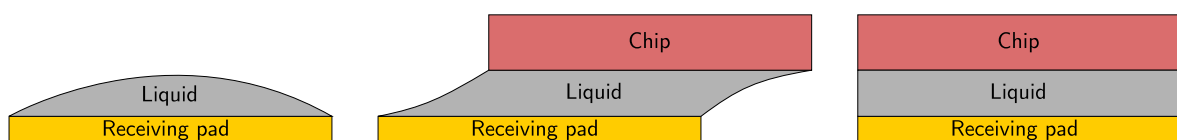


Figure 2.3: Principle of surface tension-driven self-alignment.

The main advantage of this process is that sub-micron precision can be achieved. Additionally, it does not require a precise placement, making it suited for a high throughput and low precision component placement technique. It is also quite flexible: a wide variety of liquids

can be used, different component feeding options are possible as well as droplet deposition techniques and the size of the components can go up to a dozen millimetres. Those different topics will be discussed in the following sections.

2.4 State of the art of surface tension-driven self-alignment processes

Surface tension-driven self-alignment or capillary self-alignment depends on a lot of parameters, namely the liquid, the receiving pad nature and cleaning, the component itself and its feeding. This section presents the influence of those parameters and the limitations of such a process.

2.4.1 Droplet

2.4.1.1 Basic wetting theory

The wetting of a liquid on a surface, *i.e.* how well the droplet spreads on it, is characterised by the contact angle (see Fig. 2.4). A high wetting angle corresponds to a poor wettability, a low angle to a good one. The contact angle θ is defined by the Young-Dupré equation:

$$\cos \theta = \frac{\gamma_{SG} - \gamma_{SL}}{\gamma_{LG}} \quad (2.1)$$

Where γ_{SV} , γ_{SL} and γ_{LV} are the surface energy of the solid/gas, solid/liquid, liquid/gas interfaces.

From this equation, it appears that for the same liquid/gas interface, the wetting is good if the solid/liquid interface has a low energy. In practice, a liquid with a low surface tension like silicone oils tends to have a good wetting on most surfaces. On the other hand, for higher surface tension liquids, the solid should have a similar surface tension and polarity as the liquid. As an example, water is polar and has a high surface tension compared to most organic liquids. Its wettability is good on polar surfaces like glass but poor on non-polar surfaces like metals.

However, the Young-Dupré equation is valid for perfect interfaces only and the behaviour of a droplet on real surfaces can differ.

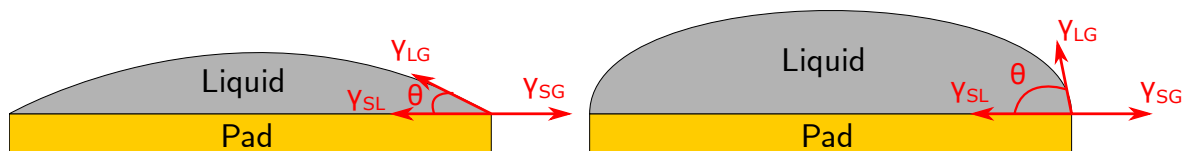


Figure 2.4: Scheme of a droplet with a low (left) and high (right) contact angle.

2.4.1.2 Droplet nature

Various liquids can be used to form the droplet, the main ones being water, liquid adhesives and molten alloys. The two main figures of merit of the liquids are their surface tension

and viscosity. A higher surface tension results in higher capillary forces and better alignment accuracy and yield. Indeed, there is less risk of the liquid under or overflowing and of the friction forces between the substrate and the component interfering with the alignment. A higher viscosity makes the process longer. However, high placement accuracy have been reported with adhesives with a high viscosity [56]. The viscosity and surface energy of some liquids are displayed in Table 2.1.

Water is the most commonly used liquid in self-alignment processes. It is abundant, cheap, liquid at room temperature and has a high surface tension and a very low viscosity. As mentioned earlier, its wettability can be very high on polar surfaces. It can be increased further by the means of plasma treatment [57]. Water is suitable for direct bonding [58, 59, 60], but it cannot be used to bond cells on a glass substrate.

The physical and chemical properties of adhesives can vary significantly. Nonetheless, they share a high viscosity and a low surface tension. The main advantages of these liquids are the flexibility of the cure which can be tuned to protect fragile components, the formation of a strong bond between the die and the substrate and the possibility to use electrically conductive adhesives.

Molten metal alloys have an extremely high surface tension and a low viscosity. They can be used to form a strong bond and an electrical path between the dies and the substrate at the same time, making them particularly suited for micro-electronics and for our application. Low-melting temperature solders are often desired to simplify the manufacturing and prevent heat sensitive components damage. The most common solders used to be near-eutectic SnPb alloys, with a melting temperature below 190°C. For very heat sensitive applications, eutectic Tin/Indium or Tin/Bismuth [61, 62] solders can be used with a melting point of 118°C, but at a higher cost. Nowadays, The European restriction of the use of certain hazardous substances (RoHS) [63] prohibits the use of certain solder materials like lead. The cheaper, most widely available lead-free solders are near-eutectic Tin/Silver and Tin/silver/copper alloys, with melting points around 220°C. Their mechanical properties, especially thermal cycling fatigue strength are not as good as lead-based solders, but other elements can be added to the alloys to improve them [64, 65, 66, 67].

2.4.1.3 Droplet confinement

One of the crucial parameters to achieve high placement accuracy is the droplet confinement, *i.e.* how well the shape and position of the droplet are defined. A poor droplet confinement can lead to overflow or under-wetting of the liquid, which is detrimental to the placement accuracy. In the end, droplet confinement will change the macroscopic wetting angle of the liquid, significantly increasing it for larger volumes. Droplet confinement can be achieved with either chemical or topographical contrast between the pad and the rest of the substrate. Figure 2.5 shows different techniques. As an example, hydrophobic surfaces can be made with a polymer deposition [59]. A combination of the techniques presented below

can be used and give better results than a single method [68].

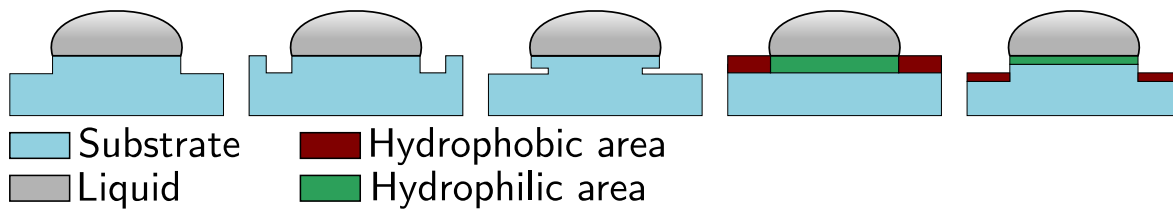


Figure 2.5: Examples of droplet confinement methods using topography and chemical contrasts.

2.4.1.4 Droplet deposition

The droplet deposition techniques can vary a lot depending on the liquid used. An important parameter of the process is the droplet deposition speed, as it will determine the duration of the deposition step. Thus, we chose to divide the droplet deposition methods in two categories, single and parallel deposition. Single-droplet deposition methods are the slowest but also the most reliable and flexible one. Their flexibility comes from the ability to dispense liquids without any viscosity limitation. Usually, automated dispensers are used, with a well-controlled deposition volume and a relatively high deposition speed. Parallel deposition itself covers a large range of techniques. The simpler one would include the use of automated dispenser with multiple dispensing heads, so that the movement of the dispenser is limited and multiple droplets can be deposited at a time (Fig. 2.7(a)). Other techniques aim to realise the deposition on a surface rather than a single pad, using die-coating, blade-coating (Fig. 2.6) or spray-coating.

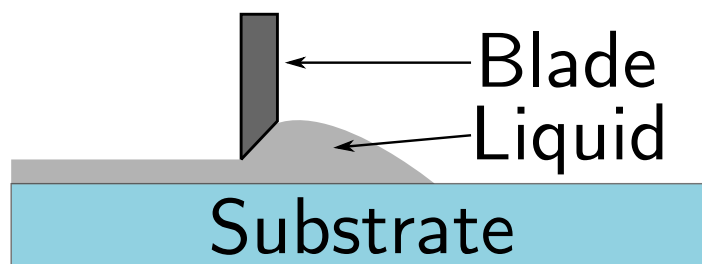


Figure 2.6: Scheme of a blade coating process.

Another method consist of immersing the substrate into water and is called dip-coating (Fig. 2.7(b)). The common point of these methods is that the liquid is dispensed on the whole substrate but only stays on the hydrophilic surfaces (the pads), making these techniques massively parallel. On the other hand, careful substrate preparation is needed, some pads may not receive a droplet and the volume is poorly controlled. Moreover, only low viscosity liquids can be used, such as water.

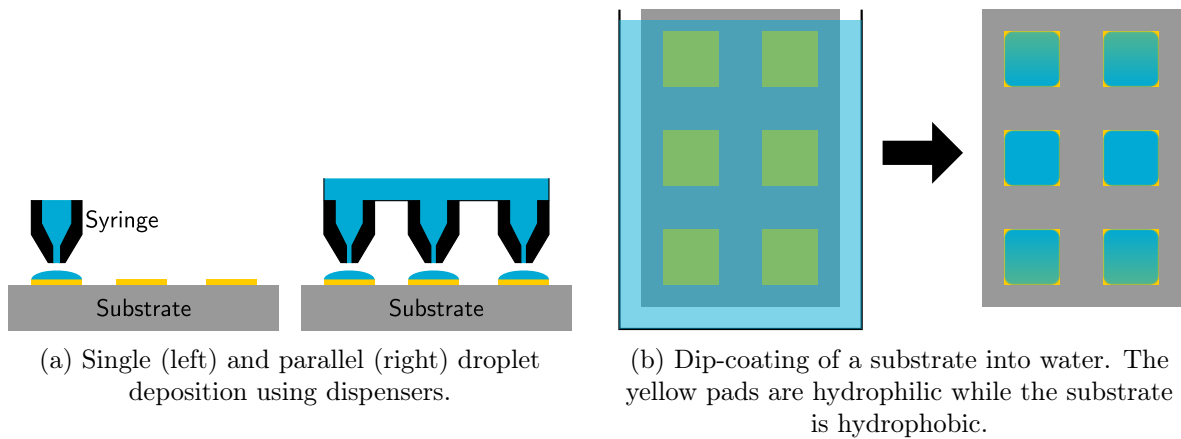


Figure 2.7: Schemes of a few droplet deposition methods.

2.4.2 Receiving pad

The pad size, edge definition and shape all influence the placement accuracy. The pad should have exactly the same size and shape as the die to achieve the highest accuracy and yield [69]. On a side note, different pad/die shapes change the accuracy: hexagonal pads give better results than square and triangular ones [70]. Moreover, the pad edges should be well-defined, *i.e.* the jaggedness should be low (see Fig. 2.8 for a scheme). However, the tolerance is relatively high for rectangular pads with a jaggedness amplitude of 15 μm leading to an alignment error of less than a micron [71].

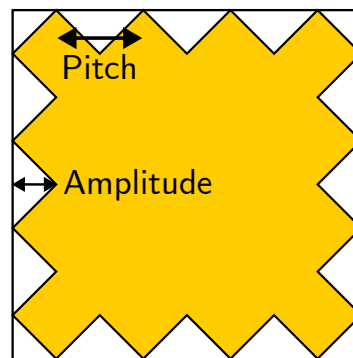


Figure 2.8: Illustration of a square pad jaggedness.

The pad material choice strongly depends on the liquid used, as it should match its polarity and have a high surface energy. For liquid metals, a metal pad should be used. The surface energy of some metals is listed in Table 2.1. Most metals tend to spontaneously get oxidised in air, polarising the surface and significantly decreasing the molten metal wettability. It is possible to remove the native oxide with chemical or mechanical treatments, but the oxide layer is usually extremely fast to form [72, 73]. For this particular reason, printed circuit boards receive a gold surface finish to prevent oxide formation, even if its surface energy is not the highest.

The topography of the pad can have a high impact on the wettability. On a rough surface,

such as black silicon [74], the droplet can be standing on the highest asperities of the surface, increasing its contact angle. The droplet is said to be in the Cassie-Baxter state [75]. Surface roughness can also have an impact on wetting hysteresis [76]. Ideally, the surface roughness should be as low as possible to prevent the Cassie-Baxter state and stay close to the contact angle predicted by the Young-Dupré equation.

Material	Au	Cr	$SnAg_3Cu_{0.5}$	Water	Epoxy (uncured)
Surface energy (N/m)	1.5 [77] 1.506 [78]	3 [77] 2.3 [78]	0.55 (600 K) [79]	0.07	0.04 [80] (25°C)
Viscosity (mPa.s)	/	/	2.7 (500 K) [81]	1	1000 [80]
Melting point (K)	/	/	217	273	NA

Table 2.1: Physical properties of some materials for self-alignment.

Additionally, surface contamination can have a massive impact on wettability. Oil contamination on metal pieces is known to lead to poor adhesive bonds. Substrates are typically cleaned with chemicals like ethanol and acetone to remove organic contamination from the surface. What's more, a plasma treatment is often used to clean or to improve the hydrophilic nature of a surface, resulting in stronger adhesive bonds. Different gas can be used for plasma treatment, yielding different results. Oxygen and air plasma tend to oxidise the surface [82, 83, 84], even gold, greatly improving their hydrophilic nature but significantly decreasing a liquid metal wettability. Argon plasma seem to be a better solution [85], but the ion bombardment can also impact the surface roughness and thus the wettability [85, 86]. However, good wettability was achieved without requiring those plasma treatments. On a side note, commercially available solder often include some flux which goal is to clean the surface and promote wettability.

2.4.3 Component and component feeding

The shape and nature of the component itself has an influence on the self-alignment process. Cuboid components are the best suited for surface tension-driven self-alignment [69]. They should preferably be light to minimise the influence of gravity. Lastly, their chemical nature should match the one of the liquid used to ensure better wettability.

Similarly to single-droplet deposition, single-component feeding consists in placing the components one by one, for example using a P&P machine. It has the same advantages and drawbacks, namely a high flexibility but a low throughput compared to parallel processes. It is worth noting that the initial positioning of the component (before the self-alignment step) can be done with a high and controlled accuracy. Most techniques involve placing the component on top of the substrate. Nonetheless, successful self-alignment was achieved by doing the opposite, picking the component by putting the substrate on top of it [87].

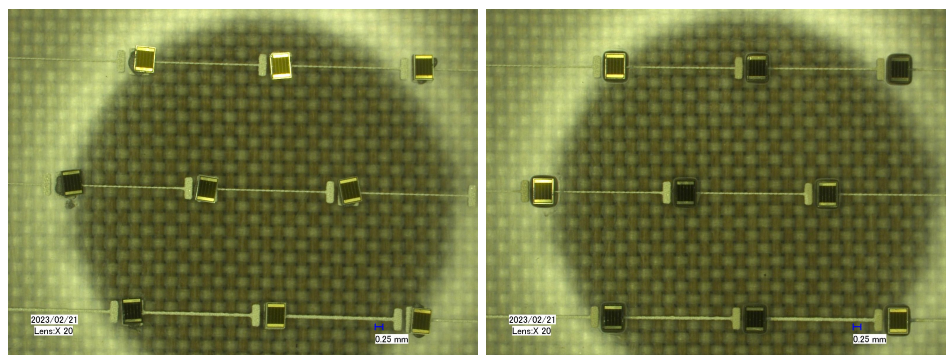
As its droplet deposition counterpart, parallel component feeding consist of placing multiples components during the same step. This can be achieved using P&P with different tools, which will be similar to the scheme in Fig. 2.7(a). Transfer printing is another method to place components in a massively parallel fashion, although it is used as a complete alignment process and not a feeding one [88]. It should be noted that it has been used to make micro-concentrators [89].

2.4.4 Conclusion of the state of the art

Many different self-alignment methods exist and have been studied. By comparing each of them and taking the requirements into account, surface tension-driven processes came out as the best option. Among its variations, using a molten solder as the liquid and metal as the receiving pad was considered to be the best option. Indeed, since the cells will be bonded on a glass substrate, adding metal receiving pads will ensure a very high chemical contrast between the pad and the substrate, as well as some topography contrast. Moreover, the rearside of the cells must be electrically connected. A conductive adhesive would also work, but from the state of the art, liquid metals work better with self-alignment because of their high surface energy. Furthermore, they exhibit high wettability on other metals. Lastly, the solar cells are cuboid, which is a shape that works nicely with the surface tension-driven process.

In the end, a self-alignment process with molten solder strongly bonds the cells on the substrate, makes the electrical connection with the rearside of the cells and align them with a high precision, all in one reflow step. Thus, we chose to study this process in further detail. Surface tension-driven self-alignment has been studied extensively, as shown in this section. However, it is still not fully understood, which hinders its industrial development. In particular, the precise effect of the liquid volume and the receiving pad dimensions tolerances are not well-known. Furthermore, the process must be suitable for the substrate and solar cells used in this thesis and should possibly be adapted.

To sum up, we chose a capillary self-alignment process with a molten solder, cuboid components, parallel solder deposition, single component feeding with P&P and metal pads with a gold surface finish.



(a) Microscope picture of the solar cells before reflow. (b) Microscope picture of the solar cells after reflow.

Figure 2.9: Experimental example of micro solar cells self-alignment with a molten solder.

As an example, self-alignment tests performed with manually dispensed solder and manually placed solar cells are shown in Fig. 2.9. The cells were positioned with an initial accuracy of about 200 μm and the $\text{SnAg}_{3.0}\text{Cu}_{0.5}$ solder volume was poorly controlled. Still, they all seem to be aligned from a qualitative inspection.

2.5 Experimental process

The molten solder surface tension self-alignment process flow is presented in Fig. 2.10. In step one, the cells are packaged on a dicing tape. Simultaneously, the receiving pads and tracks are printed on the glass substrate. The second step consists of applying the solder paste on the pads. In this example, stencil-printing is used. Then, the cells are placed on the solder paste with a P&P machine that can work at its full speed. At the end of this step, all the cells are roughly positioned on the receiving pads. The last step is the reflow. The solder paste particles melt and the self-alignment takes places. Once the samples have cooled down, the cells are precisely positioned and strongly bonded on the receiving pads. Experiments were conducted at CEA-Leti.

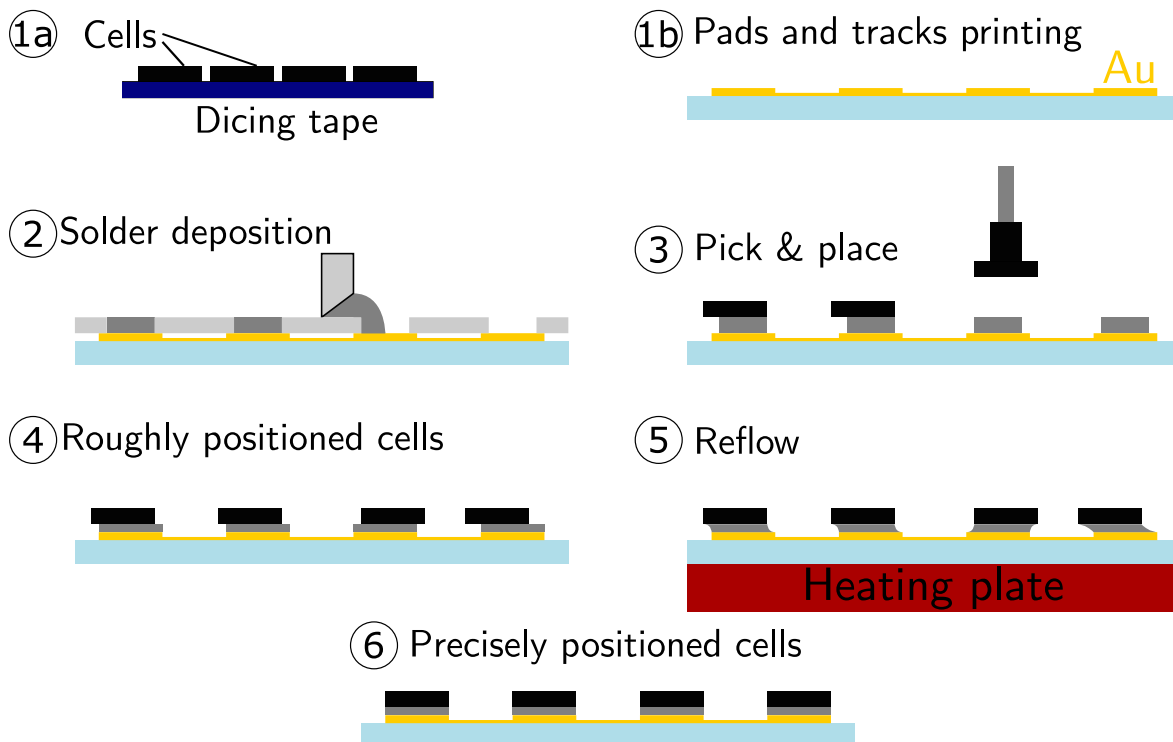


Figure 2.10: Scheme of the process flow for the self-alignment of micro-solar cells.

Based on the state of the art, a few process parameters can already be defined and do not need further investigation.

Since the cells are cuboids, the pads should be rectangular with the same dimensions at the cell rearside. The cells will be soldered, so the pads should be made of metal with a gold surface finish to prevent an oxide layer forming. The solar cells should not be heated too much to avoid any degradation during soldering, so a low-melting point solder is preferred. Even if

RoHS allows the use of lead-based solders for energy production applications, it was decided to use lead-free solders out of concern for personal and environmental safety. To reduce solder costs, the standard so-called SAC305 ($\text{SnAg}_{3.0}\text{Cu}_{0.5}$) solder will be used. This solder is also known for its good thermal cycle reliability [61]. The reflow thermal cycle depends on the solder used and will not be studied. Instead, manufacturer guidelines will be followed. The corresponding temperature profile can be found in the appendix (Fig. B.1(a)).

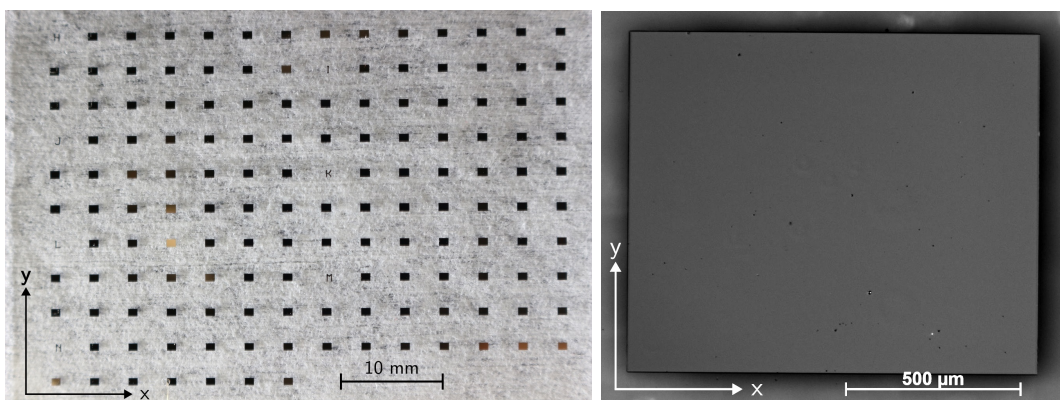
In the end, we chose to study the influence of the solder volume, the cell initial placement before reflow and the receiving pad size. The studies were performed in the framework of a partnership with the Fraunhofer Institute for Solar Energy Systems (ISE) and the topics were divided between the two institutes as summarised in Table 2.2.

Institute	Pad size tolerances (μm)	Solder volume (nL)	Pad pretreatment
CEA	Cell size $\pm 0, 10, 20, 50$	23, 46	Yes
ISE	Cell size -27, -92, +41	28, 33, 38, 44	NA

Table 2.2: Summary of the self-alignment topics of study of both ISE and CEA.

2.5.1 Receiving pads

The receiving pads were manufactured with Physical Vapour Deposition (PVD) and a lift-off. More precisely, photolithography with chrome (Cr) on glass masks was performed on glass substrates. Then, metal layers were deposited in an evaporation chamber with a crucible. The final stack from bottom to top is 10 nm of Cr, 300 nm of Cu and 15 nm of Au. The Cr is used to promote adhesion between the Cu and the glass. The thin Au layer prevents surface oxidation that would be detrimental to the solder wettability. PVD and photolithography were used because of their high dimensional accuracy (1 μm resolution) needed for the pad size study. The quadratic surface roughness was measured with a profilometre and was equal to 1.47 nm. A picture of a substrate and a close-up of a pad are shown in Fig. 2.11. For each size, 20 pads were manufactured.



(a) Picture of a substrate with pads.

(b) Microscope picture of pad made with PVD.

Figure 2.11: Examples of PVD pads.

2.5.2 Solder stencil-printing

Prior to solder deposition, the substrates with the receiving pads were cleaned with acetone first and then with isopropanol as acetone tends to leave marks.

The $\text{SnAg}_{3.0}\text{Cu}_{0.5}$ solder pastes were deposited on the receiving pads using stencil printing with a DEK machine (picture in Fig. 2.12). This technique achieves a precise solder volume control and a high throughput.

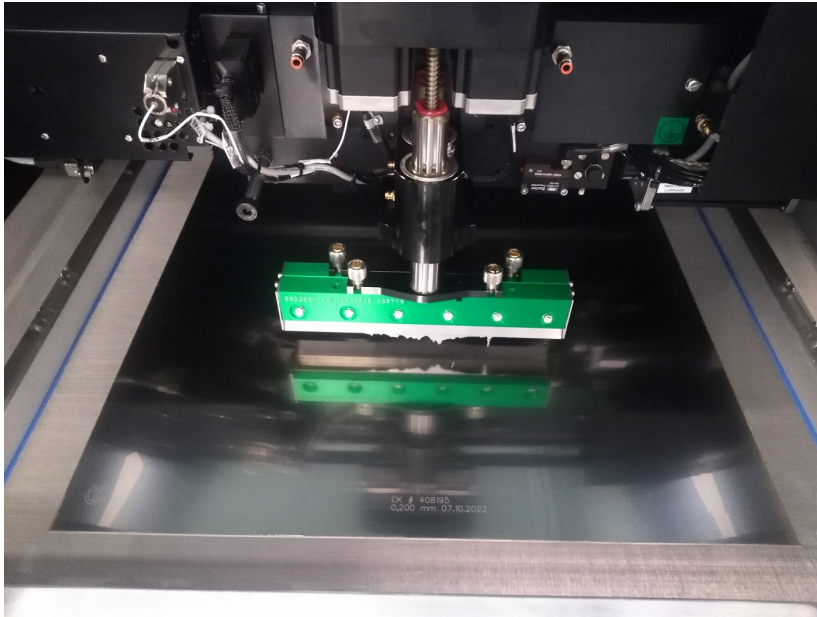


Figure 2.12: DEK stencil-printing machine at CEA-Leti.

Two stainless steel stencils A and B were used to deposit two different solder volumes on the pads. The stencil geometry is described in Table 2.3. The openings are 50 μm smaller than the smallest corresponding pads ($835 \times 635 \mu\text{m}$) to prevent solder paste overflow during stencil printing.

Stencil	Paste	Opening size (μm)	Stencil thickness (μm)	Opening volume (nL)	Reference
A	T3	784x584	100	46	A-T3
B	T3	784x584	200	91	B-T3
A	T6	784x584	100	46	A-T6

Table 2.3: Summary of the experiments parameters.

Two solder pastes of the same alloy were used, the difference between the two is the flux and the solder particle size. According to the manufacturer, the T3 paste particles range from 20 to 45 μm [90] and the T6 paste particles from 5 to 20 μm [91]. The flux composition is not detailed. According to the manufacturer, both particle sizes are compatible with the opening sizes that were used.

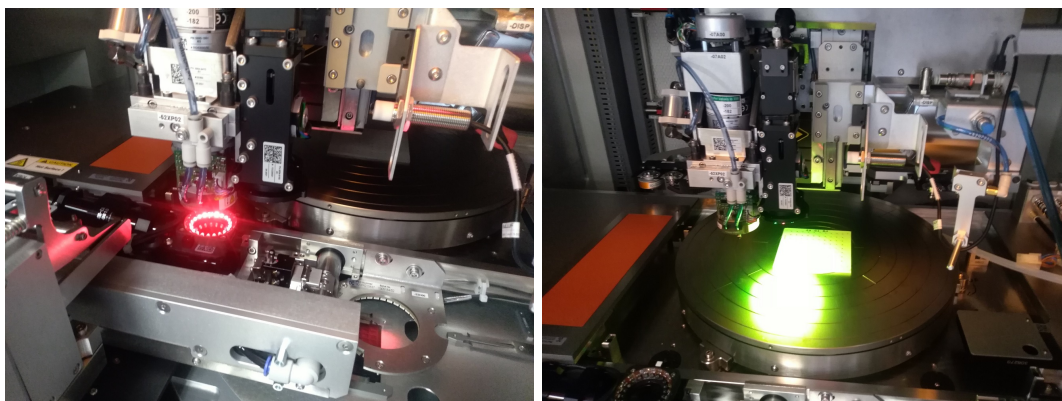
The stencil-printing process settings are the forward speed of the squeegee, the pressure applied to the stencil by the squeegee and the demoulding speed, *i.e.* the speed at which the stencil is moved away from the substrate. These parameters depend on the paste and the geometry of the openings. They are determined empirically by trial and error and are summarised in Table 2.4.

Reference	Forward speed (mm/s)	Pressure (kg)	Demoulding speed (mm/s)
A-T3 B-T3	25	5	7
A-T6	25	6	7

Table 2.4: Stencil-printing parameters.

2.5.3 Solar cells initial placement

The solar cells were placed on the substrate with a Datacon 2200 evo advanced P&P machine. According to the manufacturer, the placement accuracy reaches $3\ \mu\text{m}$ 99.7% of the time [92]. Figure 2.13 shows pictures of the machine at work. Figure 2.13(a) shows the recognition of the picked cell and Fig. 2.13(b) the recognition of the substrate fiducials. The first step is done for each cell and the second one every few cells.



(a) Chip recognition step.

(b) Fiducial recognition step.

Figure 2.13: Datacon P&P machine used at CEA-Leti.

All cells except from half the T6 experiments (see Table 2.3) were initially placed in the middle of the pad, according to the machine tolerances. In the T6 experiments, half the cells were also placed with an initial offset of $100\ \mu\text{m}$ in the x direction.

2.5.4 Means of characterisation

The final position and in-plane orientation of the cells were characterised by optical microscopy with a motorised stage. The fiducials on the substrate were set as the reference

points. Then, the position of the corners of the cells were measured with respect to it. Because of the pads layout, it was not possible to measure the out-of-plane rotation with a side-view of the cells. Indeed, they are all aligned and only the closest ones to the substrate edges would be visible. Instead, 3D reconstructions were made with a Keyence digital microscope. The rotation was then calculated from the height difference between the lowest and highest point of the cell. This technique is particularly time consuming compared to in-plane characterisations, so only the rotation of a few cells was measured this way. Pictures of substrates after the cells placement is shown in Fig. 2.14.

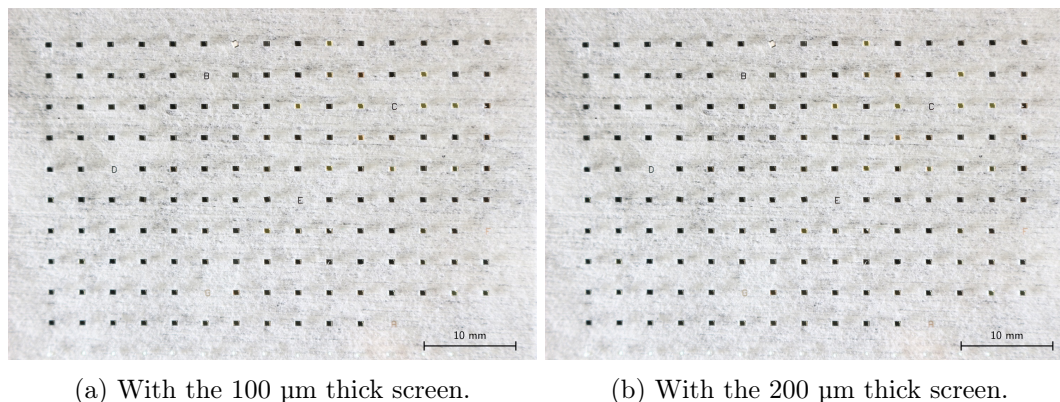


Figure 2.14: Pictures of two substrates after the $885 \times 685 \mu\text{m}$ cells placement using the T3 paste.

2.6 Simulation models

As a way to explain the experimental results, an analytical and a numerical model were developed to calculate the capillary forces acting on the cell during self-alignment. The goal is to compare both the CEA-Liten and ISE experimental results with the simulations. Having two different ones allows to verify the calculated values and check their limitations. Both models, presented in the upcoming section, are based on an energy approach and only give steady state results. Thus, the dynamics of the self-alignment are not taken into account.

2.6.1 Analytical model

A scheme of the model is presented in Fig. 2.15. Considering that the cell and pad have the same width, the system can be represented in 2D as shown below. The chip (in red) rest on a solder layer (in grey) with a thickness h . The solder is assumed a trapezoid and its volume is noted V . The solder rests on the receiving pad (in yellow). To simplify the problem, the contact lines of the the solder will be considered pinned on the pad and cell edges. The cell, respectively pad length is noted C_L , P_L . The difference $P_L - C_L$ is noted ΔL . The width of both is noted W . The dimensions can be found in Table 2.5. The cell offset or displacement is the distance between the pad and the cell centre. The displacement of the cell in the y direction was assumed equal to 0. The rotation of the cell was not considered.

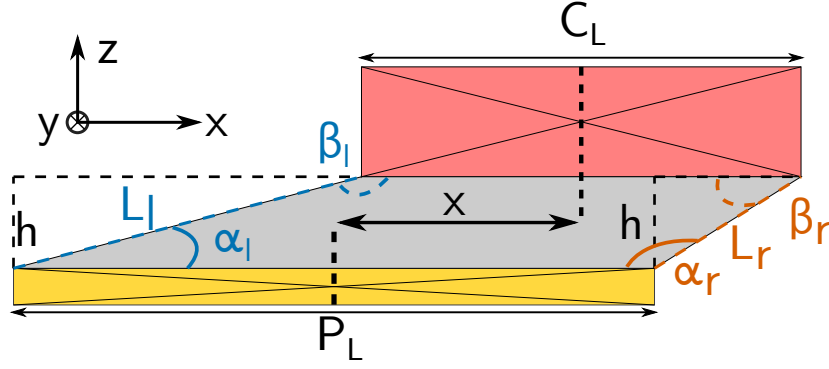


Figure 2.15: Scheme of the problem.

The energy of a side i can be expressed as the product of the surface tension by the corresponding surface:

$$E_i(x) = \gamma \times W \times L_i(x) \quad (2.2)$$

L_i is the solder flank length on a side i .

On a side i , the capillary force F_i can be expressed as:

$$F_i(x) = \frac{-dE_i(x)}{dx} \quad (2.3)$$

In the end, on the left side:

$$F_l(x) = -\gamma \times W \times \frac{x - \frac{\Delta L}{2}}{\sqrt{(x - \frac{\Delta L}{2})^2 + h^2}} \quad (2.4)$$

And on the right side:

$$F_r(x) = -\gamma \times W \times \frac{x + \frac{\Delta L}{2}}{\sqrt{(x + \frac{\Delta L}{2})^2 + h^2}} \quad (2.5)$$

The total force F_t is the sum of F_l and F_r . It is then possible to calculate the solder angle on the pad or on the cell. As an example, the solder contact angle on the left side of the pad α_l is expressed as:

$$\alpha_l(x) = \arccos \left[\frac{x + \frac{\Delta L}{2}}{\sqrt{h^2 + (x + \frac{\Delta L}{2})^2}} \right] \quad (2.6)$$

And since the solder layer is a trapezoid:

$$h = \frac{2V}{W(P_L + C_L)} \quad (2.7)$$

The details of the equations can be found in the appendices.

2.6.2 Numerical model

A numerical model was built using the Surface Evolver software, a free tool made by K. Brakke [93]. A screenshot of the model is shown in Fig. 2.16. The geometry of the system and the conventions are the same as in the analytical model. Since the metal receiving pad is on a glass substrate and the cell edges have no metallisation, there is a high wettability contrast between the pad and the substrate and between the cell rear side and its edges. The corresponding applied boundary conditions are listed below:

- No solder overflow beyond pad limits.
- No solder overflow beyond cell limits.
- The solder cannot go above the bottom face of the cell.

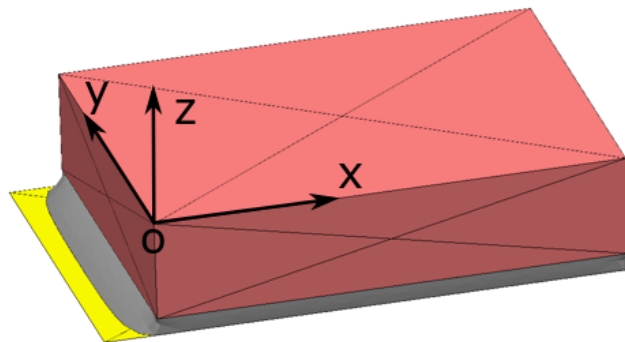


Figure 2.16: Screenshot of the numerical Surface Evolver model.

The solder surface is divided into facets which size is user-defined. The solving algorithm is based on an energy approach. First, the total energy of the system is calculated by summing the energy of the individual facets. Then, a small perturbation is applied on the facets to determine which direction of motion would decrease the total energy of the system. Afterwards, the facets are moved by an arbitrary factor in the direction determined previously. The number of iteration is defined by the user.

The input parameters are listed in Table 2.5. The liquid contact angle was estimated from several references [94, 95, 96, 97] to get a reasonable value.

Parameter	Default value
Liquid surface tension ($10^2 dg.s^{-2}$)	0.5 [98]
Liquid density (dg/mm^3)	7.5×10^{-4} [79]
Pad/liquid contact angle ($^\circ$)	30
Chip/liquid contact angle ($^\circ$)	30
Gravity acceleration ($mm.s^{-2}$)	9800
Liquid volume (mm^3)	0.04
Chip dimensions ($x \times y \times z$, mm)	$0.855 \times 0.685 \times 0.19$
Pad dimensions ($x \times y$, mm)	0.855×0.685
Chip density ($dg.mm^{-3}$)	5×10^{-4} (exp)

Table 2.5: Parameters used in the simulations.

To prevent some computations issues, there are no solder facets on the pad or cell surface. Instead, an energy integral is calculated. It corresponds to the solder surface tension multiplied by the surface described by the solder edges. The topography of the surface is only taken into account *via* the contact angle.

2.7 Results

2.7.1 Solder volume influence

The first step was to compare the placement accuracy for the two solder volumes (experiments A-T3 and B-T3). Figure 2.17 and Figure 2.18 show the final displacement in x , respectively y direction as a function of the pad size for the two stencil thicknesses. A quick overlook shows that using a higher solder volume results in a larger final displacement. The displacement range can be as high as 200 μm and the cell clouds are not centred on the 0 position. On the other hand, with the lower solder volume, the cell clouds are centred on the 0 position and their dispersion is lower. The displacement range is about 150 μm in the worst case and the maximum displacement is equal to 120 μm .

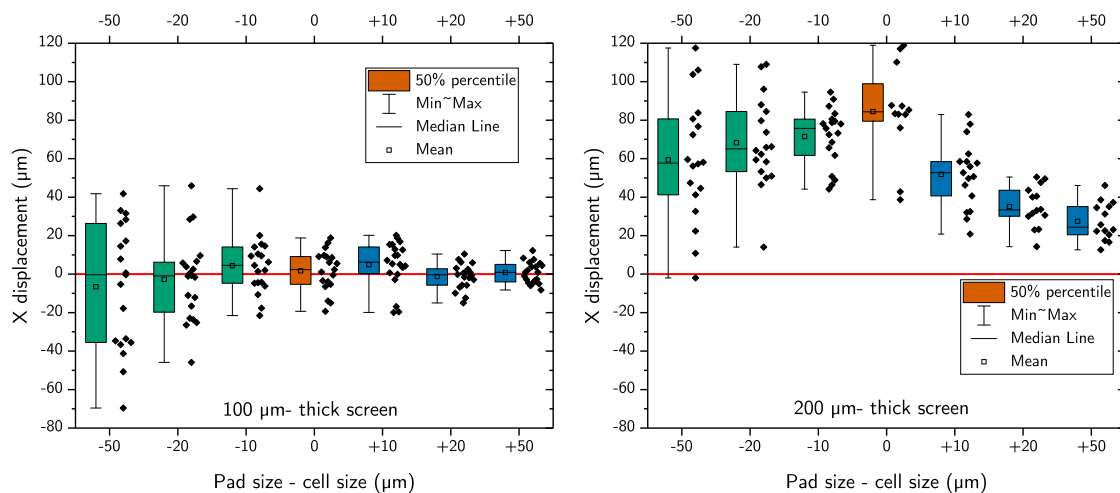


Figure 2.17: Final displacement along the x -axis for the 100 μm thick stencil (left) and the 200 μm thick stencil (right) with the T3 paste. Compared to the cell size, smaller pads are green, identical ones orange and larger ones blue.

Moreover, focusing only on the lower solder volume graphs, the final displacement is higher when the pads are smaller than the cells. The displacement also seems lower when the pads are larger than the cells, although this trend is less clear. However, according to the state of the art, the pad equal in size to the cell should yield the best results. The experimental results can most likely be explained by the large solder volume used compared to the pad size.

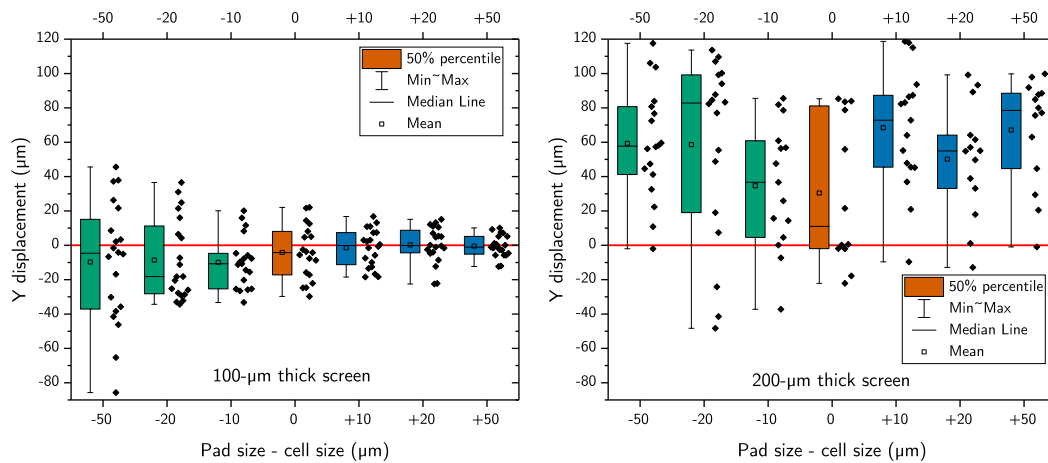


Figure 2.18: Final displacement along the y -axis for the 100 μm thick stencil (left) and the 200 μm thick stencil (right) with the T3 paste. Compared to the cell size, smaller pads are green, identical ones orange and larger ones blue.

Figure 2.19 shows a cell after reflow for the T3 paste with the 200 μm thick stencil and the T3 paste with the 100 μm thick stencil. The focus is on the substrate surface. The 200 μm stencil picture exhibits a so-called solder pillow on the right side of the cell. During the reflow, when the solder is liquid, the cell rests on a pseudo-spherical surface. Thus, a small displacement can cause the cell to slip on the side of the sphere, causing a large translation and a large out of plane rotation. The solder pillow forms when the solder volume to the pad size ratio is high enough. In these experiments, it happens with the thicker screen and any pad sizes as well as with the thinner screen with the smaller pads.

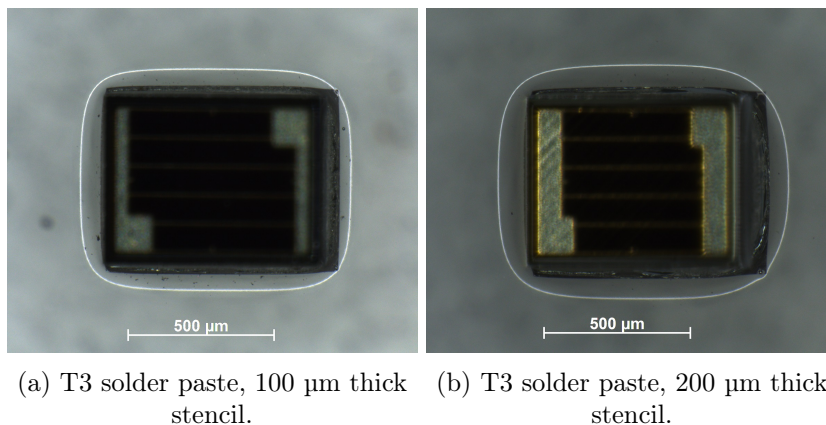


Figure 2.19: Pictures of the solder paste on the pads after reflow.

Figure 2.20 shows the in-plane rotation of the cells after the reflow process for both stencils. As opposed to the in-plane translations, there is no clear trend when it comes to the rotation. The pad size or the solder volume seems to have little influence on it. It is worth mentioning that the highest rotation measured is of 6° , which is relatively small.

From these results it was decided to perform the following T6 experiments with the 100 μm

thick stencil only. Instead of testing two volumes, half the T6 experiments were realised without an initial cell placement offset and the other half with a 100 μm offset.

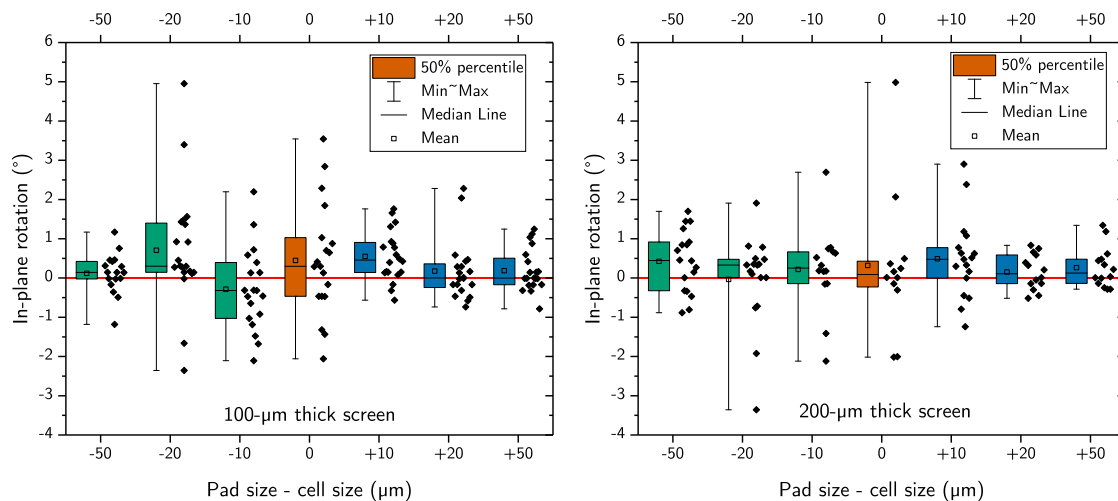


Figure 2.20: Final in-plane rotation for the 100 μm thick stencil (left) and the 200 μm thick stencil (right) with the T3 paste. Compared to the cell size, smaller pads are green, identical ones orange and larger ones blue.

2.7.2 Initial displacement influence

Experiments A-T6 were performed with the T6 paste and the 100 μm thick screen only. As opposed to the T3 experiments, some cells were placed on the pads with an initial offset of 100 μm before reflow. Figure 2.21 and Fig. 2.22 show the final x , respectively y direction displacement for the cells from the T6 experiments, as a function of the pad size.

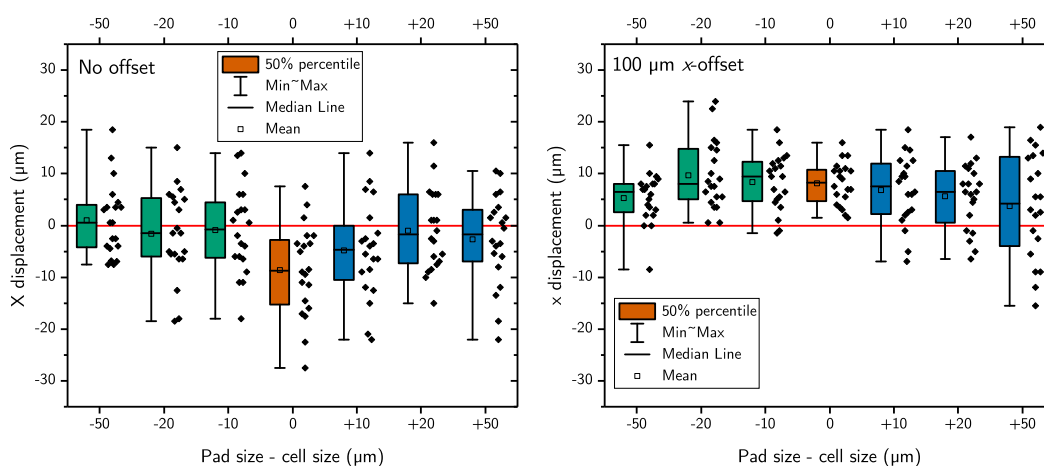


Figure 2.21: Final displacement along the x -axis for the cells placed without offset (left) and with 100 μm x -offset (right) with the T6 paste. Compared to the cell size, smaller pads are green, identical ones orange and larger ones blue.

First, the maximum displacement does not exceed $30\ \mu\text{m}$ for the whole 140 cells. The final displacements with and without an initial $100\ \mu\text{m}$ offset are in the same range, but the initial offset seems to induce a higher displacement in the corresponding x direction. Indeed, the point clouds are not centred on the 0 position but displaced in the positive x values. However, the initial offset substrates also show a smaller scattering than the ones without the offset. A possible explanation is that the capillary forces of the solder are high enough with an initial displacement to start the move back towards the pad centre, resulting in more similar values.

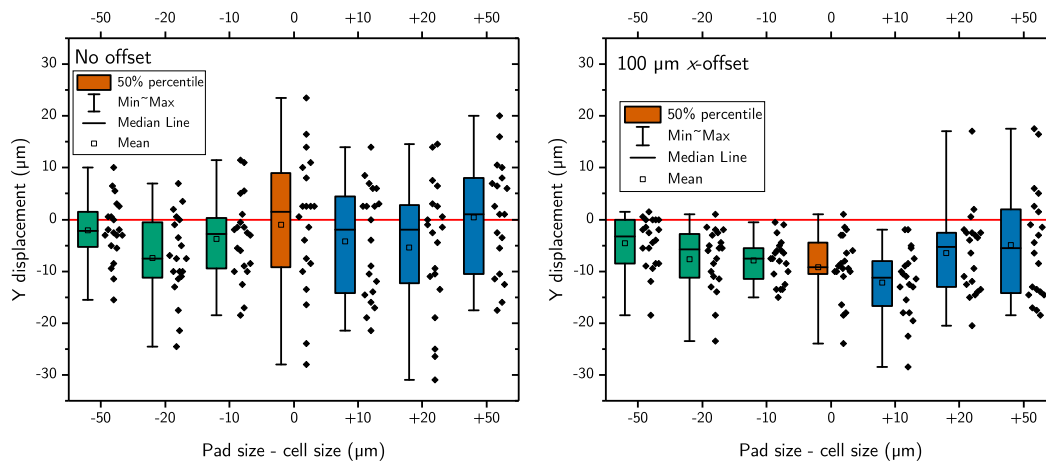


Figure 2.22: Final displacement along the y -axis for the cells placed without offset (left) and with $100\ \mu\text{m}$ x -offset (right) with the T6 paste. Compared to the cell size, smaller pads are green, identical ones orange and larger ones blue.

Similar conclusions can be made regarding the in-plane rotation (Fig. 2.23). The rotation reaches 3° for the $+50\ \mu\text{m}$ pads and the initial offset.

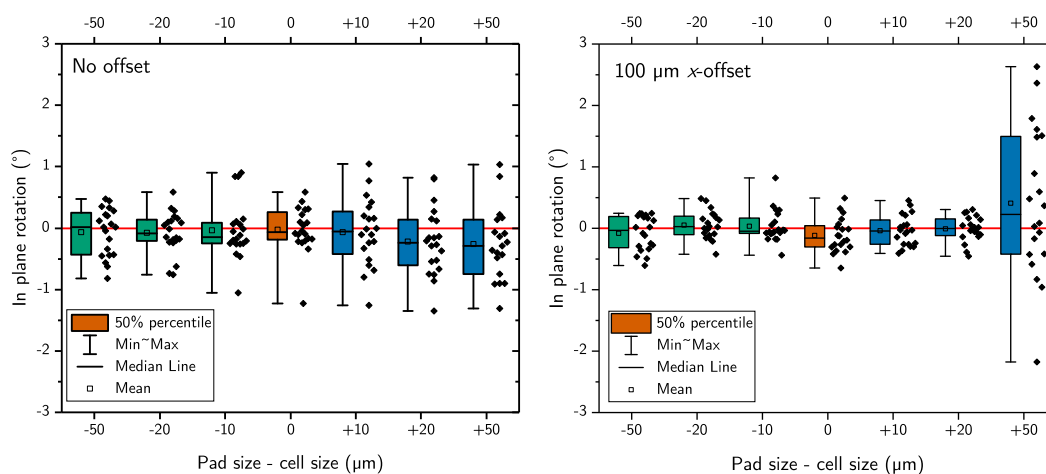


Figure 2.23: Final in-plane rotation for the cells placed without offset (left) and with $100\ \mu\text{m}$ x -offset (right) with the T6 paste. Compared to the cell size, smaller pads are green, identical ones orange and larger ones blue.

For all the other cells, the rotation does not exceed 1° . The initial offset also decreased the final rotation and its scattering, except for the largest pads.

From the T6 experiments, it is also hard to conclude anything regarding the pad size. The largest pads seem to be more sensitive to in-plane rotation, but not much can be said from the in-plane translations measurements.

Finally, looking at the out-of-plane rotation of the cells in Figure 2.24, an increased pad size and an initial offset improved the self-alignment. The increasing pad size influence can be attributed to the decreasing volume per surface and the formation of a solder pillow.

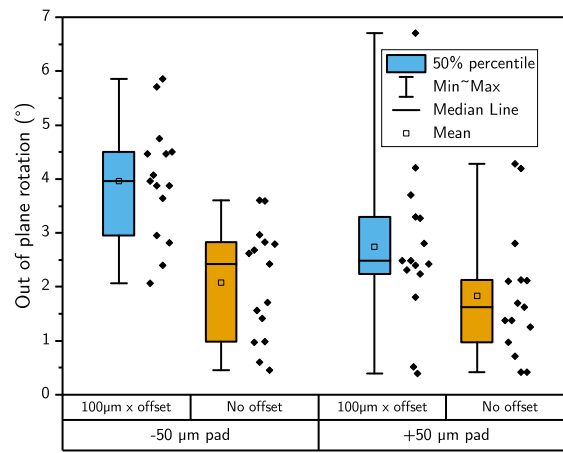


Figure 2.24: Final out-of-plane rotation for the cells placed on the smallest and largest pads, with (blue) and without (orange) a $100\ \mu\text{m}$ offset with the T6 paste.

Both the solder volume and initial displacement results can be linked to the capillary forces simulations. Figure 2.25 shows the capillary forces as a function of the cell displacement in the x direction for the analytical (lines) and numerical (points) models. The green and orange plots represent the forces for two different solder volumes, 20 and 40 nL. In both cases, the pad length is equal to the cell length and to $885\ \mu\text{m}$. The blue curves represent the forces for the same solder volume as the green curve (20 nL) but for a longer pad length of $985\ \mu\text{m}$. In the three cases, both the analytical and numerical models show good agreement for small displacement with no more than 9.1% relative discrepancy at $50\ \mu\text{m}$. The differences between the models get more significant as the displacement of the cell is larger, reaching 10% relative discrepancy at a $100\ \mu\text{m}$ displacement. This can be explained by the assumptions of the analytical model. As the displacement gets larger, the solder edges are not pinned to the cell pad or cell edges anymore. Nonetheless, in the range of 0 to $100\ \mu\text{m}$ displacement, both models give similar results.

In all cases, the total force curves are strictly increasing with the displacement. For the same pad length (green and orange curves), the force is lower if the solder volume is higher for all displacement values.

However, for the same volume, if the pad and cell lengths are different (blue curves), the shape of the force versus displacement curve changes. Nonetheless, the $\Delta_L \neq 0$ curve is always below

the $\Delta L = 0$ one. Furthermore, the asymptotic force at high displacements stays the same.

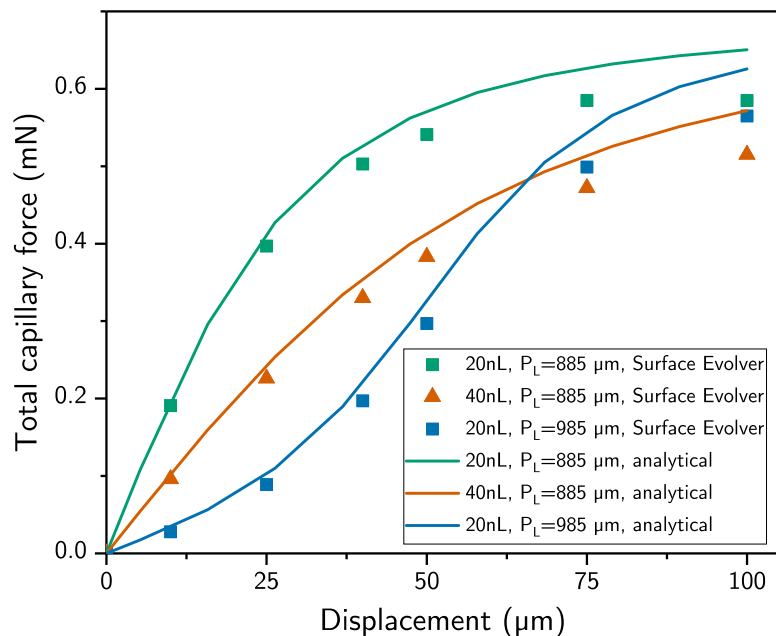


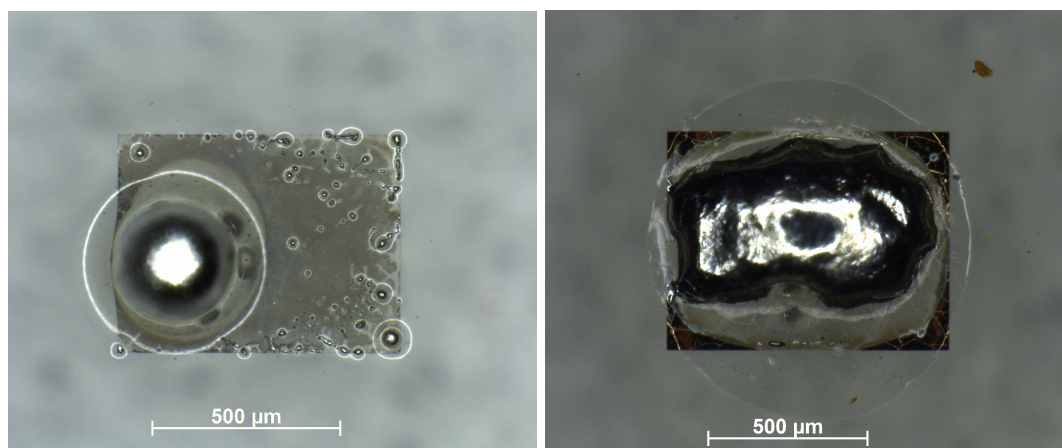
Figure 2.25: Total capillary forces as a function of the cell displacement calculated with the analytical model (lines) and the numerical model (symbols) for two different solder volumes and pad sizes.

From these first simulations results, a higher initial displacement induces higher initial forces. The experiments previously presented show that the self-alignment accuracy is better with an initial displacement of 100 μm compared to no intended initial displacement. It is important to bear in mind that the P&P accuracy results in a small initial displacement anyway. Besides, the experiments also seem to indicate that a lower solder volume/pad surface ratio yields a higher self-alignment accuracy. Similarly, the simulations show that the forces are lower for a higher solder volume. Then, one can assume that in the 100 μm initial displacement case, the initial forces are high enough to set the system in motion and start the self-alignment process. When no initial displacement is applied, the forces are initially too low to start moving the cell.

2.7.3 Solder paste influence

Comparing the final displacement measured for the T3 and T6 experiments with the same 100 μm thick screen, the accuracy is much higher with the T6 paste, whether looking at the translations or rotation. A possible explanation lies in the solder paste wettability. Figure 2.26 shows solidified solder droplets on a pad after the reflow step for the T3 and T6 pastes. First, the wettability of the T3 paste is extremely poor as the solder formed a ball on the pad. Second, the pad appears to be badly damaged after the reflow and most of the metal ripped out from the glass. However, all the solder balls are contained within the original borders of the pad. The wettability is better with the T6 paste but still poor. The solder spread further but the wetting is quite high judging from the picture. Moreover, the edges of the pad are

not wet at all. A possible explanation for the pad damage is that the bond between the pad and the glass is too weak and the metal was ripped by the solder paste itself. However, it does not explain why the T6 paste shows a different behaviour. Another explanation could be the different fluxes. Unfortunately, information about the flux was not available. It is worth noting that after reflow with a cell on top of the solder (Fig. 2.19), the solder is almost spread on the whole pad surface anyway.



(a) T3 solder paste.

(b) T6 solder paste.

Figure 2.26: Pictures of the cells on the pads after reflow.

2.7.4 Poor substrate wettability influence

Figure 2.27 shows three screenshots of the Surface Evolver model. To emulate the solder behaviour seen in Fig. 2.26, the cell was removed on the left picture. Furthermore, the pad contact angle was set to 120° in the three cases. The cell contact angle was set to 120° in the middle picture and to 30° in the right one. Without the cell and with a high pad contact angle, the solder wettability is poor and a solder ball is formed as expected. Adding the cell with a high contact angle does not affect this behaviour much and only flattens the top and bottom of the ball. However, if the cell contact angle is low, the solder ends up being almost completely spread on the pad, as seen in Fig. 2.19.

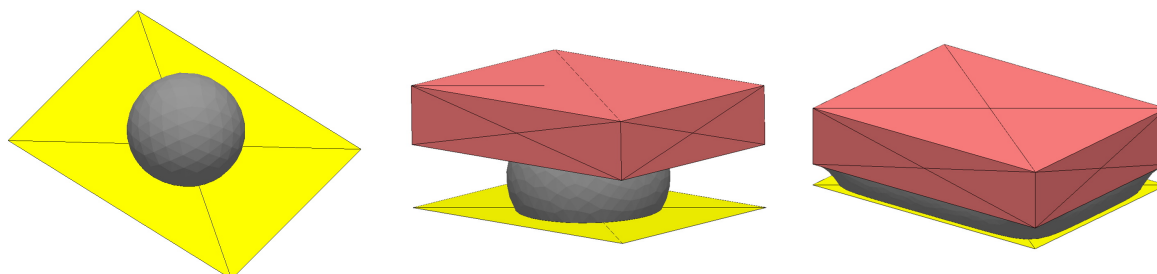


Figure 2.27: Screenshots of the Surface Evolver model. Without cell (left), cell contact angle= 120° (middle) and cell contact angle= 30° (right). In all cases, pad contact angle= 120° .

One can then conclude that the solder wettability on the cell is high and that the pad

wettability does not have as much of an influence than initially thought. High cell wettability is enough to ensure solder spread and self-alignment.

2.7.5 Pad size and initial displacement combined influence

The experimental self-alignment results from the ISE experiments should be briefly presented. Similar conclusions were obtained regarding the solder volume and a small intended initial cell displacement, with a higher accuracy. However, differences were observed concerning the pad size. Those results are shown in Fig. 2.28. Overall, the smaller the pad, the better the placement accuracy was. Moreover, a so-called edge alignment was noticed, with the edge of the cell being aligned with the edge of the pad. This phenomenon was seen for the larger pads with an initial displacement of 100 and 150 μm and for the slightly smaller pads (27 μm smaller than the cells) for an initial displacement of 150 μm only. This hints towards the edge alignment being more likely the larger the pad is and the higher the initial displacement is as well.

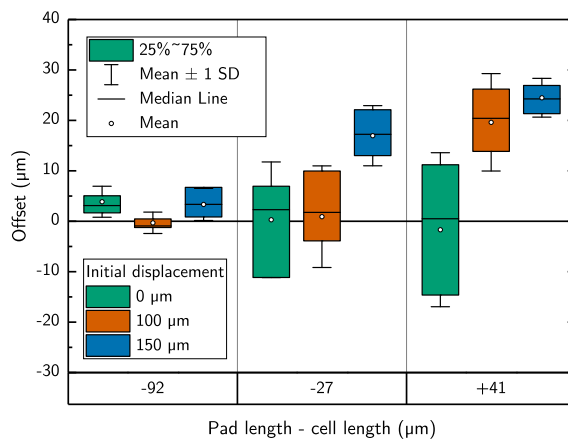


Figure 2.28: Final displacement along the x -axis for the cells placed without offset (left) and with 100 μm x -offset (right) with the T6 paste. Compared to the cell size, smaller pads are green, identical ones orange and larger ones blue. Adapted from [99], results from Fraunhofer ISE.

Previously, the simulated total capillary forces were plotted against the displacement. In Fig. 2.29, the left and right forces are also plotted separately for two pad sizes. When the pad and cell length are the same ($\Delta L = 0$), the solder edges L_l and L_r have the same length for any displacement. Thus, they reach a minimum at 0 μm and the resulting force on both side is equal to 0 mN (Fig. 2.29, left side). However, when the pad is smaller or larger than the cell ($\Delta L \neq 0$, Fig. 2.29, right side), the problem is asymmetrical. The left and right forces reach a minimum for $x = \Delta L/2$ and $x = -\Delta L/2$ respectively, which corresponds to the inflection point of the total force curve. Therefore, the total force variation is slower for small displacements (roughly until $\Delta L/2$) and then faster for larger displacements. More importantly, at 0 μm , capillary forces of opposite signs and same amplitude are still applied

on the cell. Their amplitude is equal to half the maximum total force. In absolute values, the forces are much higher.

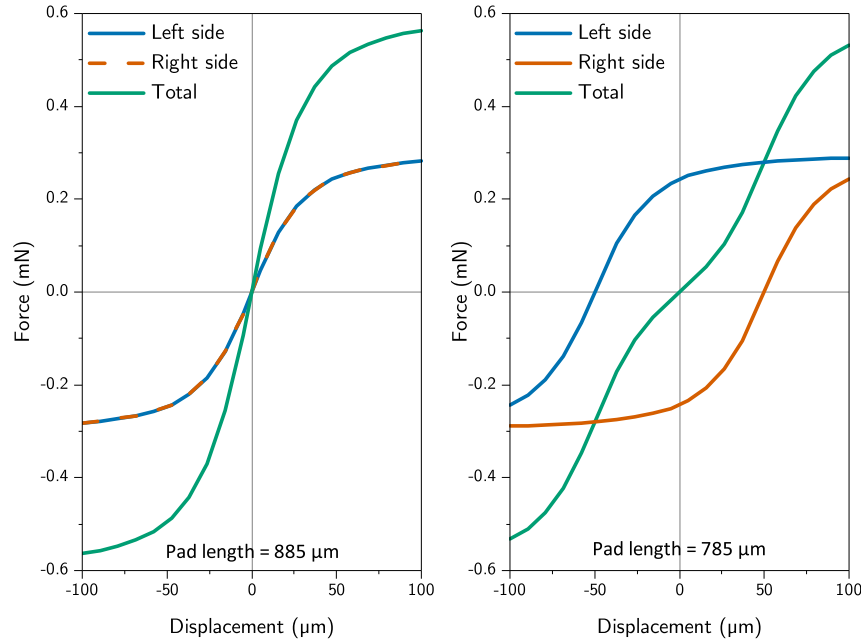


Figure 2.29: Left, right and total forces as a function of displacement for two pad lengths of 885 and 785 μm . Cell size = $885 \times 685 \mu\text{m}$.

Assuming that it makes the most sense to focus on the edge forces and not the total one, when $\Delta L \neq 0$, one can assume that the 0 position of the cell is more stable than when $\Delta L = 0$. However, it is important to notice that in every case, if the solder wettability is enough to ensure complete wetting of the pad and cell, the cell should end up at the 0 position, even for different pad dimensions. Moreover, according to this hypothesis, the largest pads should yield the best self-alignment results, just like the smallest pads. Finally, from those results alone, the initial displacement should not have an impact. In practice, this is not the case as explained from the ISE results earlier [100]. Based on those experiments, it seems like forces alone cannot explain the differences observed between the pad sizes.

The second hypothesis relies on the wetting angle of the solder. In the beginning of this chapter, basic contact angle theory has been presented. In practice, the contact angle can significantly differ from the balanced state one predicted by the Young-Dupré equation. The wetting angle can be made much higher with droplet confinement as shown in Fig. 2.5. In our case, the solder contact angle is roughly equal to 90° when the cell is centred on the pad, which is higher than the 30° expected. However, if the contact angle is lower than expected, the contact line on the pad should move to go back to the balanced state, assuming no wetting hysteresis. Going back to Fig. 2.15, with a positive x -displacement, the angles β_l and α_r will always be well above the expected solder contact angle (30°). On the other hand, the angles β_r and α_l will be under 30° for large displacements and may cause dewetting. Figure 2.30 shows the wetting angle of the solder on the left side of the pad for different pad lengths and

a solder volume of 20 nL. The values were obtained with the analytical model. The wetting angle decreases when the displacement and the pad size increase. With a combination of a high initial displacement and a large pad, dewetting is expected in the beginning of the process. The critical initial displacement value inducing dewetting is lower the larger the pad is, which matches the experimental conclusions. Although it is uncertain why, this initial dewetting most likely has a detrimental effect on the self-alignment accuracy. To confirm this hypothesis, further experimental investigation would be required.

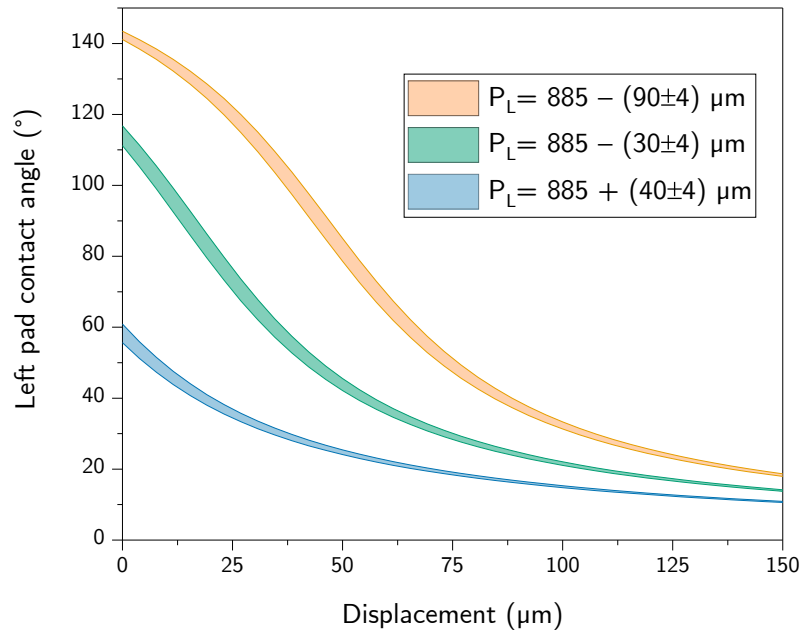


Figure 2.30: Wetting angle of the solder on the left side of the pad for different pad sizes and a solder volume of 20 nL.

2.8 Conclusion

An analytical and a numerical model of the capillary forces responsible for the self-alignment process were built and showed good accordance for cell displacements smaller than 50 μm . As the displacement gets larger, a drift is observed but the relative discrepancy does not exceed 10%.

An initial cell placement offset of 100 μm gave a higher accuracy. This was explained by the capillary forces being initially higher than without offset, inducing the self-alignment motion with more ease.

A high solder volume proved to have a detrimental effect on the self-alignment accuracy, because it decreases the capillary forces.

The T6 paste gave better results than the T3 paste, likely because of the higher wettability of the T6 paste due to a different flux.

Concerning the pad sizes, no clear difference regarding the positioning accuracy was observed in the CEA-Liten experiments. A large difference was observed for the +50 μm pads with an in-plane rotation three times as high than for the other sizes. This indicates a high man-

ufacturing tolerance of the pad dimensions of at least $\pm 20 \mu\text{m}$. However, ISE experiments yielded a higher accuracy with pads smaller than the cells, linked to the initial displacement. The most likely explanation is partial wettability of the pad when the cell is highly displaced. Nonetheless, further experimental investigation would be required to validate this hypothesis. Through the experiments and the simulations, it was demonstrated that a good pad wettability is not necessary as long as the cell wettability is good enough to ensure solder spread. In practice, a cell wetting angle of 30° is enough.

To conclude, a reliable and precise cell assembly technique has been studied in this chapter. The self-alignment experiments proved that a high positioning accuracy of $\pm 30 \mu\text{m}$ can be reached, with an initial $100 \mu\text{m}$ tolerance on the cell placement, a low solder volume of 23 nL and the T6 paste. This way, a method to manufacture the concentrator front glass has been defined. The following chapter deals with the thermomechanical aspects of the design structure.

3 Structural deflection and its impact on optical performances

3.1 Introduction

In the previous chapter, a way to assemble and align the cells on the front glass substrate was studied. The next step is to focus on its structure. Indeed, space conditions are harsh and the concentrator could suffer damage for multiple reasons, including take-off and panel deployment. Furthermore, its asymmetric and heterogeneous nature means that the space temperature cycles will make the structure bend. It could cause component failure and will certainly have an influence on its optical performances. Finally, mass and volume are major concerns and should be kept as low as possible. In this chapter, the thermomechanical behaviour of the micro-concentrator structure is studied. The end goal is to choose the right geometry to ensure reliability, performance and minimal mass. First, the bending stiffness of the structure is studied by the means of experiments and simulations. Second, the temperature-induced deflection of the structure is studied with the same tools. As a result, both studies give insights and guidelines on how to choose the right structure geometry. Finally, those guidelines are compared between each other and to space constraints to define the structure and to determine what dimensions are acceptable.

3.2 Determination of the bending stiffness of the concentrator

3.2.1 Introduction

As discussed earlier, space solar panels have to face many challenges from the space craft take-off to their end of life. High mechanical stress is expected from take-off and deployment, which is especially critical in the case of this micro-concentrator design. Indeed, it includes a large glass plate on its top side. It holds the cells, meaning that its failure would lead to high PCE losses. Besides, because of temperature variations, the structure is expected to vibrate, inducing stress and modifying the incident angle of the light. For a concentrator, it implies optical losses. A way to decrease the expected stress and vibrations is to make the panel stiff. However, it is not possible to change the materials of the structure: they should be space-grade. The only possibility is to change the geometry of the concentrator, *i.e.* the thickness of the different layers it is made up of. Nonetheless, increasing the quantity of any materials implies a mass increase as well. Therefore, it is important to understand the influence of the geometry on the stiffness of the concentrator to reach an acceptable value while minimising

its mass and the mechanical stress in the glass layer.

To reach this scientific goal, the first study consist in determining the appropriate structure geometry to reach the bending stiffness target while minimising its mass. Unfortunately, no stiffness specification was available. Instead, a target of $5 \times 10^3 N.m^2$ was defined by compiling the data available in various studies [101, 102, 103]. The second goal is to build a model that represents the behaviour of the structure under a 4-point load to be able to test multiple geometries without having to manufacture more samples. Ideally, the model should be as simple as possible to reduce computation time and make it easy to handle, that's why different approaches will be tested. Lastly, having reached the stiffness target, one can get a feel for the curvature expected in-flight and its influence on the performances of the concentrator, depending on its size. Not knowing what load the panel will experience in flight, a stress target for the glass cannot be defined. However, it is still possible to look for a way to decrease it, even if its absolute value will remain uncertain.

A scheme of the structure is displayed in Fig. 3.1. Three geometry parameters were studied: the glass thickness (t_g), the bottom honeycomb (thickness H) and the thickness of the CFRP layers (t_{ft} and t_{fb}). Those last two parameters will be considered equal and noted t_f . The cell size c and thickness t_h of the bottom honeycomb were included in the honeycom type. The thickness of the top honeycomb was not considered as it would change the optical design of the concentrator.

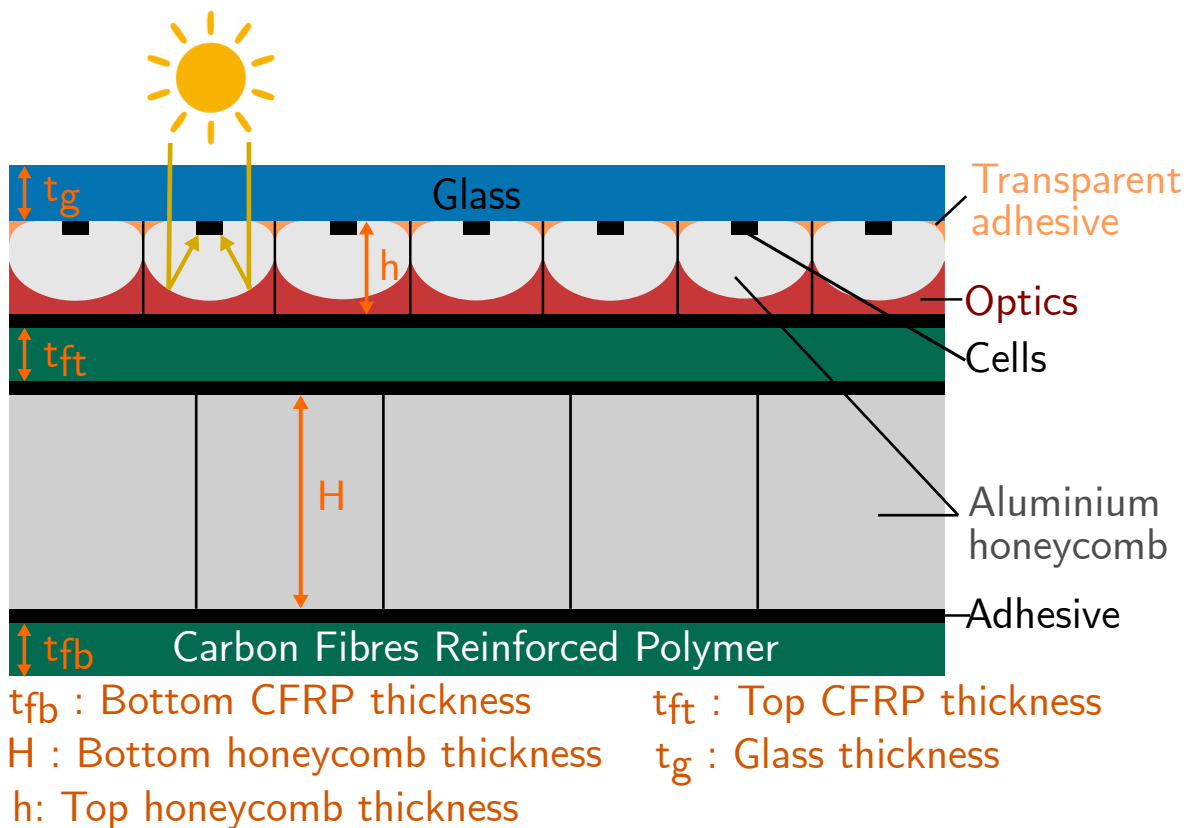


Figure 3.1: Scheme of the concentrator structure and geometry parameters.

3.2.2 Method

3.2.2.1 Sandwich theory

A scheme of a simple sandwich under a 4-point bending load is shown in Fig. 3.2. Such a structure is composed of a core and two faces bonded on its top and bottom sides. In this case, the two faces are identical and the structure is symmetric. The core provides shear and compressive stiffness and strength. The faces provide bending stiffness. This loading case corresponds to a quarter-point configuration as described in [104]. Assuming beam theory can be used, the bending stiffness D of a symmetric sandwich beam is given by Eq. (3.1) [105].

$$D = \frac{E_f b t_f d^2}{2} + \frac{E_f b t_f^3}{6} + \frac{E_c b c^3}{12} \quad (3.1)$$

E_f, E_c are the elasticity modulus of the faces and the core respectively, b is the width of the beam, t_f, c are the faces and core thickness respectively and d is the distance between the centroid axis of the faces; $d = c + t_f$. h is the total height of the structure.

The first term corresponds to the bending stiffness of the faces around the sandwich centroid axis, the second one is the stiffness of the faces around their own centroid axis and the third one is the stiffness of the core around the sandwich centroid axis. If the second term can be neglected, the faces are considered thin. If the third term can be neglected, the core is considered weak. In the case of typical space sandwich panels, both hypotheses are verified. The bending stiffness of a symmetric sandwich with thin faces and a weak core under a 4-point bending load can be determined with Eq. (3.2).

$$w_{4m} = \frac{11FL^3}{768D} + \frac{FL}{8AG} \quad (3.2)$$

The term w_{4m} is the maximum deflection of the beam, F is the load, L is the support span, G is the shear modulus of the core and $A = bd^2/c$. The quantity AG is the shear stiffness of the sandwich.

Similarly, for a 3-point loading case:

$$w_{3m} = \frac{FL^3}{48D} + \frac{FL}{4AG} \quad (3.3)$$

In both equations, the first term of the right member is the deflection due to the bending of the structure and scales with L^3 . The second term is the deflection due to the shear deformation of the core and scales with L . Thus, for long beams, the shear deformation of the core can be neglected. For shorter ones, it may play a significant role, especially if the shear stiffness is low [106]. The experimental bending stiffness will then be underestimated. For obvious practical reasons, bending tests are performed on rather short beams. Besides, in the case of this concentrator, the structure is asymmetric and there are two separate cores. Determining the shear stiffness of the structure and the contribution of the shear deformation of the cores to the deflection is not straightforward. To minimise this contribution, it appears best to use a 4-point load instead of a 3-point one. Moreover, the NF-T54 norm gives guidelines about the test samples geometry and the support span to minimise this issue further. For

those reasons, the shear deformation of the cores will be neglected and the experimental bending stiffness determined with Eq. (3.4).

$$D = \frac{11FL^3}{768w_{4m}} \quad (3.4)$$

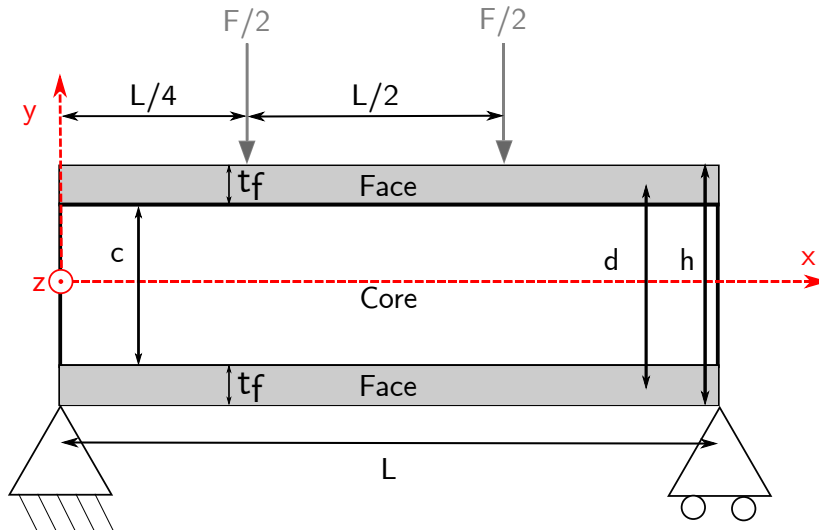


Figure 3.2: Scheme of a simple sandwich structure under a 4-point bending load. The load is represented with grey arrows, the geometry parameters with black ones.

3.2.2.2 Determination of the stiffness of a stabilised aluminium honeycomb with finite element method

Honeycombs are orthotropic structures with a complex geometry that cannot be properly represented in a 2D space. Besides, they are manufactured by laminating sheets, resulting in some walls having double the thickness of the others. As a consequence, modelling the full honeycomb is time consuming and makes the calculation time significantly higher than for a 2D material. Instead, an equivalent orthotropic material can be used. Such a material should be the same thickness of the honeycomb with the same mechanical properties, in this case the elasticity and the shear moduli. Different approaches to model an equivalent material have been proposed but do not always take the double walls into account [107]. Furthermore, the mechanical behaviour of a honeycomb structure significantly changes when it is stabilised in a sandwich structure, *i.e.* when the facesheets restrain the movement of the honeycomb walls. In this work, the following approach is used. First, a 3D model of a sandwich structure under a 3-point bending load with a fully modelled honeycomb was made. Second, another similar sandwich was modelled, but with a core having a negligible elasticity modulus. Third, the bending stiffness of both structures was determined, taking the shear strain of the core into account with Eq. (3.3). Using Eq. (3.1), the difference between them gives the contribution of the core, from which the equivalent elasticity modulus of the honeycomb can be extracted. Finally, a FEM and analytical model of a sandwich with the equivalent honeycomb core defined previously was built as verification. A 3-point load was chosen over a 4-point one

because it is easier to model and the shear deformation will be more significant, which we want to represent properly. The deflection curves for the sandwich with a fully modelled honeycomb and the two sandwiches with equivalent cores are shown in Fig. 3.3. This method was applied to the two honeycombs used in the experiments, hence the two different graphs. For both honeycomb types, high correlation is obtained between the three curves with a Spearman correlation greater than 0.997. The equivalent honeycomb properties will be used in the following section and are listed in Table 3.1.

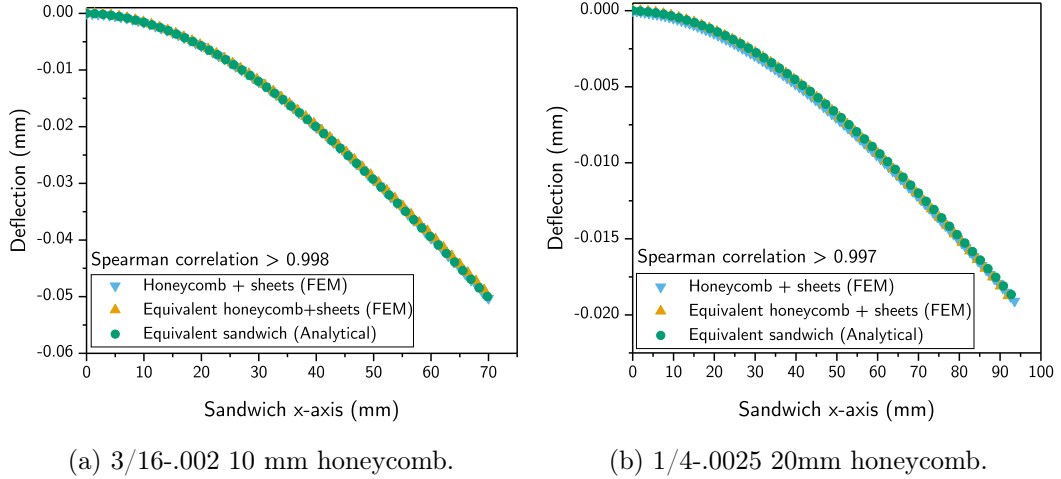


Figure 3.3: Deflection curves for the analytical equivalent sandwich model, the equivalent honeycomb and sheet FEM model and the whole honeycomb and sheet FEM model.

3.2.2.3 Simulation of 4-point bending tests

Ideally, the bending tests simulations should be as simple as possible and it seems better to use an analytical model over a FEM one. Not only does the model building and calculation time will be lower, but it also gives more insight about the behaviour of the structure. However, the risk is that it is too simplistic. In particular, the real loading case may be more complex than expected. To develop a simple yet sufficient model, three different models were developed. First, an analytical one, then one FEM model excluding the friction between the samples and the fixtures and finally another FEM model taking that friction into account. Some common assumptions were made in all three models. The optical array was not taken into account as it is manufactured by moulding Dow Corning 93-500, a silicone rubber. At -90°C , its storage modulus is equal to around 16 MPa [108]. As the glass transition is close to this temperature, the storage modulus will be considered equal to 50 MPa in the following calculation. As shown in Table 3.1, the top honeycomb has an elasticity modulus of more than 300 MPa. Considering each component on its own and the optics as a flat and homogeneous silicone layer, the ratio r of the stiffness of the top honeycomb over the stiffness of the optics is given by:

$$r = \frac{E_{ct}c_t^3}{E_s c_s^3} \quad (3.5)$$

With E_{ct} and E_s the elasticity modulus of the top honeycomb and silicone respectively and c_t and c_s their respective thicknesses. Assuming the silicone optics fill half the thickness of the honeycomb cell, $r = 48$. Therefore, the contribution of the optics to the stiffness of the structure can be neglected. The adhesives are both epoxy-based and their elasticity modulus is expected to be around a few GPa. They are about the same thickness as the CFRP layers or thinner, meaning that their contribution to the bending stiffness is expected to be about 15 times lower compared to the CFRP sheets (see Table 3.1). Therefore, they will also be neglected. The concentrator can then be considered an asymmetric structure made up of five layers with three different materials. This is beyond the scope of the basic theory presented before, so the equations have to be adapted.

Extended analytical model for asymmetric sandwiches

Focusing first in the analytical model, a scheme of the structure is shown in Fig. 3.4. The variable p is arbitrarily defined as the distance between the neutral fibre and the bottom of the sandwich. t_g and t_f are the thickness of the glass and CFRP sheets respectively, c_t and c_b are the thickness of the top and bottom honeycomb respectively. The bending stiffness of the sandwich is equal to the sum of the second moment of area of the different components around the overall neutral fibre of the structure, multiplied by their respective elasticity modulus.

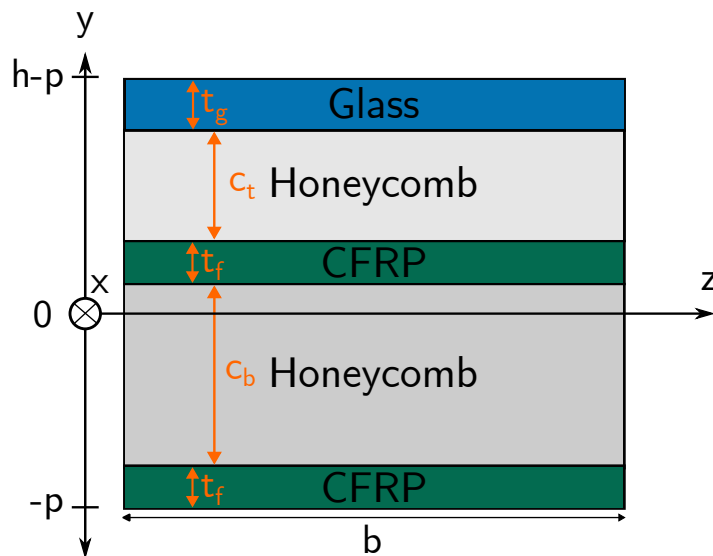


Figure 3.4: Scheme of the section of the structure.

In this case, with bending around the y axis:

$$D = b \sum_i E_i \int y_i^2 dy \quad (3.6)$$

As an example, the second moment of area of the bottom carbon sheet I_b is given by:

$$I_b = b \int_{-p}^{-p+t_f} y^2 dy \quad (3.7)$$

Equation (3.6) gives the bending stiffness as a function of p . The actual bending stiffness is the minimum of this function as it corresponds to the minimum energy storage. In this work, the value of p and D was determined through a simple numerical method.

The mechanical stress in a layer i is given by:

$$\sigma_i(x, y) = \frac{M_f(x) \times y}{D} \times E_i \quad (3.8)$$

M_f is the bending moment. For of 4-point quarter point loading, M_f and therefore the stress are maximum and constant between the two central loading points. M_f is equal to $FL/8$. One can then determine the maximum stress σ_{im} in a layer i (Eq. (3.9)).

$$\sigma_{im}(y) = \frac{FL \times y}{8D} \times E_i \quad (3.9)$$

Simply put, the stress increases with the distance to the neutral fibre and the elasticity modulus of the layer.

Finite element models of 4-point bending tests

Two slightly more complex models based on finite element method were also built. To reduce computation time and resources, the tests were modelled in 2D and plane stress state was assumed as samples are beams. For wider samples, like a whole module, plain strain elements would be more appropriate. Moreover, only half the beam was modelled as the problem is symmetrical. A structured mesh with second order quadrangles elements was used as they are adapted to the rectangular geometry of the problem. The materials properties are presented in Table 3.1.

Material	E_x (MPa)	E_y (MPa)	G_{xy} (MPa)	G_{yz} (MPa)	ν
Carbon fibres	75,000	75,000	/	/	0
Glass	73,400	73,400	/	/	0
3/16 - .0007 honeycomb	342	234	186	99	0
3/16 - .002 honeycomb	890	1517	621	265	0
1/4 - .0025 honeycomb	685	1310	565	244	0

Table 3.1: Material properties used in the simulations.

Since the Poisson's coefficient was unknown for all materials except the glass, two values were tested. It was first set to 0.3, which is rather realistic for the materials considered and then to 0, for all materials at the same time. A stiffness difference of 0.1% and a maximum stress difference of 0.6% was observed. Since it has no significant influence, the Poisson's coefficients were left to 0 even if it is unusual.

In the first FEM model, the friction between the test fixture and the sample was assumed negligible. The mesh was made so that all elements have the same dimension along the x -axis.

So, the distributed load was modelled using concentrated loads, uniformly distributed over the support and loading areas, as in Fig. 3.5(a). The bending stiffness for each configuration was determined using Eq. (3.2), assuming the shear deformation can be neglected.

In the second finite element model, the friction was taken into account. This time, no load was applied. Instead, two rigid moving bodies were used to simulate the fixture support and loading areas (see Fig. 3.5(b)). The distance between the loading areas and their axis of rotation is representative of the experimental tool. The red arrow represents the imposed displacement of one of the rigid bodies. In the case of the upper rigid body, its displacement was fixed to 0. In the case of the lower rigid body, the displacement along the y -axis was imposed (1 mm) but the displacement along the x -axis was fixed to 0. In both cases, the rotation around the z -axis was free. A contact law was defined by the friction coefficient determined experimentally (see Table 3.2 for values). An experimental set-up inspired by the ASTM D1894 standards [109] was used. The sample was maintained on a flat surface and the upper part of the test fixture was placed on top of the sample. The fixture was then dragged along the sample with a wire connected to the INSTRON machine described earlier. The fixture was previously weighed with the machine. This way, the traction force was measured, tangent to the sample surface, for the narrow and wide samples. The static friction coefficient corresponds to the ratio of the maximum recorded traction force over the weight of the test fixture. Five tests were made for each type of contact.

Sample size	Contact	Friction coefficient
Narrow	Rubber/CFRP	0.95
	Rubber/glass	1
Wide	Rubber/CFRP	0.19
	Rubber/glass	0.2

Table 3.2: Friction coefficients used in the FEM model with friction.

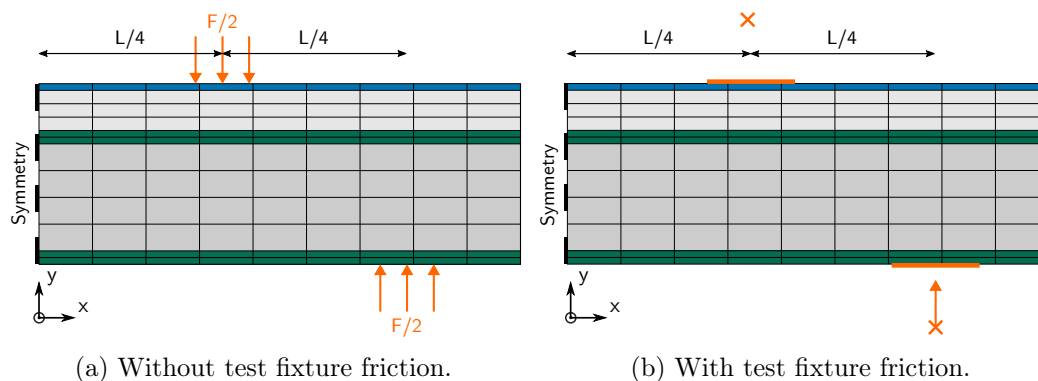


Figure 3.5: Scheme of the two FEM models. Red lines represent the loading areas in contact with the sample. Red crosses represent the centre of rotation of the loading areas.

3.2.3 Experiments

Manufacturing the samples and testing them is time-consuming. Besides, the materials are expensive. Instead of testing all the twelve configurations, we decided to use the statistical analysis software JMP [110] to design the experiments. Only six configurations were tested, chosen by the software. They are presented in Fig. 3.6. This small number of experiments is enough to obtain the influence of the input parameters. The number of plies was chosen to obtain a CFRP thickness close to standard panels, between 0.2 and 0.4 mm. As mentioned earlier, the top honeycomb was fixed to avoid changing the optical design at this stage. The glass was chosen relatively thick to make the experiments easier to conduct. Besides, since it will act as a mechanical support, it should most likely be thicker than the space standard of 100 μm . The three thicknesses are also standard for thin glass manufacturers. Finally, a 20 mm thick honeycomb is standard for space applications. A 10 mm one was also tested to see if the volume of the concentrator could be reduced significantly.

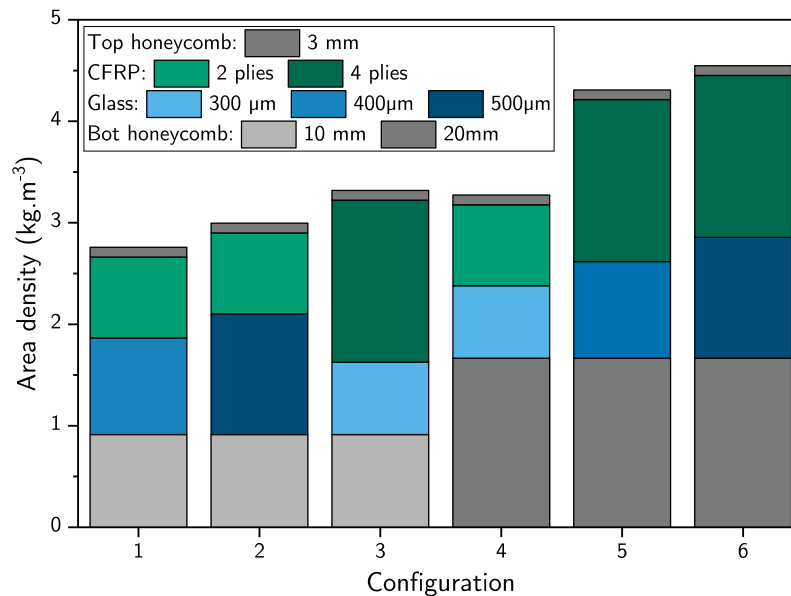


Figure 3.6: Summary of the 6 configurations to be manufactured and tested and their respective area density.

3.2.3.1 Samples preparation

The mechanical properties of the three kinds of aluminium honeycombs used in this study are listed in Table 3.1. They are all HexWeb[®] CR III 5052 Al alloy corrosion treated from the Hexcel company. Bottom honeycombs with rather thick walls were chosen as they have higher shear modulus. This helps decreasing the shear deformation of the honeycombs during the tests, which would lead to an underestimation of the bending stiffness as explained earlier. This choice does make the area density of the honeycombs higher than for a standard rigid panel. A thin-walled top honeycomb was chosen, as it would cover less surface on the cover glass and thus reduce shading.

The samples were made using TeXtreme[®] 86 PW HS40 WD/20:4320:43-1000 carbon fibres. Their elasticity modulus were characterised using a 3365 INSTRON[®] machine. The results are presented in Table 3.1.

Space-grade cover glass such as Qioptiq CMG are expensive and few sizes are available. In the context of this study, large glasses were needed and so a boro-aluminosilicate display glass, Corning EagleXG[®] slim, was used. Nonetheless, their elasticity modulus and Poisson's ratio are similar.

To bond the glass to the honeycomb without absorbing light, a clear epoxy-amine system was chosen, the Loctite[®] Ablestik 45 CLEAR and the catalyst Loctite[®] CAT 15 CLT, both manufactured by Henkel. While a space-grade encapsulant like Dow Corning DC 93-500 would induce less optical losses, the goal of this study is to assess the mechanical properties of the structure. An epoxy adhesive provides a stronger bond at a lower cost and does not require the use of adhesion primer and the associated chemical hazards.

The CFRP sheets were bonded on the honeycombs using HexBond[™] 312L from Hexcel.

According to the NF T54-606 norm guidelines [104], the width and length of a test sample must be chosen accordingly to its thickness. Following the norm, samples from configurations 1, 2, 3 were manufactured to 340x50 mm and samples from configurations 4, 5, 6 to 420x80 mm.

The CFRP and honeycomb assembly were first laminated at 150°C under a pressure of 1 atm. Then, the glass was bonded on the upper honeycomb with the curing epoxy at room temperature for at least 24h. During the cure, the sample is placed upside down (glass on the downside) to prevent the epoxy from getting into the honeycomb cells. The epoxy is manually spread over the glass surface, so its thickness is not controlled.

For each configuration, five samples were manufactured and tested to ensure reproductability. Figure 3.7 shows the side view of a test sample (configuration 6).

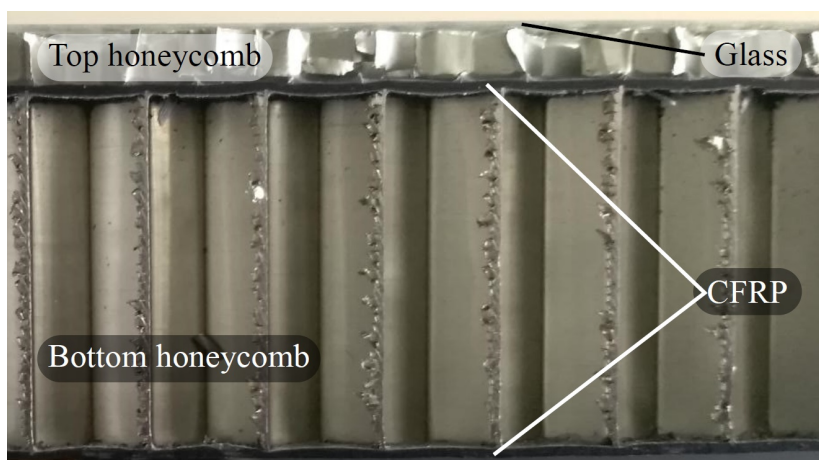


Figure 3.7: Picture of the side of a sample. Configuration 6.

3.2.3.2 Set-up and test procedure

The tests were performed on a INSTRON 3365 system. The force was recorded with a 5 kN load cell with a sensitivity inferior to 1 N. Tests were carried out at a fix displacement rate of 2 mm/min to stay in the range of a quasi-static problem. The 4-point bending test fixture included four flat and rectangular loading areas. The loading areas were mounted on cylinders to be able to rotate freely. This is done so that they follow the curve of the samples as they bend. This fixture is compliant with ASTM D7250 and D7249 standards [111, 112]. To record the deflection of the samples during the tests, a SVE2 video extensometre was used. As the test support span was large enough (compliant with ISO standards) and the honeycomb chosen for their high shear stiffness, the shear deformation of the honeycomb was considered negligible and the bending stiffness was determined with Eq. (3.2). A picture of the test set-up with a sample can be found in Fig. 3.8. The red light is due to the extensometre.

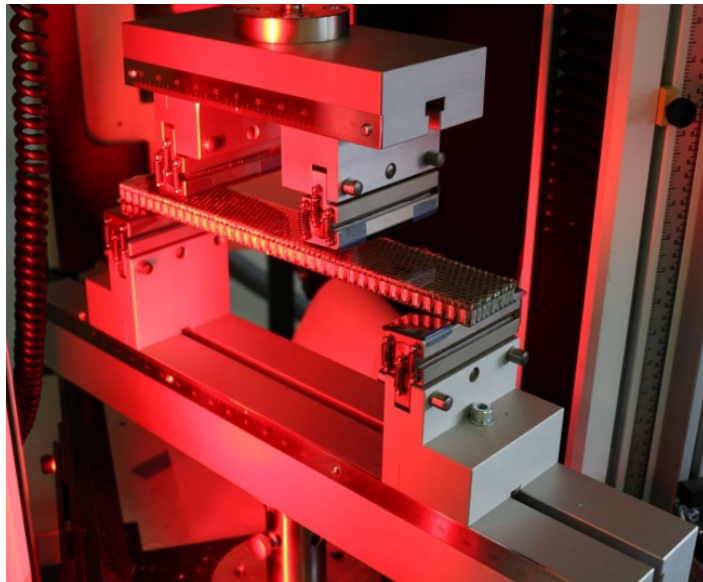


Figure 3.8: Picture of the 4-point bending fixture used with a sample ready to be tested.

Because of the test fixture, the friction forces were different depending on the samples geometry. A scheme of the samples on the fixture is shown in Fig. 3.9.

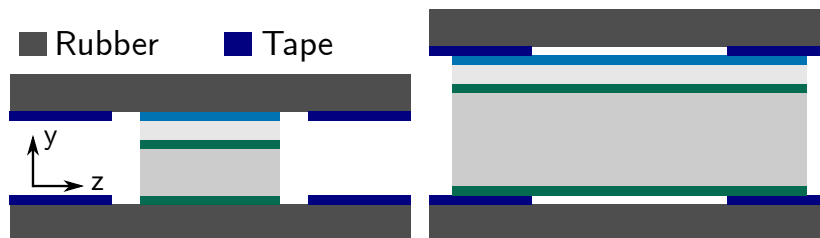


Figure 3.9: Scheme of the contact between the test fixture and the narrow (left) and wide (right) samples.

For the narrow samples (1, 2, 3), their surface was in contact with the rubber bands on the loading areas, resulting in a very high friction coefficient. The wide samples (4, 5, 6) were

large enough so that their surfaces was in contact with the tape used to maintain the rubber bands, which has a lower friction coefficient.

3.2.4 Results and discussion

3.2.4.1 Comparison of the experiments and models

Figure 3.10 shows the bending stiffness obtained from the experiments, the analytical model, the FEM model without friction and finally the FEM model with friction for the 6 configurations tested. First, the stiffness from the experiments is higher than the one from the analytical and FEM without friction models. The relative discrepancy is higher for the 1, 2 and 3 configurations and lower for the three others, reaching up to 34%. Furthermore, the experiments and FEM model with friction exhibit good agreement, with no more than 5% relative discrepancy. Those differences can be explained by the friction forces between the loading areas of the test fixture and the samples results in a higher measured load. Thus, the experimental bending stiffness is largely overestimated from the friction caused by the test fixture. In the future, bending tests should be performed without the rubbers pads and with proper lubrication to reduce the friction as much as possible.

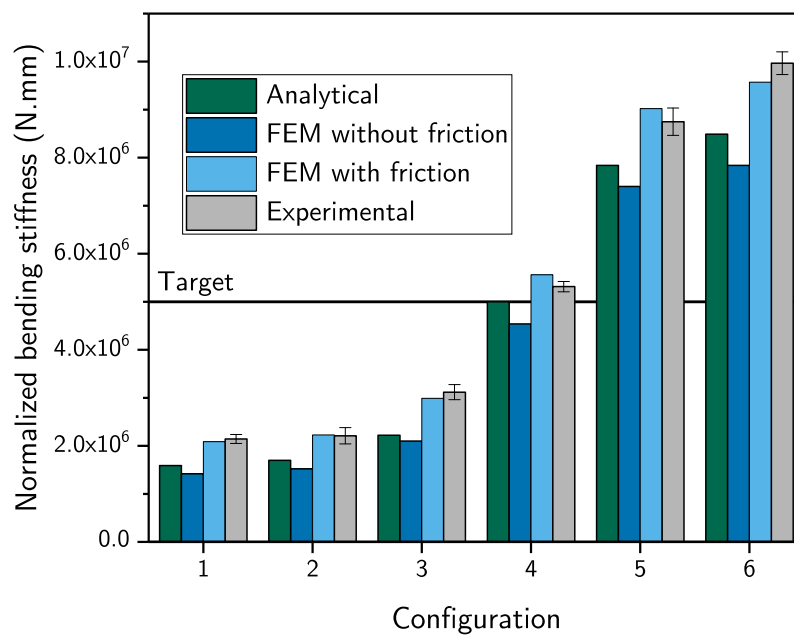


Figure 3.10: Normalised bending stiffness of the different configurations from the experiments, the analytical and the two FEM models.

Notwithstanding, the relative discrepancy between the FEM model without friction and the analytical model did not exceed 11%. First, this shows that both models are valid and describe the bending tests well. Second, a simple analytical model is enough to determine the bending stiffness of 5-layered sandwich structures. The use of FEM may add accuracy but a clear conclusion cannot be drawn from the experiments because of the friction issue.

Lastly, focusing on the model giving the lowest bending stiffness, the target of $5 \times 10^6 N.mm$

was reached for configurations 5 and 6 with certainty. The next step is to look at the stress distribution in the structure to know how the stiffness/weight ratio of the structure can be decreased.

The maximum stress in the CFRP and glass layers from the analytical and FEM without friction mode for the six configurations are shown in Fig. 3.11. As a rule of thumb, an ideal structure should exhibit low glass stress and a balanced stress distribution between the two CFRP layers. The stress in the honeycomb is not represented as it is negligible compared to the other layers. Indeed, the elasticity moduli of the honeycomb do not exceed 2 GPa. Thus, for a layer at the same distance from the neutral fibre, the honeycomb stress would be about 35 times lower than in the glass or CFRP. An arbitrary bending load of 200 N was applied in both models, so the absolute stress values have no practical meaning.

Comparing the two models, agreement is found with no more than 11% discrepancy. The difference comes directly from the stiffness difference between the model (see Eq. (3.8)). Once again, the simple analytical model is enough to get an idea of the stress distribution in the structure.

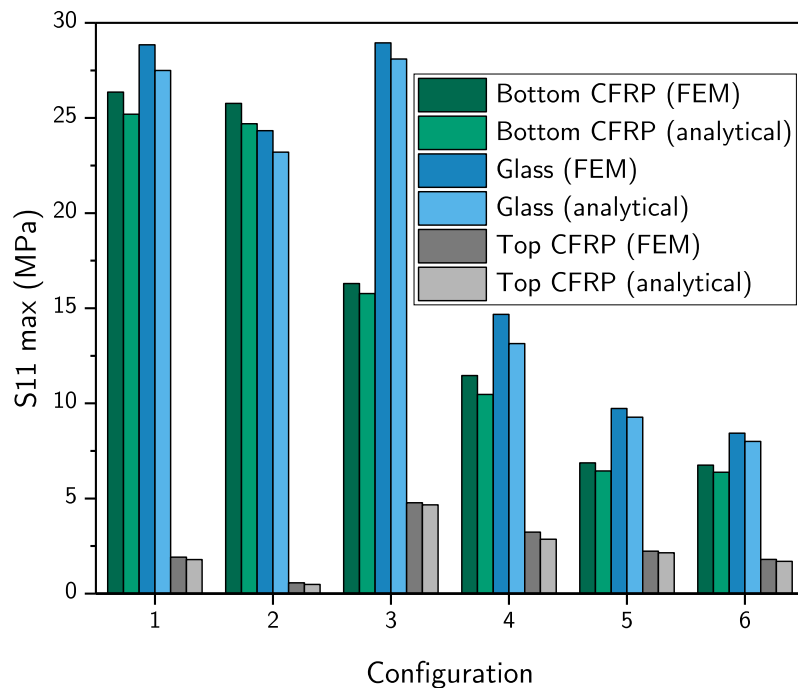


Figure 3.11: Maximum longitudinal stress in the main layers for the analytical and FEM model without friction.

All configurations are far from the ideal structure describe above. The stress is lower in the glass than in the CFRP layers for configuration 2 only, which did not reach the stiffness target. For configuration 3, the stress in the glass is almost twice as high as in the bottom CFRP. Overall, the stress in the top CFRP is much lower than in the other layers. It does not exceed half of the stress in the top CFRP layer, results obtained in configuration 5. From

these results, it appears that the top CFRP layer has little to no contribution to the bending stiffness of the structure. This is especially true when it is thick compared to the other layers, as predicted by Eq. (3.9). It then seems interesting to dissociate the thickness of the two CFRP layers.

3.2.4.2 Choice of the most interesting configurations

From the previous results, the following guidelines for the concentrator geometry can be established:

- The bottom honeycomb should be thick.
- The bottom CFRP and glass layer should be thick.
- The top CFRP layer should be thin.

Overall, the measured area density of the configurations may seem high for space PVA. One should bear in mind that the CFRP used are not high elasticity modulus space grade, but rather high strength. The standard elasticity modulus of space-grade CFRP would be about twice as high, decreasing the CFRP thickness and mass needed to reach the stiffness target by two.

Another point to bear in mind is that relatively thick-walled honeycombs were chosen for their ease of manipulation. Those honeycombs are quite heavy and are responsible for about a third of the total mass of the configurations 5 and 6. Keeping the importance of core shear stiffness, lighter honeycombs with thinner walls should be used.

Lastly, the epoxy adhesive layer used to bond the glass appeared to be quite thick from a visual inspection. For later bonds, its thickness could be decreased, further reducing the area density of the structure.

3.3 Thermally induced deflection of the micro-concentrator array

The structure of the concentrator is asymmetric, whether considering its geometry or the materials used to manufacture it. The main feature is a rather thick glass plate (400 μm) on one side and a CFRP layer on the opposite side. Besides, there is another CFRP layer placed between two aluminium honeycomb of different thicknesses. Not even considering the adhesives, the three materials mentioned have different Coefficients of Thermal Expansion (CTE) and thus will have a different behaviour with temperature changes. This means that the curvature of the solar panel will change with the temperature, modifying the incident angle of the light and inducing mechanical stress as explained in the previous section. In Earth orbits, high temperature amplitudes are expected and the panel curvature may have a significant influence of the electrical performances of the concentrator. Once again, the materials themselves cannot be changed and the curvature can only be controlled by modifying the geometry of the concentrator or its thermal design. In this section, we will keep building on

the bending stiffness study and focus on the geometry only. This includes both the thickness of the different layers and the length of the panel.

3.3.1 Determination of the acceptance angle of the concentrator

The system was modelled using a ray tracing software, TracePro [®], that does not take into account the honeycomb shape of the mechanical support. Thus, the AM0 solar flux (1366 W/m²) passes through a 500 μm thick N-BK7 coverglass. A circular solar cell with a diameter of 900 μm is located on the downside of the glass. To estimate the incident solar flux on the surface of the cell, the cell is considered as a perfect absorber. The mirror is a parabola, with a focal length of 2.25 mm and a diameter of 4.6 mm (geometric concentration of 26X), coated with a silver reflective layer that focuses the luminous flux onto the cell surface. The acceptance angle as a function of the alignment error along the optical axis of $\pm 500 \mu\text{m}$ gives a minimum AA of 4.2°.

3.3.2 Design of experiments

From the bending stiffness study, it appears that the two CFRP layers should be considered independently. So, this time, five variables were taken into consideration and are shown in Fig. 3.1. A set of variables corresponds to a specific geometry that will be called configuration. The first approach to test their influence would be to manufacture samples with different configurations and measure their experimental curvature as a function of the temperature. As for the bending tests, test samples manufacturing is quite expensive and the length of the samples is limited by the experimental set-up available. Space-grade materials are still not available. Besides, high temperature amplitudes are necessary to be able to properly measure the curvature of rather small samples. This makes experiments extremely time-consuming, especially since having five variables implies a high number of experiments.

For those reasons, the idea is now to develop a model which parameters are easy and quick to modify. The model will be build on experiments with test samples manufactured with the same materials described before. Only one structure configuration will be used in the experiments, chosen to maximise the curvature, making the measurements more precise and reliable.

Then, the model will be adapted to space-grade materials and used to determine the temperature dependent curvature of multiple structure configurations. Simple geometries and temperature conditions will be used. Although not representative of actual space conditions, the will be pave the way for more realistic models. Since simulations are expected to have a low computation time and can be automated, the five geometries parameters will have four different levels. This means that 1024 configurations are possible. Thanks to statistical analysis, only 40 configurations are necessary to get the influence of the parameters and approximate the curvature for any configuration. The configurations were chosen by the JMP software. A summary of the parameters and their levels are shown in Table 3.3.

Once the temperature-dependent curvature is known, it is possible to determine the maximum

incident angle of the panel for a specific orbit. Coupled with a ray-tracing model, the impact of the curvature on the optical performances can be estimated.

H (mm)	h (mm)	$t_{fb}(mm)$	$t_{ft}(mm)$	$t_g(mm)$
15	3	0.2	0.2	0.1
20	5	0.4	0.4	0.2
25	10	0.6	0.6	0.5
30	15	0.8	0.8	1

Table 3.3: Summary of the parameters and their levels.

3.3.3 Experimental curvature measurements

To measure the deflection as a function of the temperature of the structures, a specific experimental set-up had to be designed. To control the temperature, an INSTRON climatic chamber was used, which temperature can range from -70°C to more than 200°C . The samples are still visible through the chamber glass, but its dimensions limit the sample geometry, especially their length. A pair of samples was held with aluminium fixtures. Figure 3.12 shows a scheme of the experimental set-up.

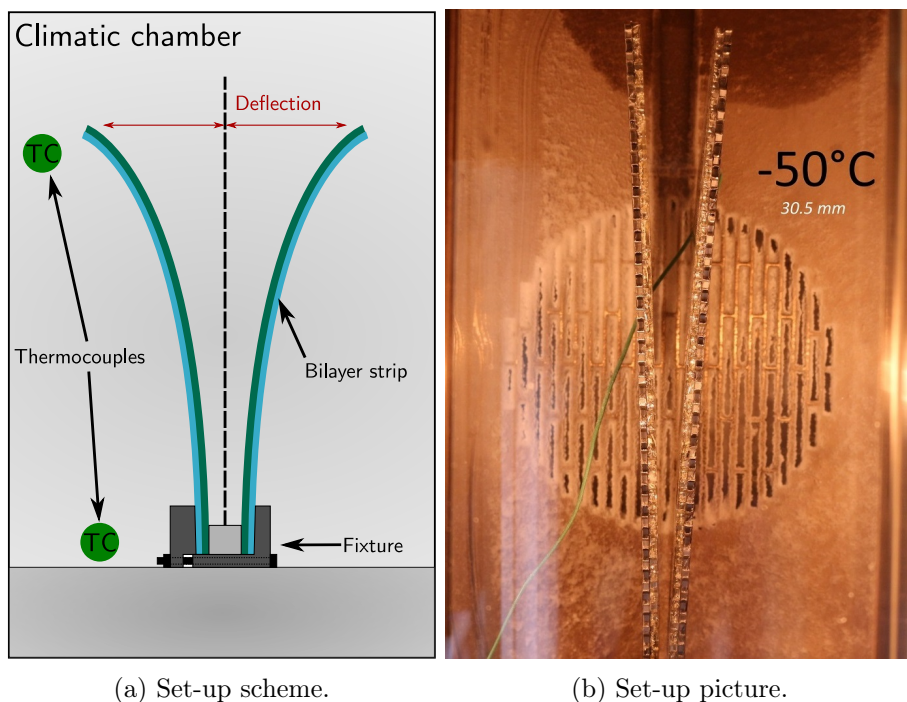


Figure 3.12: Experimental set-up used to measure the deflection as a function of the temperature.

Having two samples allows to measure a deflection that is twice as high than for a single sample, increasing the measurement precision. A polymer block was placed between the samples to be able to measure positive and negative deflection. Unfortunately, the fixtures used were not meant for this task and it was difficult to maintain the samples in place properly,

especially for large temperature differences. The consequences will be seen in the upcoming sections: some data points may be missing in the deflection curves. It also adds some measurement uncertainties that are difficult to estimate, since samples being poorly held will exhibit a higher deflection. Two thermocouples were added in the chamber to check the temperature in real time and ensure its spatial homogeneity. Finally, the deflection was measured from pictures made with a CANON EOS camera which was placed on a tripod in front of the climatic chamber.

The samples were manufactured in a rather similar way as for the bending tests. First, the CFRP and honeycomb structure was laminated. The lamination itself can be divided into two steps. The structure is heated at atmospheric pressure about 15 min and then the 1 atm pressure is applied for 20 more minutes. The heat source is a hot plate on the bottom of the laminator (see Fig. 3.13(a)), so the temperature in the structure can be assumed to be heterogeneous. Besides, the actual curing temperature of the prepreg and the adhesive is unknown.

The second and last step of the sample manufacturing process consists of bonding the glass on the upper honeycomb with a curing epoxy. This time, the curing was performed in an oven at 105°C for 30 min (see Fig. 3.13(b)). This is the highest recommended curing temperature by the manufacturer and was chosen to reduce the curing temperature difference between the other part of the structure. Furthermore, it makes sense to speed the cure up in an industrial process.

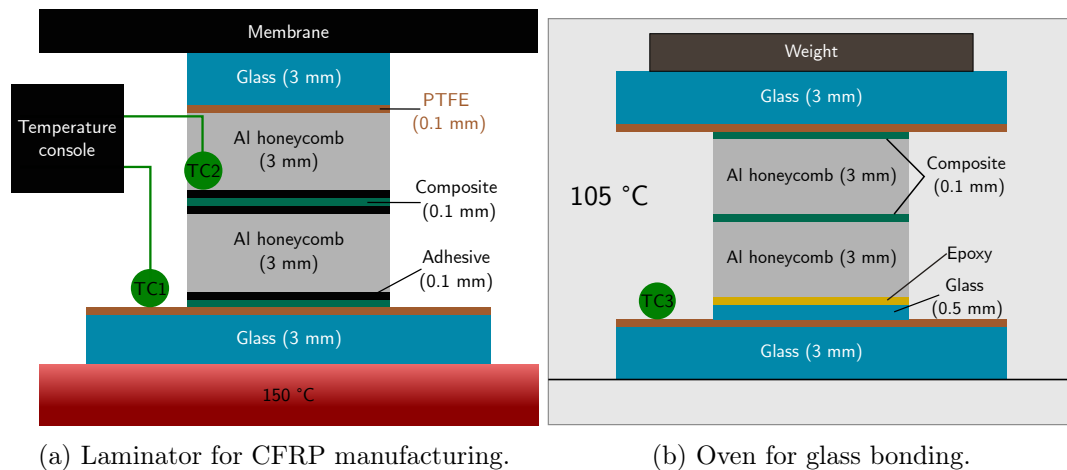


Figure 3.13: Scheme of the lamination and glass bonding steps.

3.3.4 Finite element model building

3.3.4.1 Overview of the FEM model

A 2D FEM model was build first and its results presented at the CPV-18 conference [113]. After trying to confront it with experiments, it appeared that it was too simple to properly represent the behaviour of the structure. It was then decided to build a more complex model that is presented here.

The bending of multi-layered structures is a common issue in micro-electronics. Analytical models were already developed for such applications [114, 115, 116], even for an indefinite number of layers [117]. However, considering the geometry of the samples, the adhesives cannot be considered as thin layers placed between the other layers (*e.g.* a redux layer between a honeycomb and a CFRP sheet). Instead, they tend to get inside the honeycomb cells and slightly up the walls by capillarity. Representing this geometry in 2D is not possible. Furthermore, using 2D also means using an equivalent material for the honeycombs. Although we demonstrated good results with such an approach in the first part of this chapter, it is unsure how well it could be applied in this case. To avoid additional uncertainties on the honeycomb mechanical properties, it appears best to use a complete 3D mesh. With this in mind, it makes sense to use FEM instead of an analytical model that cannot represent the geometry of the structure.

To this purpose, a parametric structured mesh was designed with the Gmsh software. The parameters are the honeycomb thickness, cell size and wall thickness. This approach is harder to develop than a CAD design at first but it does make changing the honeycomb type much easier once it is ready. Since forty different structures will be tested in the DOE, it seemed to be the better option this time. The mesh is structured so that all layers are coherently tied in the Abaqus model later on. It also provides faster convergence. A scheme of the mesh can be found in Fig. 3.14.

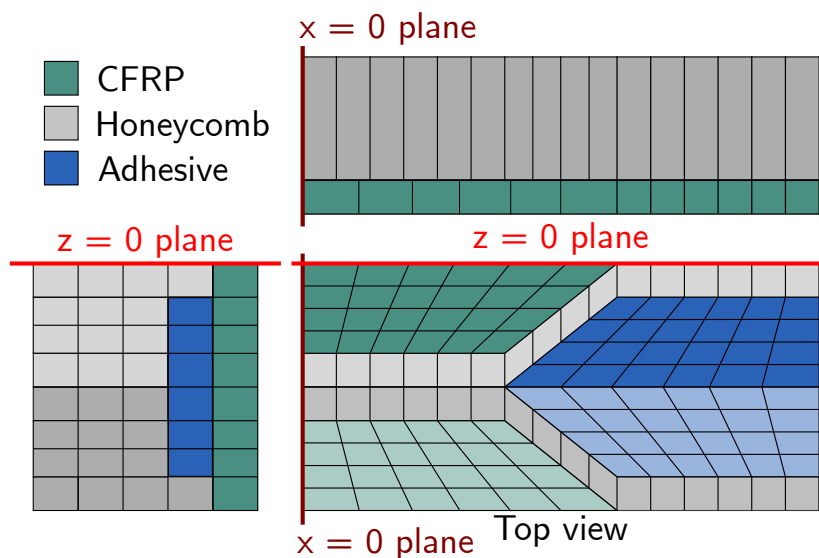


Figure 3.14: Scheme of the bottom layer of the structured mesh.

Because of the high complexity of the meshes and their high number of nodes and elements, it was not possible to use models with the large dimensions expected in experiments. As an example, building a model with only eight honeycomb cells takes more than 30 min and this time grows exponentially with the number of cells. Besides, this time does not even take the calculation time into account. So, instead of building large models, it is possible to assume that the structure curvature is quadratic. For each configuration, the deflection as a function

of the temperature can then be fitted as a quadratic function that depends on the structure size. Thus, the deflection of a configuration can be extrapolated for any length. In practice, to get a deflection curve from the FEM calculation that can be properly fitted, a minimum number of cells is needed. If too few cells are in the model, the deflection in the model will be underestimated and the extrapolated deflection will be wrong. A convergence study was performed, comparing the deflection of the same configuration for different model lengths. It appeared that 8 honeycomb cells were enough to converge without increasing the calculation time too much.

Regarding the boundary conditions, symmetry conditions were applied to the nodes in the $x = 0$ plane to represent the fixed side of the panel. Symmetry conditions were also applied to the nodes in the $z = 0$ plane to represent a second row of honeycomb cells and be closer to the actual structure without increasing the calculation time.

3.3.4.2 Materials properties

The equation of the curvature of a bimetallic strip as a function of the temperature [118] is enough to determine what material data are needed to build a more complex thermal deflection model. On top of the geometry of the structure and its individual layers, the elasticity modulus, CTE and reference temperature of the materials are required. In the case of a bimetallic strip, the reference temperature is the temperature at which both layers were bonded. In this case, it can be approximated at the curing temperature of the layers. However, it is difficult to determine when bonding occurs during curing.

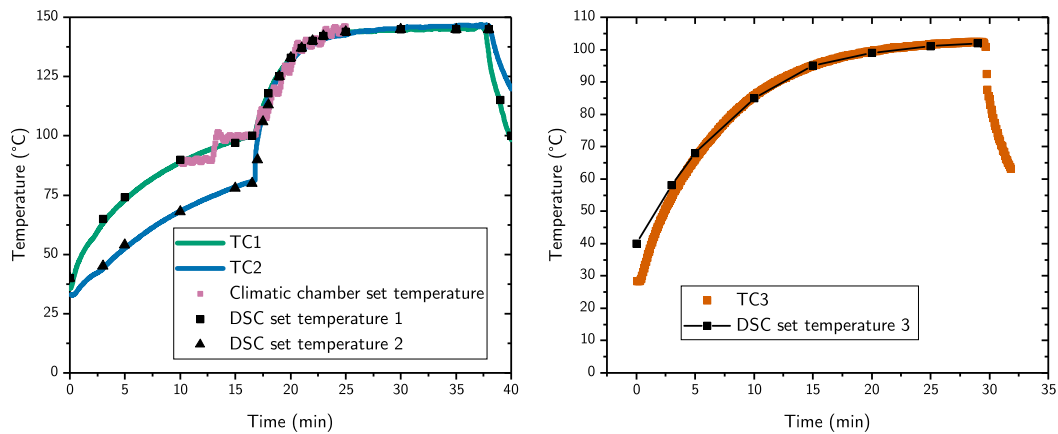
Some material data are given by manufacturers, other were obtained from previous studies. At this stage, no data about the adhesives was available and the CFRP CTE was also missing.

To determine the curing temperature of the polymers, Differential Scanning Calorimetry (DSC) measurements were performed. To closely reproduce the experimental manufacturing conditions, the temperature in the different layers of the structure was recorded during the lamination step. Then, the thermal profiles obtained were reproduced in the DSC measurements. Similarly, the temperature profile in the oven was recorded and reproduced. The temperature profiles can be found in Fig. 3.15. As shown in Fig. 3.13(a), the thermocouple 1 (TC1), respectively 2 (TC2) were placed on the bottom, respectively top CFRP layer during lamination. As expected, the top layer is significantly cooler in the first 15 min, before pressure is applied. This difference reaches about 25°C when the bottom layer is at 100°C. During this step, the contact between the different layers may not be total and the heat slowly spreads to the upper layers, resulting in a high temperature gradient. Once the pressure is applied, full contact is obtained. Even if the honeycomb walls are thin, aluminium is an excellent heat conductor and the other layers are very thin (<1 mm), so the heat spreads quickly. The temperature difference becomes negligible almost as soon as pressure is applied.

Concerning the abestik curing process, thermocouple 3 (TC3) was placed near the glass plate to be bonded. The assembly shown in Fig. 3.13(b) was put cold in the hot oven. Therefore, the temperature slowly rises from room temperature to 105°C, only reaching it towards the end of the process.

During the DSC measurements, the heat flow difference between the sample and an inert ref-

erence is recorded. If no transition or curing occurs in the test sample, this difference should be equal to 0. However, in this case, since the set temperature profile includes several steep slope changes, measurements artefacts appear and make the graphs hard to read. To solve this problem, reference curves were made with already fully cured samples of both thermal profiles. Those curves were subtracted from the measurements of the actual samples to get easily exploitable curves. Nonetheless, some minor artefacts are still visible.



(a) Temperature profiles for thermocouples 1 and 2. (b) Temperature profile for thermocouple 3.

Figure 3.15: Measured temperature profiles during manufacturing and corresponding temperature profiles for the experiments.

The DSC measurements for the CFRP epoxy and the redux 312L for both thermal cycles (TC1 and TC2) are shown in Fig. 3.16(a). First, the curves exhibit exothermic heat flow peaks corresponding to the polymer curing. Focusing on the peak amplitudes first, it appears that the same material has the same amplitude no matter its thermal cycle. The large amplitude difference between the two materials is due to their composition. The redux is an epoxy film, whereas the CFRP is a composite with only 40% of MTC 811 epoxy, so 60% of the sample does not react.

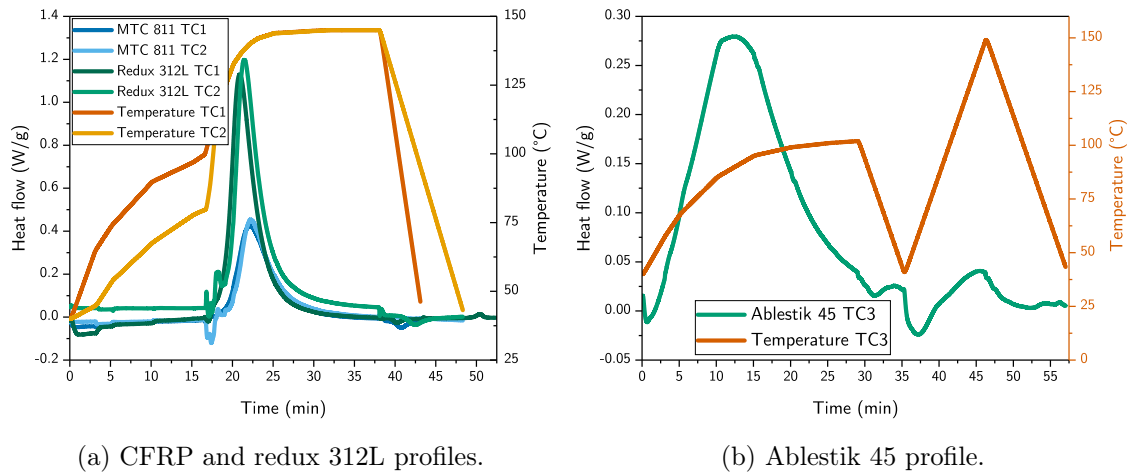


Figure 3.16: Heat flow and temperature as a function of time for the DSC measurements.

More importantly, the peak occurs at about the same time corresponding to a temperature of about 125°C. Consequently, the full structure cures at the same temperature during the lamination step and its reference temperature is around 125°C.

Focusing now on the ablestik epoxy in Fig. 3.16(b), it appears that the curing peak is wider than for the other measurements. The ablestik epoxy takes a longer time to cure. Looking at the second heating cycle (35-50 min), it seems that 30 min at 105°C are not enough to fully cure it. Nonetheless, in practice, no delamination was observed and from a qualitative inspection it appears hardened. Moreover, the peak is reached at about 90°C.

The mechanical properties (mainly elasticity modulus) of the polymer layers of the structure are expected to vary quite a lot with temperature. Indeed, terrestrial applications materials are used, which operating temperature is rather low. The tensile elasticity modulus of CFRP is determined by the carbon fibres, the temperature dependent behaviour of the matrix should not have an impact on it. However, the question is open for the redux and ablestik adhesives. This is especially critical as the degradation of the adhesive layers may cause delamination at high temperatures. Thus, Dynamical Mechanical Analysis (DMA) was performed on the adhesives to determine their storage modulus as a function of the temperature. The extracted measurements are shown in Fig. 3.17.

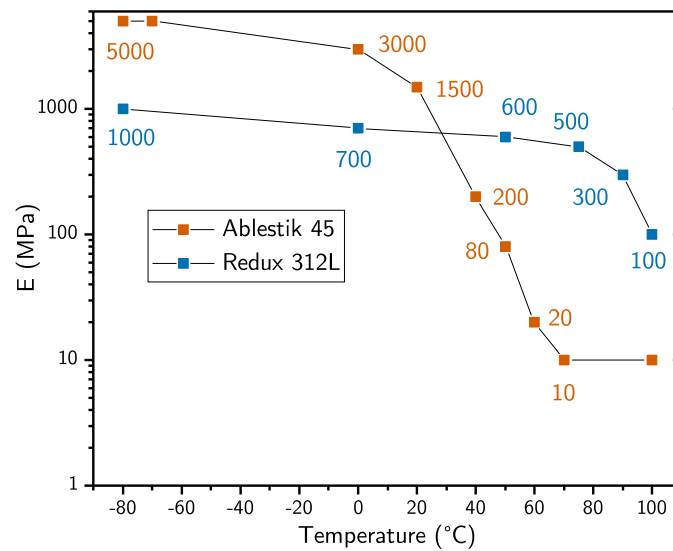


Figure 3.17: Ablestik 45 and redux 312L storage modulus measured in DMA.

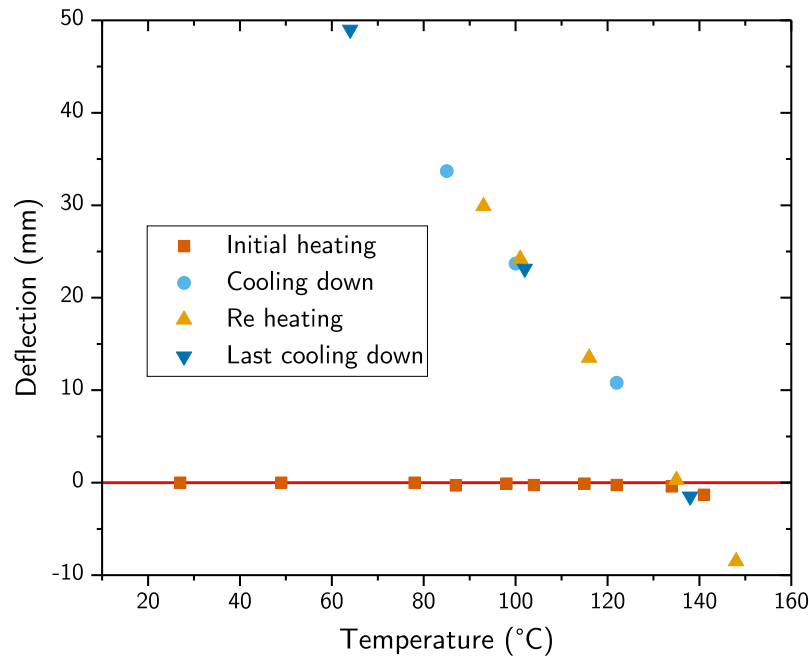
The redux curve shows a slowly decreasing storage modulus when the temperature increases. It is about 1 GPa at -80°C and 500 MPa at 70°C . As the glass transition happens around $70\text{--}80^{\circ}\text{C}$, the modulus decreases rapidly but remains above 100 MPa at 100°C . The ablestik epoxy shows a similar but more extreme behaviour. The storage modulus is larger than for the redux at low temperatures (5 GPa at -80°C). It decreases rapidly with the temperature increasing and the glass transition is observed at about 60°C . At this point, the elasticity modulus drops dramatically and is as low as 80 MPa at only 50°C . It keeps decreasing and gets too low to be measured at 70°C . In the simulations, the storage modulus will be considered equivalent to the elasticity modulus of the corresponding material, neglecting its viscoelastic behaviour.

First, the experimental deflection of CFRP-glass bilaminates was measured. This has two purposes: verifying that the CFRP curing temperature determined in DSC is the right one and measuring the CFRP CTE. The corresponding curve is shown in Fig. 3.18(b). To be able to see precisely when the two layers become bonded, curing was performed inside the climatic chamber used for measurements. To verify that high temperatures do not degrade or deform the bilaminates, the sample was heated following the lamination thermal cycle, cooled down, heated again and cooled down to room temperature. The first heating cycle can be seen in Fig. 3.15(a) and was measured with thermocouples.

The initial heating shows no deflection below 135°C , as the layers are not tied yet. The bonding temperature is a bit higher than expected, at 135°C . However, the CFRP does not cure under pressure, so the kinetic of the reaction may be different. No difference is observed between the other three curves, indicating that there is no degradation of the bilaminates and no influence of the thermal cycling. The deflection curves can be fit with a simple bi-layer strip model to measure the CFRP CTE, in this case $0.4 \times 10^{-6} \text{K}^{-1}$. This value will be used in the following simulations.



(a) Scheme of the bilaminate.



(b) Deflection curve.

Figure 3.18: Experimental and simulated deflection as a function of temperature for the CFRP/glass structure and corresponding scheme.

3.3.5 Comparison between the experimental deflection and the simulations

The next step is to measure and compare the curvature of another simple structure, made of a 3 mm honeycomb bonded on 0.4 mm CFRP layer with a redux film. At this point it should be mentioned that ideally, the CFRP thickness should be minimised to increase the curvature. However, using only 0.1 mm (single ply) leads to honeycomb energy storage issues that make the curvature measurement difficult. The bilaminates exhibit a preferred bending direction which can be the longitudinal or transverse direction of the honeycomb, depending on the sample. The empirical solution to this issue is to use four CFRP plies. The experimental and simulated temperature-dependent deflection curve of this structure is shown in Fig. 3.19(b). Two different sizes were used.

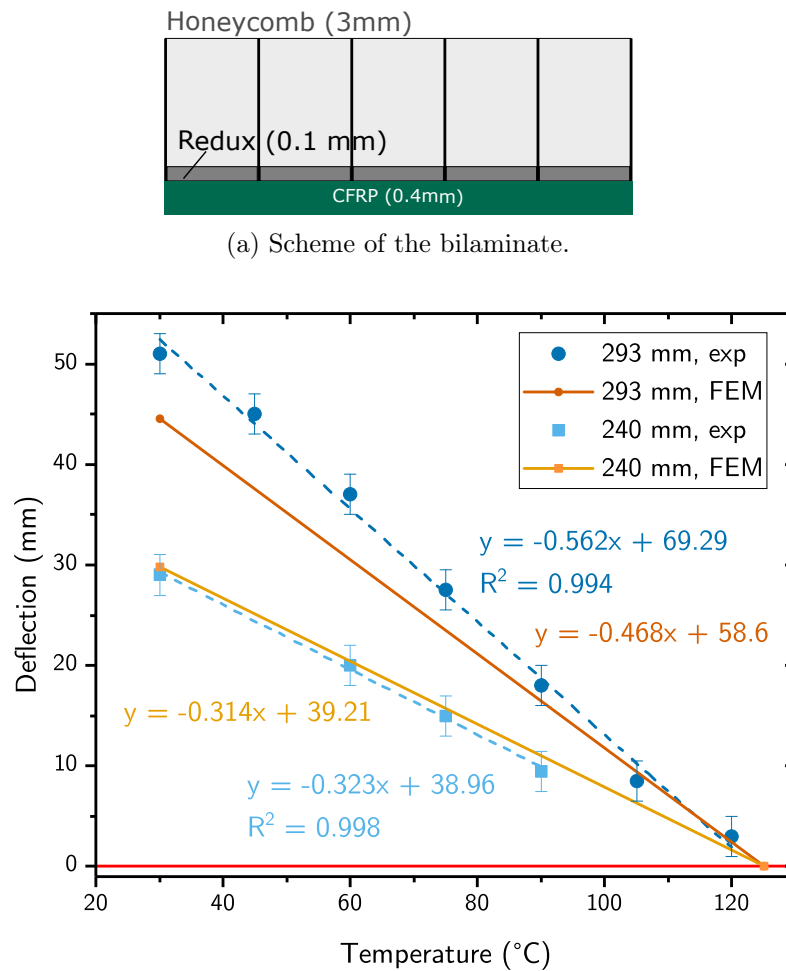
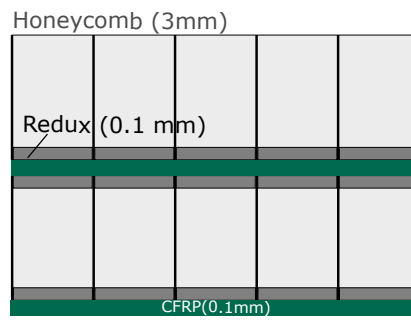


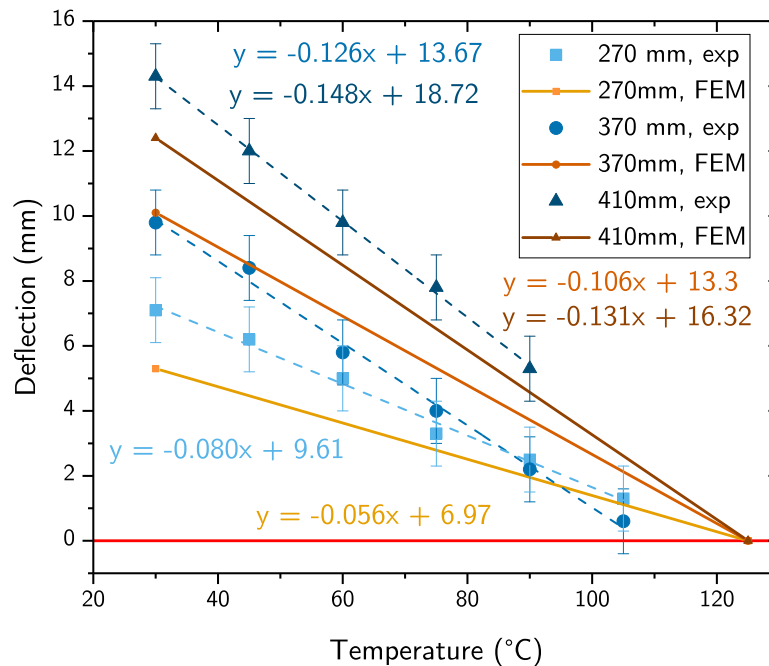
Figure 3.19: Experimental and simulated deflection as a function of temperature for the CFRP/honeycomb structure.

First of all, the reference temperature is the same for the experiments and the models, at around 125°C. Second of all, the model and the experiments show rather good agreement. All curves are linear as expected in this temperature range. Considering the slope of the curves, the relative discrepancy does not exceed 17% for the larger samples.

Afterwards, structures with two 0.1 mm CFRP sheets and two 3 mm honeycombs were manufactured. Unfortunately, using thicker CFRP drastically reduces the deflection and makes the measurements difficult. However, from a qualitative inspection, the energy storage does not seem to be an issue in this case, the structure being way stiffer than the previous one. Nonetheless, there may be an effect on the deflection that cannot be isolated here.



(a) Scheme of the bilaminate.



(b) Deflection curve.

Figure 3.20: Experimental and simulated deflection as a function of temperature for the double CFRP/honeycomb structure.

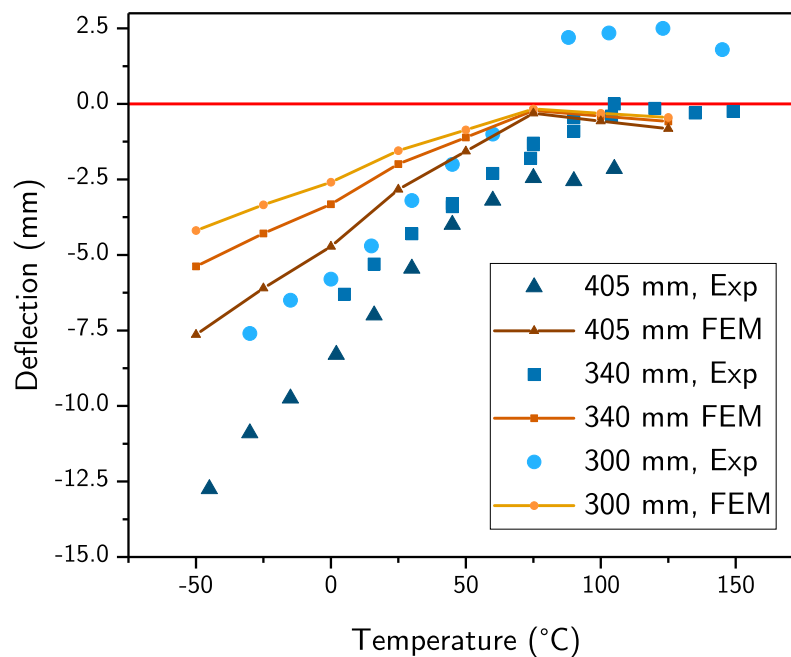
The deflection curves for three sample lengths are shown in Fig. 3.20(b). For two sizes (270 and 410 mm), the reference is once again at around 125°C as predicted by the DSC measurements and expected from the previous bilaminates. In both cases, the simulations underestimate the deflection. However, for the 370 mm samples, it is quite different and is around 110°C. This difference is not explained but hints towards a poorly controlled lamination process.

The relative discrepancy between the slope of the experimental and simulated curves is higher, reaching 30% for the smaller samples. This larger difference may be a result of the energy storage issue or could simply due to the fact that as the structure is more complex. This is to be kept in mind for further work.

Finally, the deflection curves for the full concentrator structure are shown in Fig. 3.21(b).



(a) Scheme of the full structure.



(b) Deflection curve.

Figure 3.21: Experimental and simulated deflection as a function of temperature for the full structure.

Once the glass is finally bonded on the honeycomb with the ablestik epoxy, the deflection curve changes. It can be considered linear in the low temperatures from -50°C to around 60°C . In the high temperature (60°C and above) the slope quickly decreases and the curve is almost flat at 70°C . The deflection even seems to decrease above 100°C but this trend is not clear. The slope discontinuity is also seen in the FEM model. It corresponds to the elasticity modulus of the ablestik collapsing. The epoxy film can no longer withstand the mechanical stress induced by the curvature of the structure. Thus, the glass starts sliding against the honeycomb and the curvature stops increasing again as the CFRP-honeycomb part of the structure tends to bend the other way. From the experimental curves alone, it seems very difficult to precisely predict what happens at this temperature transition. Depending on the sample, the deflection stops at different values (2.5, -2.5 and -2 mm) which do not correspond to the FEM model stopping at 0.2 mm. This difference is not explained. The fact that the

displacement remains small at temperatures above the adhesive glass transition may appear beneficial at first. Indeed, the concentrator structure stays almost flat above this temperature. However, it implies that the glass and the honeycomb slip between them, causing the optics and the cells to be misaligned. This is to be avoided.

Focusing on the low temperature part of the curves, the relative discrepancy between the experiments and the FEM model is higher than for the other simpler structures. The experimental slope is about twice as high than in the FEM model. For rather small temperature changes, the model works fairly well. As the temperature change amplitude increases, the absolute difference becomes quite high.

3.3.6 Updated model for space materials and environment

To build a more realistic model, the materials and boundary conditions of the FEM were changed. The main difference is the material properties, with space-grade materials as inputs. A summary of the properties is displayed in Table 3.4

Concerning the adhesives, they were assumed to be able to withstand space temperature. Thus, their elasticity modulus was considered independent of temperature. Its value for the CFRP/Al, respectively glass/Al adhesive was taken from the -80°C DMA measurements of the redux, respectively ablestik adhesives. The CTE and Poisson's coefficient of both are standard for cured epoxy resins.

The honeycombs were assumed to be 5052-3/16-.002. Thus, the aluminium properties are the ones of the 5052 alloy [119].

Material	E (GPa)	ν	CTE (10^{-6}K^{-1})
Aluminium	69	0.33	23.5
CFRP	169	0.1	1.5
Glass	77	0.2	5.5
CFRP/Al adhesive	1	0.4	30
Glass/Al adhesive	5	0.4	30

Table 3.4: Materials properties used in the design of simulations.

The elasticity modulus of the CFRP was taken from M55J fibres, standard for space applications [120]. A plain weave fabric and 60% fibre volume was assumed. Its CTE was estimated from [121] and [122].

The elasticity and CTE of the glass were taken from the QiOptic CMG glass data sheet [123]. Its Poisson's coefficient was taken from [124].

Regarding the boundary conditions, the initial temperature of the glass, glass/Al adhesive and the part of the honeycomb in contact with the adhesive was set to 150°C . The temperature of the rest of the structure was set to 180°C . This is a simplified thermal load as the temperature would not be homogeneous in the whole panel. However, this is a first step towards understanding and modelling the thermomechanical behaviour of the concentrator in space. As mentioned previously, the models themselves are much smaller than an actual panel. The deflection curve is fitted and extrapolated at the desired length to get the deflection or regular-

sized panels. In this case, the panel length was arbitrarily set to 2 m. This is roughly the length of a LEO panel. Figure 3.22 shows an example of the deflection curve for a configuration at a temperature of 80°C. The deflection will be multiplied by two, taking the model uncertainties into account.

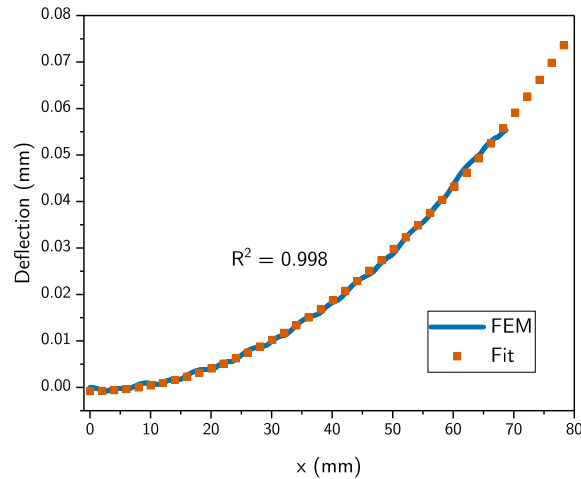


Figure 3.22: Example of a deflection curve from the FEM model (blue line) and the corresponding quadratic fit (orange squares) at 80°C.

At this stage, as getting precise data about space-grade material was not possible, a lot of assumption regarding the materials had to be made. The upcoming results from the FEM simulations should be considered carefully, especially since a lot of differences are expected from the model building presented earlier. Therefore, it is difficult to draw a conclusion on the actual maximum incident angle that will be reached in flight. Notwithstanding, the primary goal of this study is to determine the influence of the thickness of the layers of the structure on the in-flight incident angle. While the absolute angle values may differ significantly from what will happen in reality, the trends given by the statistical analysis are still valuable and give design guidelines for the concentrator. Moreover, it is still possible to get a feel for the order of magnitude of the incident angle. If a 20° angle is predicted for a 2 m long panel, chances are that the design is not suitable for Earth orbits.

3.4 In-flight bending influence on the optical performances

The deflection of a solar array in low earth orbit due to thermal vibrations was studied by Li *et al.* [103]. Two 3 m solar panels with their fixation system for a total length of 6.62 m were considered. According to this work, the vibrations amplitude can reach 200 mm. The normalised bending stiffness of the panels considered can be estimated around $4.5 \times 10^6 N.mm$ using Eq. (3.1), which is very close to our target.

A scheme of a bent panel is shown in Fig. 3.23. Assuming that the micro-concentrator structure would reach the same curvature, the vibrations would have an impact on the incident angle of the light and thus on the optical performances. The maximum incident angle of the

sun rays is noted i_m and w is the maximum deflection. For small deflection values, the shape of the bent panels can be considered quadratic and their radius of curvature R can be determined using Eq. (3.10). In this case it is equal to 110 m, which corresponds to a 18 mm deflection for a 2 m panel. This deflection will be added to the one predicted by the thermal curvature model.

For small angles, the length L of the panel is equal to its projection L' on the x -axis. The value of i_m is then given by Eq. (3.11).

$$R = \frac{\sqrt{L^2 + w^2}}{2 \sin \left\{ \arctan \left(\frac{w}{L} \right) \right\}} \quad (3.10)$$

$$\begin{cases} \cos\left(\frac{\pi}{2} - i_m\right) = \frac{L'}{R} \\ \sin\left(i_m - \frac{\pi}{2}\right) = \frac{w}{R} - 1 \end{cases} \quad (3.11)$$

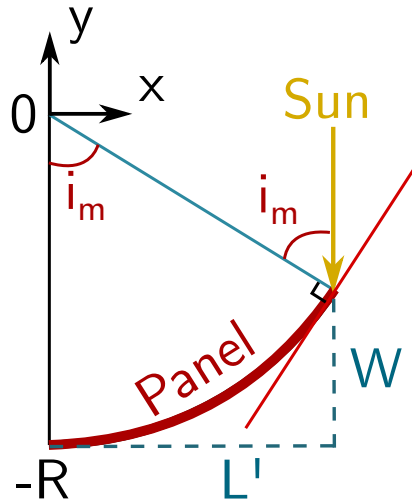


Figure 3.23: Scheme of a bent panel and the resulting modified incident angle of the light.

To reduce the maximum incident angle, it is also possible to purposefully tilt the concentrator to divide it by two [125]. Therefore, the maximum incident angle is the sum of the maximum deflection given by the model and the one from the vibrations. Then, the calculated angle is divided by 2, assuming the panel can be tilted. Then, the maximum incident angle for each configuration is used in the statistical analysis performed with the JMP software. Glass is a brittle material which mechanical strength is low under tensile stress (10 MPa) but high under compressive stress (hundreds of MPa). Thus, it is best to avoid putting the glass under tensile stress. According to the simulations, the maximum stress in the glass is positive for five configurations out of forty only. The negative stress does not exceed -75 MPa.

In the end, the incident angle is between 0.7° and 4° . This is within the range of the AA of the concentrator (4.2°). However, only a 2 m long panel was considered. From Eq. (3.11), it is possible to estimate the maximum panel length that stays within the range of the AA for a specific configuration. The curvature R does not depend on the panel length. Using the simple analytical model developed earlier, it is also possible to determine the corresponding bending

stiffness, neglecting the contribution of the honeycombs and considering a panel width of 1 m. The most interesting configurations were extracted and are presented in Table 3.5.

t_{Nb} (mm)	t_{Nt} (mm)	t_g (mm)	t_{ct} (mm)	t_{bt} (mm)	$i(L = 2m)$ (°)	$L(i = 4.2^\circ)$ (m)	D (N.m ²)
15	3	0.1	0.2	0.8	3.3	2.5	8×10^3
20	3	0.1	0.2	0.8	3.0	2.7	14×10^3
20	3	0.3	0.2	0.8	2.4	3.7	19×10^3

Table 3.5: For three different geometries, maximum incident angle for a panel length of 2 m and maximum panel length for an incident angle of 4.2°.

In every case, the glass is in a compressive stress state. The maximum panel length is compatible with standard flat space panels, with a size of a few metres. However, it does imply that some of the incident power is lost. In the future, ways to control and decrease the curvature should be studied to improve the performances of the concentrator. Furthermore, the bending stiffness target is largely reached, with the lowest stiffness being around $8 \times 10^3 N.m^2$. This is mostly due to the bottom CFRP layer being much thicker (0.8 mm) than on the literature structures considered.

3.5 Conclusion

To conclude, a first study on the bending stiffness of the concentrator was conducted. Through experiments and simulations, the impact of the tool friction was demonstrated. The stiffness target was reached for two configurations out of the six tested. Based on the stress distribution in the main layers of the concentrator, the top CFRP sheet proved to have little to no impact on the stiffness or on the structure. Good agreement was obtained between the analytical model and the FEM one without friction. Guidelines to reach our target, improve the stress distribution and minimise the mass were extracted from those results.

Then, the curvature of the concentrator as a function of its geometry for a determined temperature was also studied. Preliminary material characterisations were performed to determine the properties to be used in finite element simulations. The model built on this data was compared to experiments and yielded rather different results. For a temperature difference of 100°C, the experimental deflection is about twice as high as the predicted one. However, the trends are the same. Therefore, other guidelines to decrease the curvature of the concentrator could be deduced. The glass stress proved not to be a problem since it is negative for the low-curvature geometries.

Combining the results of both studies, the most interesting geometry for the concentrator was defined. The maximum panel length compatible with the AA specification of 4.2° was determined and is equal to about 3.7 m, compatible with standards.

4 Prototype manufacturing and characterisation

4.1 Introduction

After having identified how to assemble the cells on their glass substrate and defined a structure geometry adapted to space conditions, it is time to manufacture a prototype of the micro-concentrator. This chapter presents the manufacturing choices, process and the electro-optical characterisations of the micro-concentrator design. One should bear in mind that at this stage, developing a space and industrial compatible process is not a major concern. Instead, the aim is to manufacture a first functional prototype. This enables the characterisation of its electro-optical performances. In turns, ways to improve the design and the manufacturing process can be identified.

The chapter is divided into three main sections. First, the manufacturing process of the optics is presented. Second, the manufacturing of the front glass and the shading it induces is detailed. Third, indoor and terrestrial outdoor electrical characterisations of the prototypes are presented. Finally, ways of improvement are detailed and explained.

4.2 Optics manufacturing

The optics manufacturing process was developed by A. Bermudez-Garcia in the framework of his thesis [126]. This section presents its main aspects for the sake of clarity.

4.2.1 Structure lamination

The first manufacturing step consist in laminating the honeycomb-CFRP structure. In order to make later characterisations easier, it was decided to mould the optics into a 3 mm thick honeycomb placed on only one layer of CFRP and not the full sandwich structure. To avoid curvature and ensure dimensional stability, the CFRP layer was made laminating four CFRP plies together for a final layer thickness of 0.4 mm. The laminating process is the same as in Chapter 3. The structure is cut to the desired dimensions (5×5 cm) using a diamond wire saw. This ensures a clean cut and no deformation of the honeycomb.

4.2.2 Silicone moulding

The second step to manufacturing the optics is to mould silicone into the shape of mirrors. First, the stainless steel mould (see Fig. 4.1, left) and the structure (see Fig. 4.1, right) are cleaned. Ultrasonic power and isopropanol is used. Then, the stainless steel mould is inserted inside the honeycomb structure.

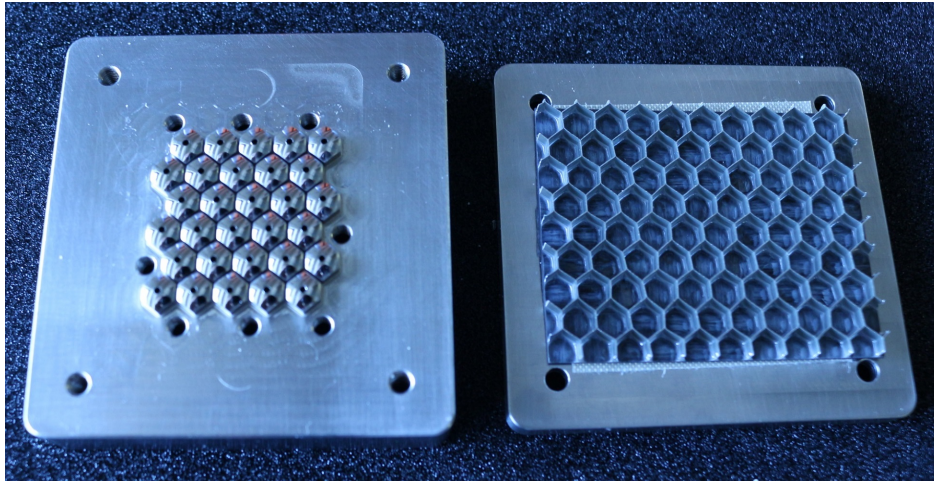


Figure 4.1: Picture of the stainless steel mould (left) and structure (right) prior to silicone moulding.

Another steel plate is screwed on the back of the structure to hold it together with the mould. Then, Dow Corning 93-500 silicone is poured into the honeycomb cells from the back of the mould. The assembly is put under vacuum for about 30 min to remove air bubbles that are trapped in the silicone. bubbles can prevent the silicone from fully filling the honeycomb structure or cause small cavities on the surface of the optics. The silicone is finally cured at room temperature and atmospheric pressure for 24h, as recommended by the manufacturer. For the prototype, the mirror network is made of five rows of rows cells. The mould was designed and the moulding process developed by A. Bermudez-Garcia [127].

4.2.3 Silver deposition

Once the silicone is fully cured, a reflective coating is applied to the optics. Substrate cleaning is crucial to obtain an uniform and highly reflective layer. To this end, ultrasonic cleaning of the moulded silicone with isopropanol for 10 min at room temperature is performed, followed by a 15 min UV/O₃ treatment. The sample is then put under vacuum to outgas for more than 60h to prevent the pressure from rising in the deposition step. This duration was determined empirically. The reflective layer deposition itself is done with PVD in the same vacuum evaporation chamber used for outgassing ($P < 1 \times 10^{-5}$ mbar). Silver was chosen because it was available and its reflectivity can reach 97% [128]. To obtain a high reflectivity, a 200 nm thick layer was deposited. The specular reflectivity of a silver layer deposited on flat silicone surface was measured by spectrophotometry and is shown Fig. 4.2. The thickness was controlled by a quartz scale. In further work, a dielectric coating should be added to prevent silver oxidation [129]. This was unfortunately not available during this thesis.

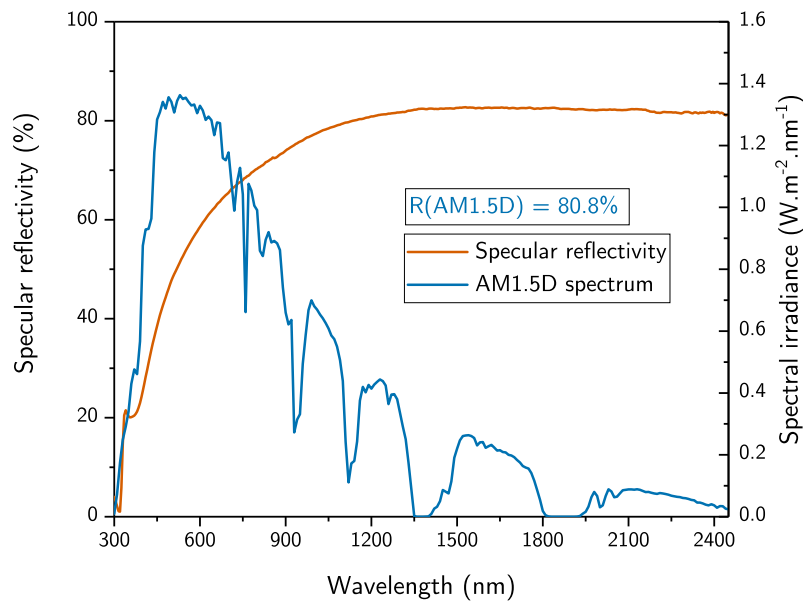


Figure 4.2: Measured reflectivity of a silver layer on a flat silicone surface and AM1.5D solar spectrum between 300 and 2450 nm.

4.3 Front glass manufacturing

4.3.1 Screen printed tracks

The pads and conductive tracks on the glass substrates were manufactured with a screen-printing process for the following reasons:

- High achievable track thickness of 15 μm
- High throughput process, suitable for large scale production
- Patterns can be weldable
- Highly repeatable process
- Dimensional accuracy of about +20-30 μm , compatible with the self-alignment requirements

Regarding the dimensional accuracy of screen-printing, the paste tends to overflow once the screen is removed, resulting in patterns larger than the corresponding openings of the screen. This overflow is of about 20 μm but depends on the size of the screen opening. Very thin patterns (*e.g.* 20 μm lines) exhibit less overflow, large patterns like the receiving pads may exhibit more overflow. For this reason, the openings for the receiving pads were set to 855 \times 655 μm (30 μm smaller than the desired size) in order to end up with the same size as the cells.

A low-temperature, weldable, 92% silver paste was used for its high electrical conductivity and to allow for soldering and wire-bonding later on. After printing, an annealing step was performed at 200°C for 10 minutes in air. The line resistivity was measured and was equal to

0.33 Ω .cm after this step.

Two screens with different meshes but the same pattern geometry were tested. The printed patterns dimensions (Table C.1 and Table C.2) and a comparison between the shape of two pads (Fig. C.1) are shown in the appendix. The second screen, giving better edge definition was used to make the prototypes. No significant differences concerning the dimensions were observed.

To get access to the electrical parameters of the modules and test different interconnection designs, four different substrates were manufactured. Because of the paste overflow described earlier, all the dimensions further given correspond to the size of the openings of the screen, not to the final size of the patterns.

All the designs include a receiving pad for the cell of $855 \times 655 \mu\text{m}$ as explained above. In order to make the wire-bond between the cells top contact and the tracks easier, a welding pad of $200 \times 700 \mu\text{m}$ is connected to the tracks, in front of the cells. The distance between the receiving and the welding is of $215 \mu\text{m}$ to make sure there is no contact between the two, even with the paste overflow. The distance itself has no influence on the resistivity of the track. The last common point between the designs is that the cells are connected in series by thin lines or wires. The string of cells are connected in parallel by larger bars. In the following sections, the series connections will be referred as lines and the parallel ones as bars.

In design A (Fig. 4.3), the six strings of five micro-cells are separated, so that each string can be tested separately. The width of the track varies: two strings with a $20 \mu\text{m}$ opening, two strings with a $40 \mu\text{m}$ opening and two strings with a $60 \mu\text{m}$ opening. It should be noted that $20 \mu\text{m}$ is the smallest dimension the machine can work with. This design goal is to test the influence of the tracks width. A thinner track decreases shading but has a lower electrical conductivity. Moreover, as the strings are individual, it is possible to test only five cells at a time if the manufacturing of a substrate with thirty cells proves difficult.

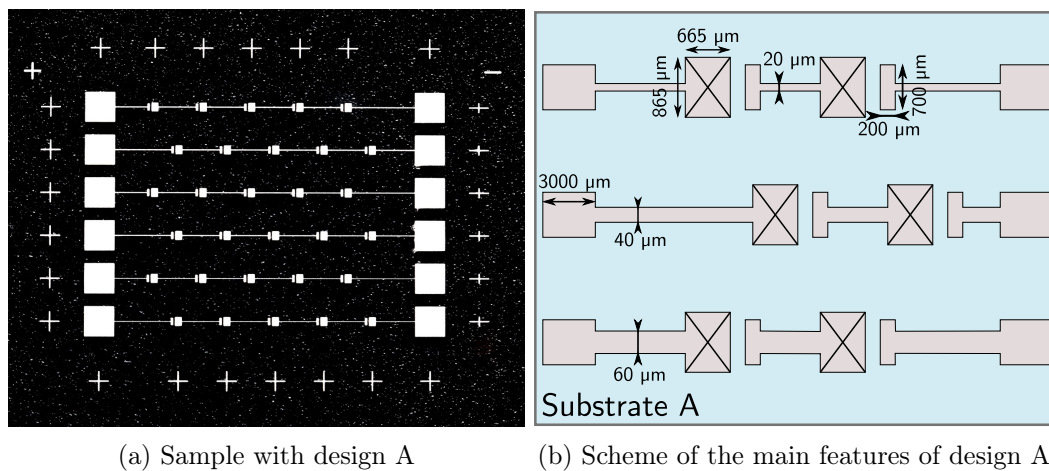
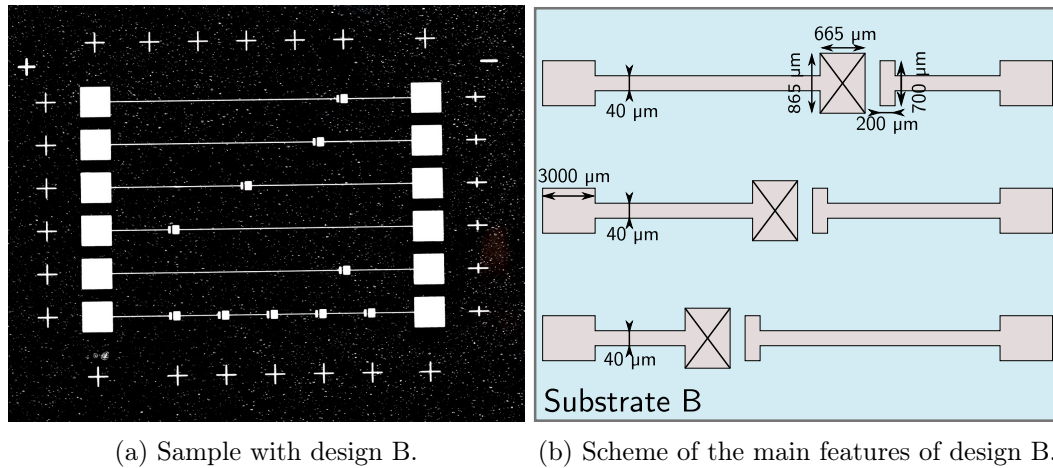


Figure 4.3: Substrate design A.

In design B (Fig. 4.4), five of the six strings only include one cell. This way, the same cell can be characterised with different individual mirrors in order to determine the influence of the mirrors manufacturing tolerances. As for design A, if the manufacturing of a full 5-cell string proves difficult, it's possible to work with only one cell.

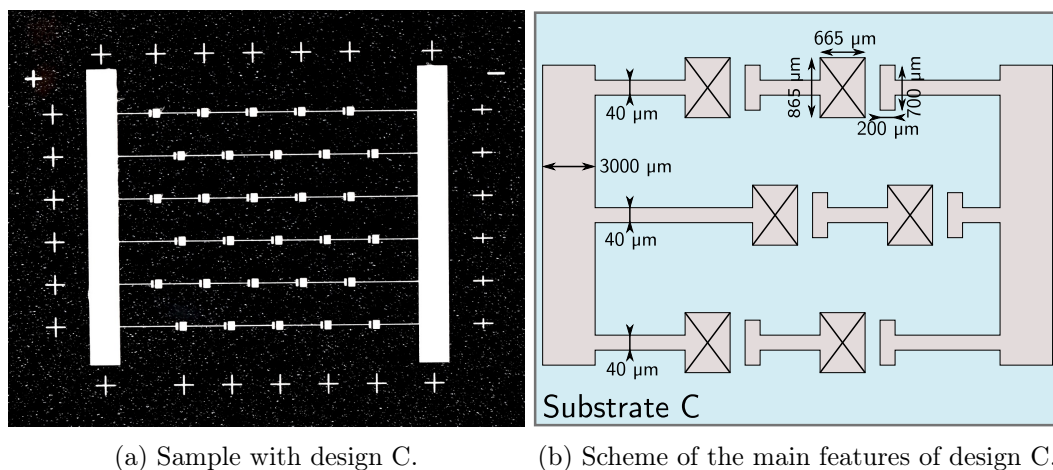


(a) Sample with design B.

(b) Scheme of the main features of design B.

Figure 4.4: Substrate design B.

Design C (Fig. 4.5) is designed for a full mirror network. The six strings are connected in parallel. The aim is to characterise the performances of a full prototype.



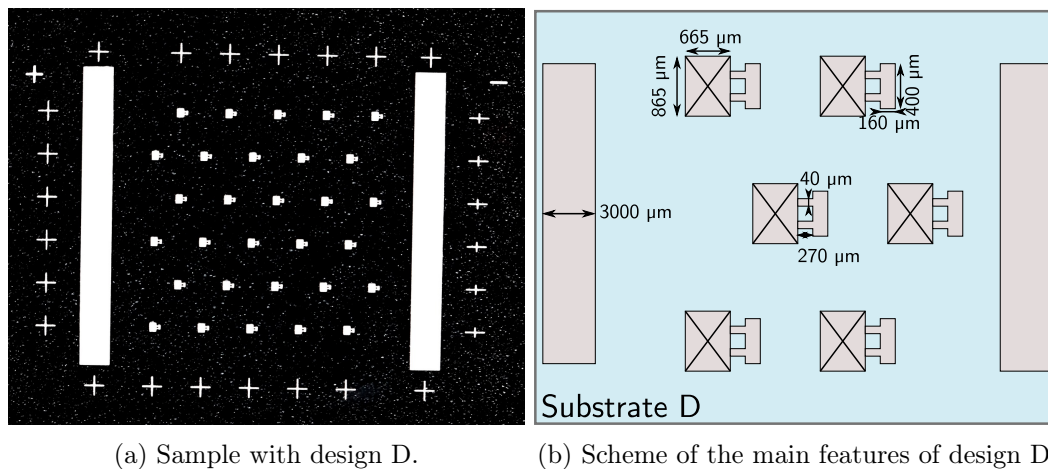
(a) Sample with design C.

(b) Scheme of the main features of design C.

Figure 4.5: Substrate design C.

Design D (Fig. 4.6) is similar to design C in the way that it's meant to be used with a full mirror network as well. The strings are also connected in parallel. The differences with the other designs is that there are no tracks. Instead, a small welding pad is added to the receiving pads. The tracks are replaced by a long wire bond between the top contact of a cell and the nearest welding pad. The aim is to decrease the shading of the tracks to a minimum. The welding is made of two thin paths leading to a larger rectangle of $160 \times 400 \mu\text{m}$. The paths

are $40\ \mu\text{m}$ thin to prevent solder overflow and the cells being displaced during self-alignment. The welding rectangle itself is smaller than in the other designs to reduce shading further.



(a) Sample with design D.

(b) Scheme of the main features of design D.

Figure 4.6: Substrate design D.

A summary of the main characteristics of the different designs are displayed in Table 4.1.

Design	Strings	Cells/string	Track width (μm)
A	Single	5	20, 40, 60
B	Single	1	40
C	Parallel	5	40
D	Parallel	5	No tracks

Table 4.1: Summary of the different substrate designs.

4.3.2 Soldering with self-alignment

Once the different designs were separated, 3J micro-solar cells were soldered on the receiving pads. I did a two-month internship at Fraunhofer ISE in March and April in 2023, which allowed me to perform some manufacturing steps and characterisations that will be detailed later on. The solar cells were soldered at ISE with the following process:

- Substrate cleaning with isopropanol
- Pressure controlled $\text{SnAg}_{3.0}\text{Cu}_{0.5}$ solder dispensing
- Pick & place placement of the cells
- Soldering in a reflow oven under nitrogen

A detailed temperature profile during soldering can be found in Fig. B.1(b) (appendix). The placement accuracy of the process was characterised and the detailed results can be found in Fig. D.1 (appendix). Overall, the cells were placed with an accuracy of $\pm 35\ \mu\text{m}$ for the in-plane translation and $\pm 1.5^\circ$ for the in-plane rotation.

4.3.3 Wire-bonding

The initial idea was to use wire-bonding to connect the tracks (soldered to the reverse side of the cells) to the front side of the cells as in Fig. 4.7. However, the screen printed silver welding pads proved to be unsuitable for wire-bonding. Using high ultrasonic power, the pad would be torn from the glass. With low ultrasonic power, the wire could not be bonded onto the pad. This is mostly likely due to silver oxidation degrading the bonding ability of the surface. To overcome this technical issue, small metal bits were cut from a 300 μm thick copper sheet with a gold surface finish. These copper bits were then soldered on the welding pad and connected to the front side of the cells with wire-bonding. A 25 μm diameter gold wire was used. Schemes of the interconnection design for the different substrates are shown in Fig. 4.7(a) with the corresponding picture in Fig. 4.7(b). Due to the lack of an appropriate cutting tool, the copper bits were manually cut. Henceforth, their size was poorly controlled and varies from one bit to another. Thus, it is difficult to estimate the final shading due to the electrical connections of the substrate, but it is slightly higher than designed. The copper bits were also placed manually with tweezers, but their position has little impact on the electrical performances of the prototype, only slightly increasing the shading if misplaced.

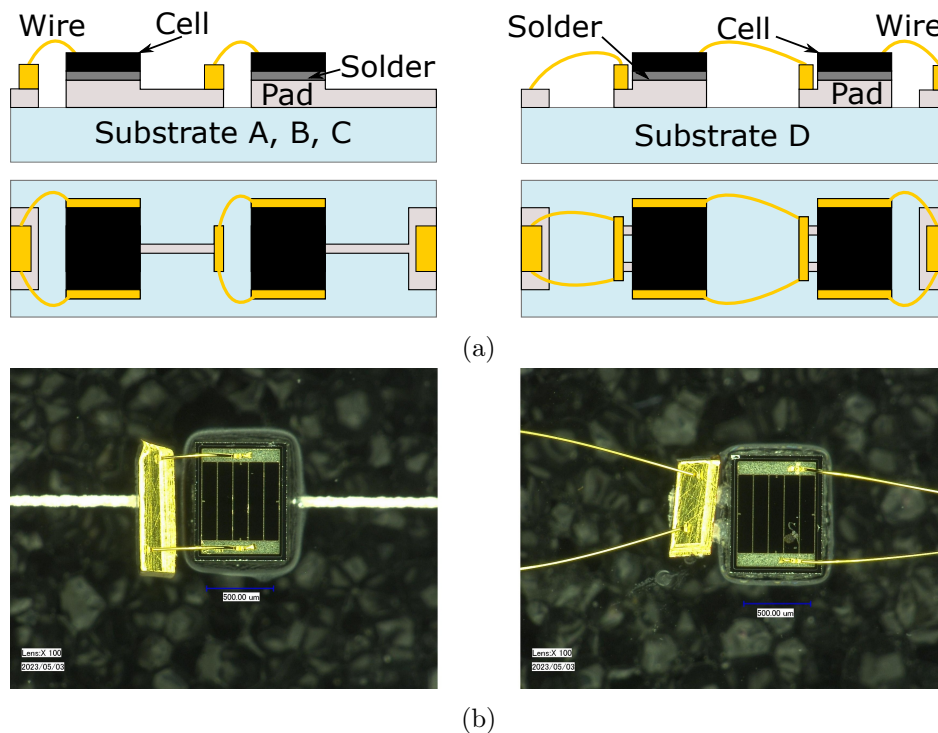
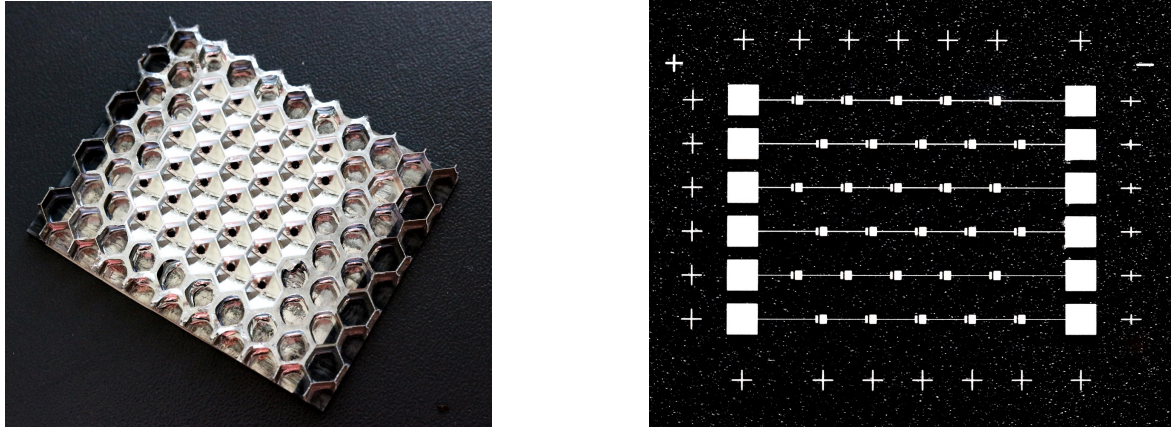


Figure 4.7: Scheme (a) and corresponding picture (b) of the wire-bonding designs.

4.3.4 Assembly

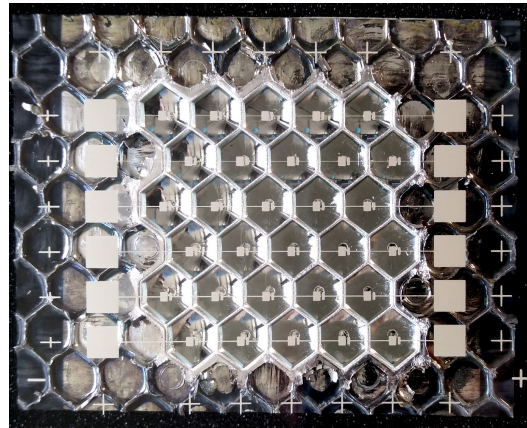
Figure 4.8 shows pictures of the optics, a design A substrate and both parts on top of each other. Ideally, the glass substrate should be aligned and bonded to the honeycomb to have a monolithic module that does not require more assembly steps. However, this means

one network of mirrors is necessary for each substrate and it will not be possible to study the alignment tolerances. So, the substrates were not bonded at this stage.



(a) Picture of the optics.

(b) Picture of a design A substrate.



(c) Picture of the assembly.

Figure 4.8: Pictures of the optics, a design A substrate and the assembly of both parts.

4.3.5 Manufacturing summary

Because of the time consuming manufacturing processes, one front glass of each design was fully manufactured. Due to the delicate and manual nature of the front glass manufacturing process, some samples were damaged. In the end:

- Design A substrate: one of the two 20 μm wide tracks was cut, making the associated string not functional.
- Design B substrate: fully functional.
- Design C substrate: fully functional.
- Design D substrate: three welding pads were ripped from the glass during the wire-bonding step, making one string not functional.

All designs will be used in the upcoming characterisations, taking their disparities into account.

4.4 Electro-optical characterisations

In the first part of this chapter, we described the manufacturing process of the prototypes. The next is then to assess their electro-optical performances. To do so, current-tension (IV) measurements were performed at ISE in Freiburg in the framework of the two-month internship described earlier. First, dark IV (DIV) measurements were used to compare the series resistance of the different line widths. Then, outdoor measurements were performed to characterise the electrical performances of the designs and the cell-optic misalignment tolerances. First, the B design (*i.e.* the one with a single solar cell) was characterised to determine the power output of the most simple device. Second, a cell-optic tolerance study was performed thanks to the same design to understand the alignment constraints. Third, the C and D design with multiple cells were also characterised to assess the performances of larger-scale devices. Afterwards, indoor measurements helped compare the different interconnection designs and understand some of the limitations encountered during the outdoor measurements. Finally, an optical losses analysis is discussed to understand how to improve the power conversion efficiency of the micro-concentrator.

4.4.1 Current-tension measurements

To compare the series resistance induced by the different line widths, DIV measurements were performed on the strings of the design A substrate. More information about the set-up are presented in the appendices. Figure 4.9 shows the corresponding DIV measurements for line widths of 20, 40 and 60 μm . As mentioned earlier, one 20 μm line was damaged. Moreover, one 40 μm line was heavily shunted and is not shown here.

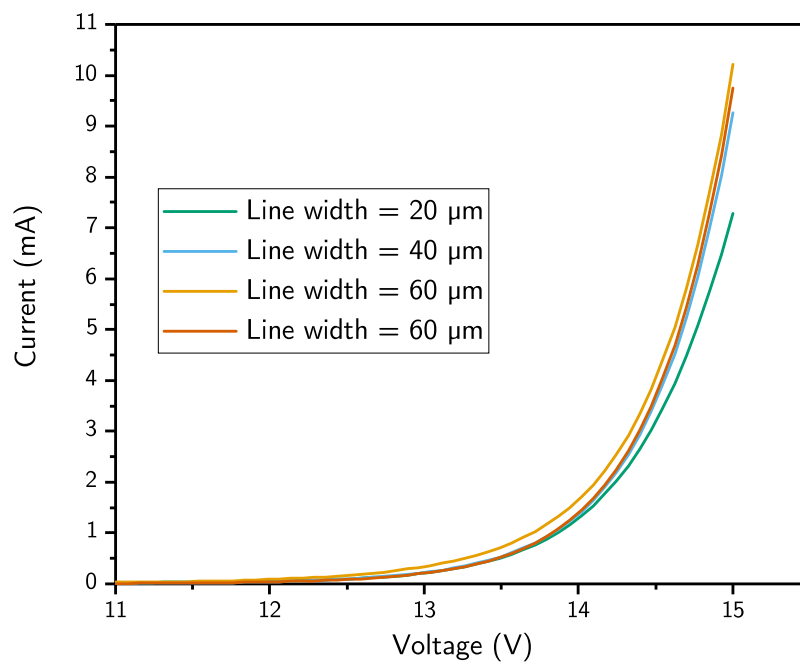


Figure 4.9: Dark-IV measurements results for design A (strings of six serially connected cells with varying electrical track width).

The series resistance of the 20 μm line is higher than the other ones, as indicated by the slope of the curves in the high-voltage domain. A much smaller difference can be observed between the 40 and 60 μm lines, but it is hard to conclude if it is due to the series resistance or to something else like the solder layers or wire-bonding. Besides, the difference stays small even for much a higher current intensity of 8 mA.

As a conclusion, 20 μm lines are not suitable for this concentrator. Both the 40 and 60 μm are, but the 40 μm lines cause less shading and are thus the best choice at the moment. Concerning the larger bars, one can assume that the correct width is 40 μm multiplied by the number of strings to be connected in parallel.

Outdoor IV measurements were performed to evaluate the electrical performances of the full devices (substrate and optics together). An optical bench was put together and a scheme is displayed in Fig. 4.10. A steel axis was mounted on a base plate. The optics and the substrate were mounted separately on this axis. Three micrometre stages were used to control the three translations of space.

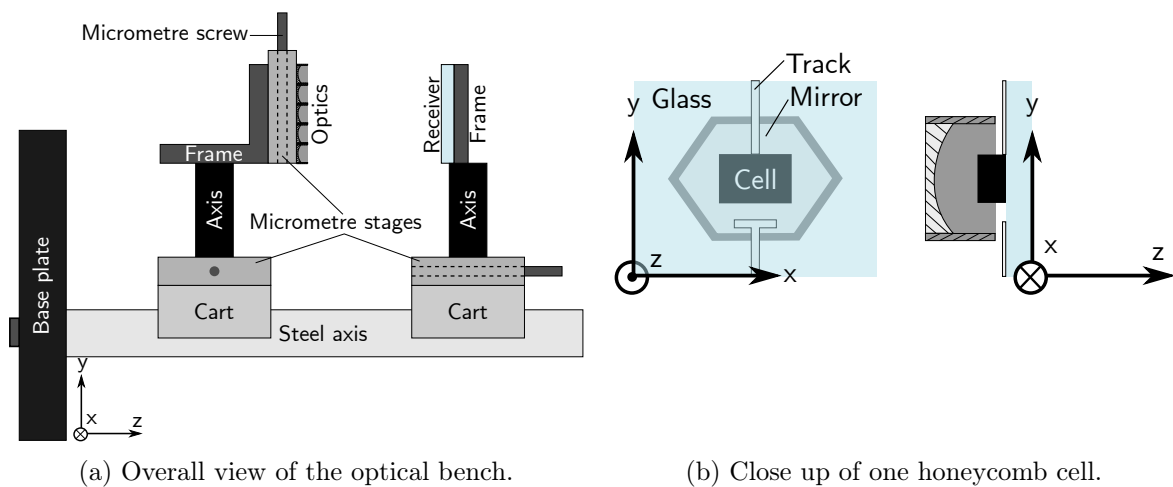


Figure 4.10: Schemes of the outdoor measurements set-up and coordinate system chosen. Complete view (left) and close-up (right).

Then the optical bench was mounted on a double-axis tracker. A picture of the set-up is shown in Fig. 4.11. The Direct Normal Irradiance (DNI) was measured with two separate pyrheliometers, one mounted on the same tracker as the concentrator and one mounted on another tracker. A mean DNI value was finally used and the relative discrepancy between the two did not exceed 0.2%.

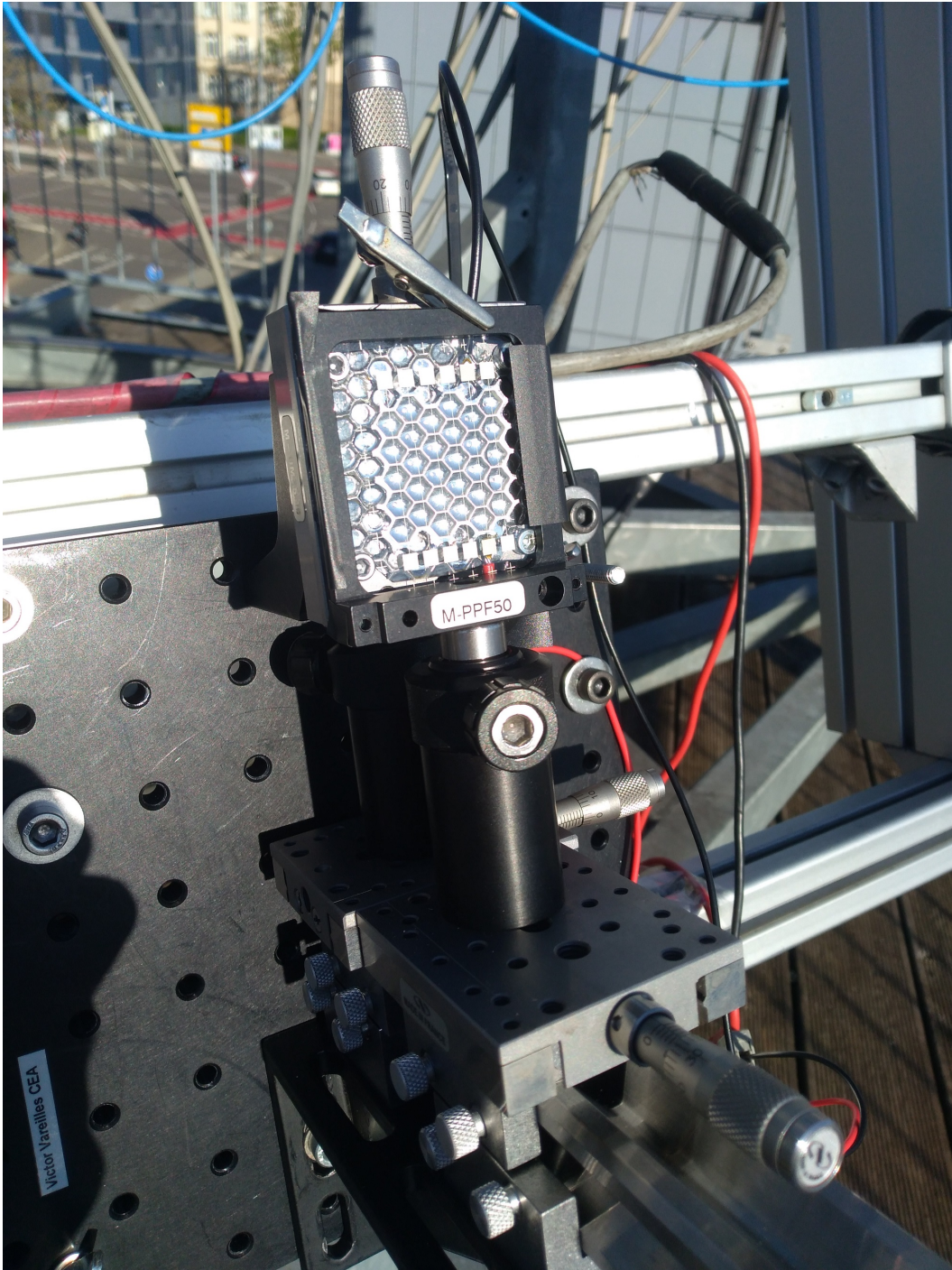


Figure 4.11: Outdoor IV measurements set-up.

Figure 4.12 shows the illuminated outdoor IV curve for the design B (one cell). The measurement was done under a DNI of 905 W.m^{-2} with a spectral matching ratio of 1.02. The ambient temperature was equal to 13°C . The V_{oc} is 2.8 V as expected from a 3J solar cell. The FF is rather high at 85% which makes sense because the current is low. Considering the light collecting area as the area of one optic (*i.e.* 21 mm^2) and the DNI, a PCE of 21% was achieved with this design.

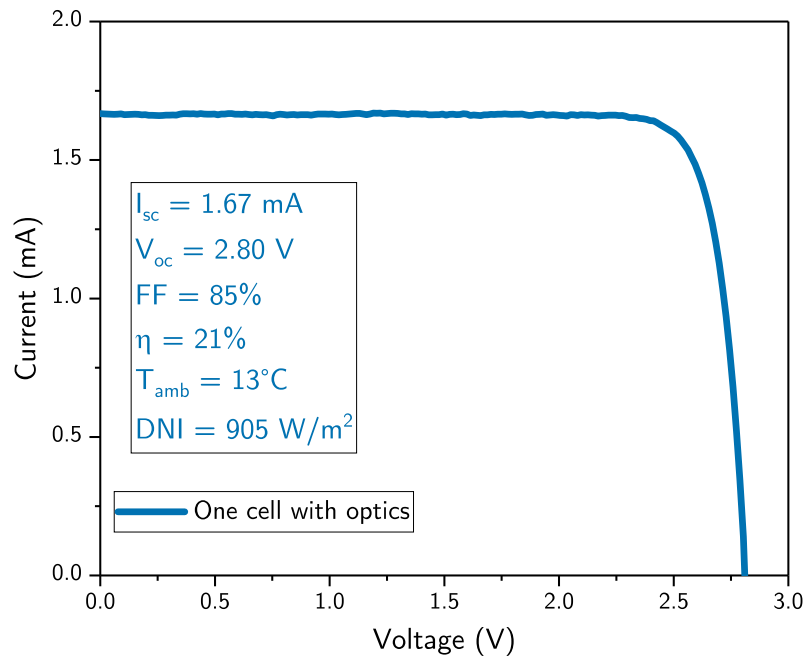


Figure 4.12: Outdoor IV curve for the design B (one cell), measured outdoors in Freiburg, Germany on April 21st, 2023.

Nonetheless, thanks to the micrometre stages, it is possible to perform a cell-optic alignment tolerances study. Figure 4.10(b) shows the coordinates system chosen for this study. Figure 4.13 shows the I_{sc} as a function of x , y and z translations.

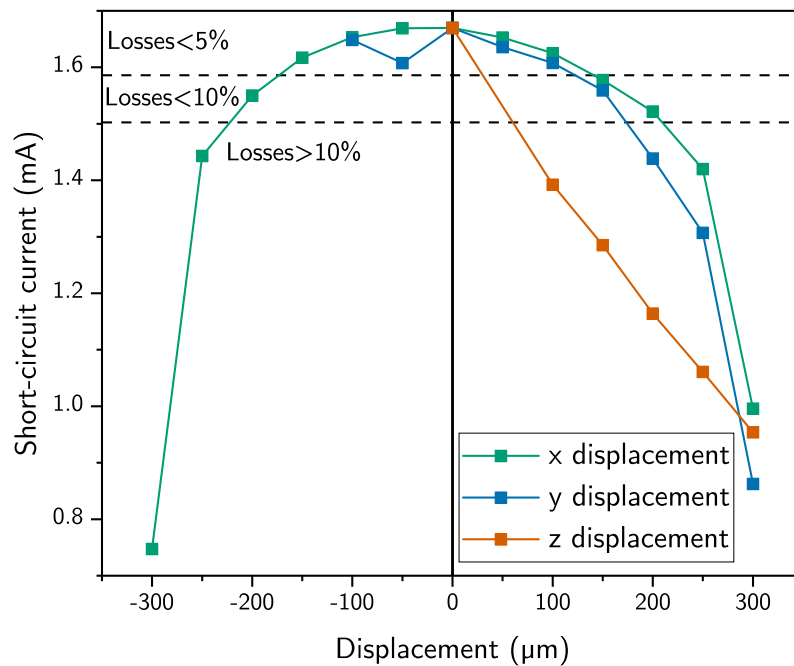


Figure 4.13: Impact of the cell position on the short-circuit current of the design B. Measurements were done outdoor in Freiburg, Germany on April 21st, 2023.

The 0 position is the position at which the maximum short-circuit current was measured. First, focusing on the x -displacement curve, the current curve is roughly symmetrical with respect to the zero position. The imperfections may be due to a small rotation of the cell or an imperfect x -alignment. Second, the y -displacement is slightly more critical than the x one. This is because of the stretched hexagon shape of the mirror. The negative y displacements are not shown since weather issues made the measurements unusable. Last, the z -displacement is by far the most critical and the curve looks fairly linear, even for small displacements. This indicates that the glass substrate should probably be placed closer to the mirror. Indeed, the optic is designed to work with the glass resting on the honeycomb walls. However, placing the glass closer to the honeycomb results in its wall touching the tracks, causing a short circuit. This is also why there are no negative z -displacement measurements. Therefore, one can assume that the thickness of the glue layer that should bond the glass to the honeycomb is critical and an improved optical design should take it into account. Nevertheless, high in-plane cell-optic alignment tolerances were measured. The current losses reached 5% for about a 100 μm y -displacement, which is largely compatible with the achieved self-alignment tolerances of $\pm 30 \mu\text{m}$.

Outdoor measurements were also performed with the C substrate (6 parallel strings of 5 serially connected cells) as it is the full prototype. Its IV curve with the highest power output measured is shown in Fig. 4.14.

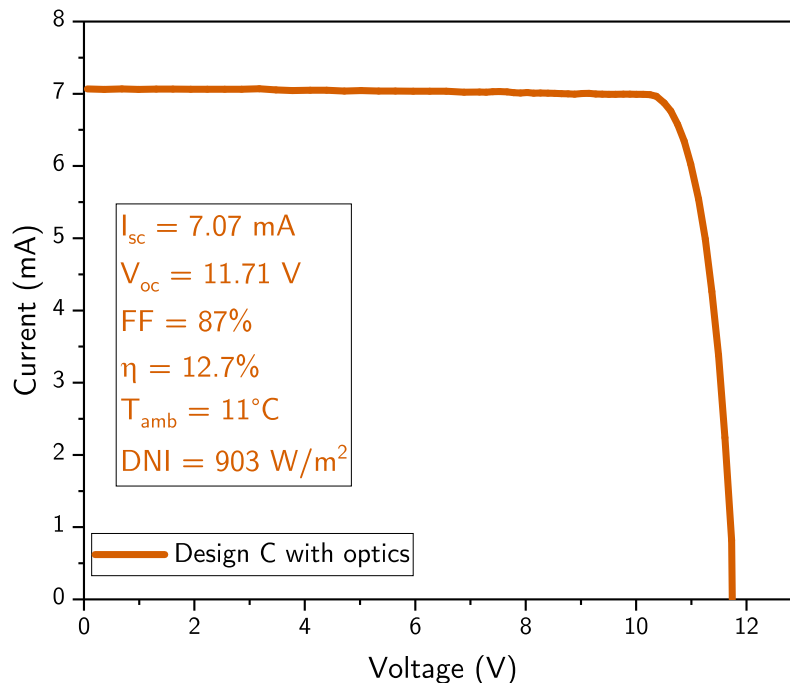


Figure 4.14: Outdoor IV curve for the design C (6 parallel strings of 5 serially connected cells), measured outdoors in Freiburg, Germany on April 21st, 2023.

The DNI was equal to $903 \text{ W}\cdot\text{m}^{-2}$, the spectral matching ratio to 0.99 and the ambient

temperature to 11°C. Without any proper rotation control, aligning the plate to the optics is difficult and the misalignment has a much higher influence than with a single cell. A small rotation of the substrate induces a high translation of the cells at the edges of the substrate. Thus, the I_{sc} is significantly lower than the 9.42 mA expected for five cells in parallel. Furthermore, the V_{oc} is lower than the 14 V expected, which is due to a shunt of one of the strings. In the end, a PCE of 12.7% was achieved, considering the surface of the 30 optics. One can safely assume that improved rotation control would significantly increase the PCE. The shunt due to manufacturing could be rather easily avoided but it was not possible to manufacture and characterise another substrate. Considering a V_{oc} of 14 V (five times the V_{oc} of the B design), an efficiency of 15.1% might be obtained.

To compare the electrical characteristics of the different designs, indoor IV measurements were performed with the AM1.5G spectrum. A single non-collimated source Pasan solar simulator, chosen because of its spatial spectral uniformity was used. The ambient temperature was 25°C. The measurements were performed without the optics. The irradiance and therefore the concentration used was determined based on outdoor measurements. An IV measurement of the B design substrate was performed outdoor under a GNI of 1049 $W.m^{-2}$ without the optics, giving an I_{sc} of 0.06 mA. This current value was used as the reference. Therefore, the absolute irradiance is not well-defined but the irradiance ratio between the measurements is. Moreover, for each measurement, the current is scaled to the same irradiance but its precise absolute value is unknown. Nonetheless, one is shown as a mean to compare the different substrates. Figure 4.15 shows the indoor illuminated IV curves for the B, C and D (5 parallel strings of 5 serially connected cells) designs.

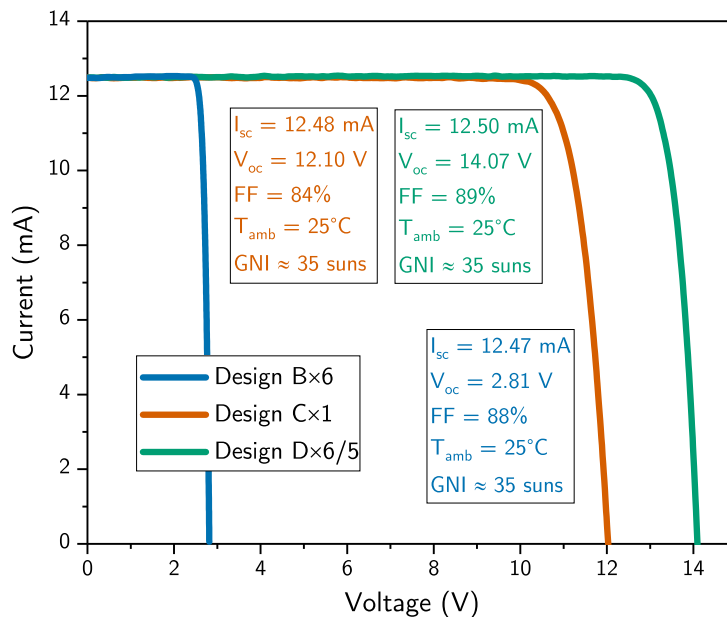


Figure 4.15: Indoor IV curves for the designs B (one cell), C (30 cells) and D (25 cells). Uncalibrated measurements performed with the AM1.5G spectrum.

The current was scaled to an approximate concentration ratio of 35X. As the designs B, C and D respectively include 1, 6 and 5 cell strings in parallel, the current was respectively multiplied by 6, 6/5 and 1 to make the comparison easier. With this assumption, the I_{sc} is the same for the three substrates, despite the different interconnections designs or number of cells. Moreover, the V_{oc} of the D design is equal to 5.01 the V_{oc} of the B design, meaning that the interconnections cause no voltage losses. However, the C substrate seems to be shunted as the V_{oc} of 12.1 V is about 2 V lower than expected. The most likely explanation is a manufacturing issue when soldering the metal welding pads. Some may be in contact with the closest receiving pad, creating another electrical path. Moreover, the indoor V_{oc} of the C design is higher than its outdoor V_{oc} of 11.71 V by about 0.4 V. As a V_{oc} difference of only 0.01 V is observed between the indoor and outdoor measurements of the B design, the effect of the temperature alone can be ruled out. This hints towards edge-recombination losses for some cells receiving a very low irradiance outdoor, most likely the ones far away from the substrate centre. Concerning the FFs, the range between 0.84 and 0.89, which is consistent with the outdoor measurements.

4.4.2 Optical losses analysis

A first theoretical optical analysis of the micro-concentrator was performed by Bermudez-Garcia *et al* [126]. The optical efficiency was estimated to be equal to 74%. A summary of those results are displayed in the first column of Fig. 4.17. A 400 μm thick borosilicate coverglass with no Anti Reflective Coating (ARC) was considered, resulting in Fresnel reflection losses of 4.14% on each side. The absorption of the glass was considered equal to 0.24%. The losses due to the silver reflective coating were estimated based on state-of-the-art silver deposition on polymers [129, 130]. The shading losses were calculated taking the cells and a simplified electrical track design into account, *i.e.* a single 100 μm wide track running through the complete honeycomb cell. The losses due to moulding errors were estimated to 10.6% by topographical reconstruction of the moulded optics and ray tracing. Ultimately, a theoretical optical efficiency of 74% was thus determined.

Having manufactured the prototypes, it is now possible to evaluate the shading more precisely, based on the actual design and experimental measurements. The shading sources are displayed in Fig. 4.16(a). The shading caused by the honeycomb walls, the pads, the tracks and the wires was investigated for the different designs. The associated calculated values are shown in Fig. 4.16(b). The designed values are calculated using the designed layout dimensions. The Exp, profilometer values are calculated using the dimensions shown in Table C.1 and Table C.2 for the screen 2. The standard error bars correspond to the minimum and maximum values. The Exp, image treatment values were measured on fully manufactured samples with image recognition. The gold wire diameter d was set to 25 μm and the pad length B_L to 700 μm .

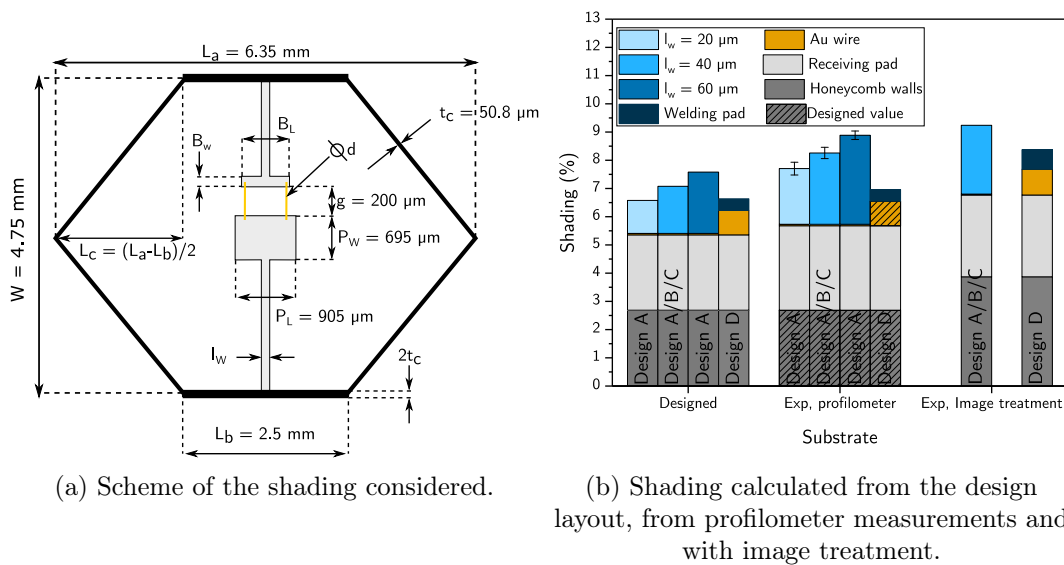


Figure 4.16: Scheme of the shading considered (left) and calculated values (right).

The designed shading ranges from 5 to 8%, depending on the interconnections. About a third of it is solely due to the honeycomb walls and another third to the receiving pad. It cannot be made much smaller because the cell is $885 \times 685 \mu\text{m}$ anyway. The tracks have a rather high influence. From the design perspective, reducing the line width from 60 to $20 \mu\text{m}$ should decrease the track shading threefold. However, the paste overflowing prevents this and the track shading can be reduced by 50% at best. The welding pads have a low influence on the shading (0.8%). The gold wires cause little to no shading (0.05%). Compared to the previous theoretical estimation, the actual shading is about twice as high, mostly because of the wider honeycomb walls. However, this difference to the honeycomb may also be due to the wall edges being hard to properly identify with image processing.

The main way to decrease shading would then be to use a thinner-walled honeycomb. The tracks cannot be made with an opening smaller than $20 \mu\text{m}$ with the screen-printing set-up that was used. The $20 \mu\text{m}$ line would be the best option to reduce shading but also proved extremely brittle and easy to damage during manufacturing. Using $40 \mu\text{m}$ lines seems to be the all round best option as they would only increase shading by 0.6% at worst compared to the $20 \mu\text{m}$ ones. The receiving pad size should be decreased but the cell being only $20 \mu\text{m}$ smaller than the largest receiving pad, the gain would be 0.1% at best.

For the B and D designs, the shading was also calculated with image treatment. A microscope picture was taken and used to determine the shaded surface. The shading is equal to about 9.5% of the total honeycomb cell surface for the B design and to about 8.7% for the D design. This is higher than estimated and can be explained marginally by the added welding pad and some solder flux around the receiving pad. More importantly, the honeycomb walls cause much more shading than expected, about 4.2% from image treatment. Besides, the shading difference between the two types of interconnections is of 0.8%, which is relatively small.

Moreover, to try to get closer to the prototype optical losses, the measured specular re-

flectivity of a silver layer deposited on a flat silicone sample will be used instead of the state of the art value (see Fig. 4.2). Considering the AM1.5D spectrum, the specular reflectivity is equal to 80.8% over the range of 300 to 2450 nm.

Finally, there are other losses sources that are difficult to estimate. As explained earlier, the cell-optic alignment is done manually and could reasonably be improved. Most importantly, the cell proved to be too far away from the substrate. The linear shape of the z -displacement curve shown in Fig. 4.13 prevents us from extrapolating the current that could be reached. Nonetheless, it is certain that it could be significantly improved.

Now that the optical losses sources have been identified, there are different ways to improve the optical efficiency of the device. A summary of the theoretical, experimental and targeted optical losses is presented in Fig. 4.17.

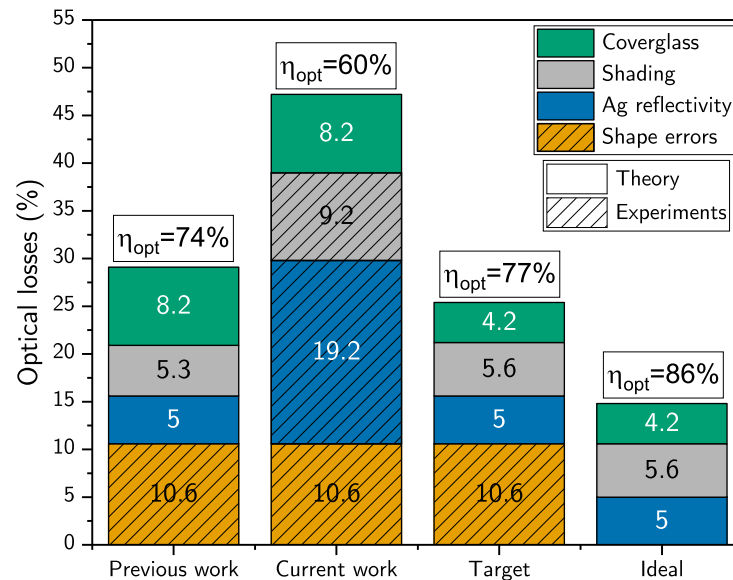


Figure 4.17: Optical losses and optical efficiency estimated from the previous work [126], from this work, targeted and in the ideal case without shape errors.

(i) First, an ARC could be added on both sides on the cover glass to decrease the Fresnel reflections to about 2% on each side of the cover glass.

(ii) Second, to our knowledge, the walls of the 3/16 honeycombs manufactured by Hexcel can be as thin as 0.0007 inches, decreasing the shading by up to 2.7%. Using the D design interconnections (without electrical tracks) could further decrease the shading by 0.8% compared to the B design (40 μm wide tracks). Reducing the receiving pad to the dimensions of the cells would decrease the shading by another 0.1%, which is marginal.

(iii) Finally, the silver reflective coating deposition process could be massively improved. Reaching the state-of-the-art reflectivity would decrease the optical losses by another 14.2%. Taking those areas of improvements into account, the current estimated optical efficiency

of could be improved significantly, realistically reaching 77% taking the shape errors into account. For a concentrator with a single solar cell (B design), the PCE would then be increased from 21% to around 27%.

4.5 Conclusion

To conclude, the first prototypes of the micro-concentrator were manufactured. Screen-printing proved to be a good method to manufacture pads with precise dimensions and to solder the cells. However, because of silver oxidation, wire-bonding on this surface was not possible. Instead, additional metal sheets had to be soldered.

Indoor IV measurements were performed on the substrates B (on cell), C (6 parallel strings of 5 serially connected cells) and D (5 parallel strings of 5 serially connected cells). Substrate C exhibited an important shunt responsible for a significant V_{oc} loss of about 2 V.

Different widths for the electrical tracks were tested. The 20 μm were very brittle and easy to damage. Dark-IV measurements were performed and showed that 40 μm tracks were enough to avoid resistive losses due to the track. No clear difference was observed between the 40 μm and the 60 μm tracks.

Outdoor IV measurements were also performed on the same substrates with the optics. A PCE of 21% was achieved for a one cell-optic system, under a DNI of $905 \text{ W}\cdot\text{m}^{-2}$ and an ambient temperature of 13°C . A cell-optic alignment tolerance study was performed. It showed that a 100 μm in-plane tolerance only induced losses up to 5%, which is compatible with the self-alignment process tolerance of $\pm 30 \mu\text{m}$. However, the out-of-plane tolerance is more critical and a 50 μm displacement is enough to lose 5% PCE. The thickness of the adhesive film that will bond the glass onto the honeycomb is critical.

The optical losses and the resulting optical efficiency of the device were assessed, based on former theoretical work. In particular, the shading due to the interconnections, the cells and the honeycombs walls were theoretically estimated to 6-8%. The measured shading is around 9%. This difference can be explained by the honeycomb walls causing more shading than expected. The optical efficiency of the B design prototype (one cell) was estimated to 60% and could realistically be increased to 77% by adding an ARC, decreasing the shading and improving the reflective coating. This would in turn significantly improve the PCE of the device, from 21% to 27%. For further characterisation work, substrate rotation control and a better alignment system should be added to the IV bench to improve the PCE, especially on larger scale modules. Besides, measurements could be performed using the AM0 spectrum.

5 Conclusion & outlook

Space industry is currently booming. Space power generation demand has been steadily increasing in the last years and the growth is expected to carry on in the future. This increase is driven by the need for high production volumes of low cost, low mass and low volume PVAs. Besides these constraints, space environment is particularly harsh and the arrays must withstand high-amplitude thermal cycling, mechanical stress and radiations among other factors. Other approaches meaning to compete with the standard CIC architecture with III-V on Ge cells are being developed. Concentrator photovoltaics is a flight-tested solution that aims to decrease the PVAs costs by focusing the sunlight onto submillimetre scale solar cells, thus greatly reducing the amount of expensive semi-conductor materials needed. This technology also demonstrated high radiation hardness compared to standard technologies. However, micro-concentration requires an optical system to focus the light and comes with its fair share of challenges. The added mass and volume of the optics hindered its development, but this approach is gaining interest again with the down-scaling of the components and high levels of integration, reducing the mass and volume of the micro-concentrators and improving their thermal management and efficiency. Nonetheless micro-concentration still has challenges to take up. Since the solar cells are micrometric, they need to be aligned with the optical system with an accuracy of a few dozens microns. In that regard, capillary self-alignment techniques are of great interest to the micro-electronic field and promise to achieve high throughput and high accuracy assembly. Besides, thousands of such cells must be assembled to make a single PVA, which requires quite some time with current assembly techniques, increasing the manufacturing costs. Then, once the micro-concentrator is launched into space, it must withstand the harsh environment described earlier. In particular, mechanical and thermal stress strongly depends on the concentrator design. Furthermore, the optical system will be affected by the temperature-induced vibrations and curvature of the system. Finally, as the design is new, its manufacturing process must be defined and its electrical performances assessed experimentally.

Therefore, this work aimed to:

- Understand the limitations and mechanisms of capillary self-alignment with a molten solder
- Identify ways to improve such a process
- Understand the influence of the concentrator geometry on its bending stiffness and in-flight curvature
- Define design guidelines to maximise the concentrator bending stiffness while minimising its curvature, mass, volume and the glass mechanical stress.
- Manufacture the first prototypes of the micro-concentrator

- Perform electro-optical characterisations on said prototypes
- Identify areas for improvement of its power conversion efficiency

First, the challenge of the precise assembly of solar cells was tackled. Based on a state of the art of capillary self-alignment, study criteria were defined. The influence of the solder volume, the pad size compared to the cell size and the initial displacement of the cell were studied experimentally. At the same time, an analytical and a numerical model of the capillary forces during the process were built and their relative discrepancy did not exceed 10%. A large solder volume significantly decrease the capillary forces and thus the self-alignment accuracy. What's more, it can lead to the formation of a so-called solder pillow, inducing a high out-of-plane rotation of the cell. An initial displacement of 100 μm proved to reduce the scattering of the final cell position. This is likely due to the capillary forces being high at the beginning of the process, initiating the cell movement. The size of the pads made with PVD had little to no influence on the alignment accuracy. However, the copper sheet pads smaller than the cells exhibited a higher placement accuracy than the ones larger than the cells. Furthermore, a combination of a high initial displacement and a large pad lead to the cell and the pad being aligned edge-to-edge. By modelling the solder contact angle, it seems that the joint effects of these factors lead to partial wetting of the solder, hindering the process. Lastly, we demonstrated that even if the solder wettability on the pad is poor, a high cell wettability is enough to ensure solder spread and a successful self-alignment. In the end, a placement accuracy of $\pm 30 \mu\text{m}$ was reached and the in-plane rotation did not exceed $\pm 2^\circ$ for 140 cells.

In a second stage, the mechanical behaviour of the concentrator structure was assessed. This study was split in two parts: first, the bending stiffness of the structure as a function of its geometry was studied. Six different geometries were tested experimentally under a 4-point load, with the help of a design of experiments. An analytical and a FEM model of the tests were built, excluding the friction between the tool and the samples. Another FEM model including it was also developed. The friction played an important role and lead to an overestimation of the bending stiffness by up to 30%. Excluding this effect, the models and the experiments showed agreement within the range of 10% relative discrepancy. The bending stiffness target of $5 \times 10^3 \text{N.m}^{-2}$ was reached for two out of the six configurations. Regarding the stress distribution in the structure, the top CFRP layer proved to have little to no impact on the bending behaviour of the concentrator. In the end, first design guidelines were established regarding the structure geometry. Afterwards, the second part of the mechanical assessment was conducted and aimed to study the thermally-induced curvature of the concentrator. To be able to study more geometry parameters, by considering the CFRP layers separately for example, the goal was to build a FEM model and limit the number of time-consuming experiments. To do so, material characterisations were first performed to determine the coefficient of thermal expansion and curing temperature (if applicable) of the materials used. Then, experimental time-dependant deflection measurements of increasingly complex structures were performed. The results were compared to the model. Their relative discrepancy was in the range of 15% for the simpler structures (single-layer CFRP and honey-

comb) but much higher for the full concentrator. For a temperature difference of about 100°C, the experimental deflection was about twice as high than in the model. Notwithstanding, the trends given by the model were correct and allowed to define additional design guidelines. Moreover, both the experiments and the simulations demonstrated the importance of using structural adhesives able to withstand high temperature. Indeed, the epoxy used to bond the glass to the honeycomb was unable to play its role above 80°C, resulting in the glass sliding along the honeycomb. With the deflection predicted by the model and the different guidelines, we were able to select the most promising geometries for our application and determine the associated curvature expected in-flight as well as the corresponding optical losses.

Having successfully found a way to assemble the solar cells on the glass and having defined the right concentrator geometry, the next step was to manufacture and characterise the first prototypes of the concentrator. The receiving pads and the electrical tracks were screen-printed on the substrate with a silver paste. Dark I-V measurements were performed on single strings of six serially connected cells with varying track width (20, 40 and 60 μm). No clear difference was seen between the 40 and 60 μm tracks. However, the series resistance is significantly higher for the 20 μm one. At this stage, the 40 μm tracks seem to be good compromise between resistivity and shading. Outdoor I-V measurements were performed on the first and second substrate (respectively 1 cell and 30 cells). The substrates and the optics were mounted separately on a dual-axis tracker at Fraunhofer ISE. Both parts were manually aligned thanks to three micrometric stages. There was no way to control their relative rotation. Considering the light collecting area of one optic and the direct normal irradiance, a power conversion efficiency of 21% was achieved with one solar cell. Using the stages, a cell-optic alignment tolerance study was performed. In-plane, the cell can be misaligned by up to 100 μm without having the optical losses exceed 5%. However, the out-of-plane translation is more critical and 50 μm are enough to reach this loss value. It also seem that the cell is too far away from the optic even if the glass is put in contact with the honeycomb. Afterwards, indoor illuminated I-V measurements were also performed on three different substrates. The first only included one cell with a 40 μm wide track, the second one 30 cells with the same track width and the third one with 25 cells and 25 μm diameter gold wires instead of the silver tracks. Scaling the current to the same receiving area and irradiance, no current difference was observed between the three substrates. However, the second one exhibited a shunt, responsible for a V_{oc} loss of about 2 V. Finally, An optical loss analysis based on previous work highlighted that the current optical efficiency of the device is around 60%. In particular, the shading due to the interconnections, the honeycomb walls and the cell itself was theoretically and experimentally assessed and is equal to about 9%. Adding an ARC on both side of the glass, decreasing the honeycomb walls thickness, replacing the electrical tracks by wires and using a state of the art reflective coating could improve the optical efficiency up to 77%. This would greatly increase the PCE of the device with one solar cell, from 21% to about 27%. Aligning the 30 cell-substrate with the optics was exceedingly difficult without a proper mean to control the rotation. Coupled with the shunt due to a manufacture issue, an efficiency of 12% was achieved, to be significantly improved with rotation control.

Some questions remain open and some aspects could be studied in further details. Moreover, this work paved the way for future micro-concentrator developments.

(i) The electrical characterisation of the prototypes remains challenging for larger scales. The set-up should be modified to include rotation control at the very least. Even so, manually aligning the optics with the glass substrate is impractical for indoor characterisations with a flash lamp. The micrometric stages need to be adjusted one increment at a time, which combined with the charging time of the flash lamp results in an extremely time-consuming process. This could be fixed by using motorised plates and an automated set-up which would seek the higher electrical power. Although this would not require the constant presence of an operator, it does not make the process shorter. Another similar solution could use image recognition to align the cells visually. A better, different solution would be to have a frame to mechanically align both components. In a way, this is required for further developments as the optics and the substrate need to be bonded in the end. However, with the current manufacturing process, it is difficult to cut the glass or the composite structure to precise dimensions and most importantly to precisely define where the screen-printed pattern will be on the substrate. To summarise, the manufacturing process needs to be standardised in order to improve the final assembly step. Only then would the larger-scale module electrical characterisations be possible. Besides, there is no doubt that making the assembly easier and more precise would increase the concentrator PCE.

(ii) The cells interconnections were difficult to make because of the wire-bonding issues on silver. Since the technique itself is arguably too time-consuming and thus costly for the high density of cells, another method would be preferred. Recent developments indicate that screen printed interconnections with conductive ink may increase the throughput, decreasing the cost.

(iii) Concerning the tracks themselves, if screen-printed silver was satisfactory for prototypes, it can be improved. The cost itself is a concern, with silver being an expensive material. Copper would most likely be an interesting choice in that regard. Moreover, the reliability of such screen-printed paste in space conditions is questionable. As of today, no data is available to assume it fits space requirements, at least to our knowledge. Furthermore, the tracks should ideally be even thicker and narrower to decrease shading while maintaining a high electrical conductivity. The screen itself and the deposition process might be optimised to that purpose.

(iv) The thermal aspects of the design were not fully studied. The thermal deflection model proved to provide quite different results from experiments, with different possible causes. As an example, the lamination process seems poorly controlled. Due to materials unavailability and the difficulty to perform deflection measurements on large samples, the deflection model aiming to predict the bending of a realistic full-scale space concentrator structure had to rely on strong hypotheses. In particular, the thermal loading was poorly known and had to be simplified. To improve this, a complete thermal management study of the design is needed. On top of improving the deflection model, cell operating temperature is a major concern for concentration and should be studied. Then, using a realistic temperature profile, the corresponding impact on the silicone optics performances should be estimated. To try to get the

most realistic estimation of in-flight performances, a coupled simulation model including the temperature profile, structural bending and ray-tracing could be used.

(v) Concerning the optics, it would be interesting to study their behaviour as a function of the temperature, but their mass is quite high and should be decreased. Instead of moulded silicone, a thin membrane would surely increase the specific power of the design. Of course, this comes with many additional questions regarding the membrane manufacturing, costs and reliability.

(vi) Finally, self-alignment proved to be a very interesting placement and packaging solution. As mentioned before, it is of great interest to the micro-electronic field in general and the study started in this work could be continued. In particular, the cause of the edge-to-edge alignment could not be confirmed, and more experiments are needed to provide a definitive answer.

References

- [1] R. L. Freeman, *Satellite Communications*. John Wiley & Sons, Ltd, 2002.
- [2] R. L. Easton and M. J. Votaw, “Vanguard I IGY Satellite (1958 Beta),” *Review of Scientific Instruments*, vol. 30, pp. 70–75, 12 2004.
- [3] R. Ambrosi, E. J. Watkinson, A. Barco, R. Mesalam, T. Crawford, C. Bicknell, H. Williams, M.-C. Perkinson, C. Burgess, S. Gibson, C. Stroud, A. Godfrey, J. Merrifield, D. Kramer, C. Barklay, K. Stephenson, M. J. Reece, K. Simpson, R. Tuley, T. Tinsley, and M. Sarsfield, “Radioisotope power systems for the european space nuclear power program,” in *2019 IEEE Aerospace Conference*, pp. 1–10, 2019.
- [4] Jet Propulsion Laboratory (NASA), “Solar power technologies for future planetary science missions,” 2017.
- [5] M. Finckenor and K. de Groh, *Space Environmental Effects*. NASA ISS Program Science Office, 2015.
- [6] G. Halford, “Low-cycle thermal fatigue,” *NASA Technical Memorandum 87225*, 1986.
- [7] C. Qu, J. Hu, X. Liu, Z. Li, and Y. Ding, “Morphology and mechanical properties of polyimide films: The effects of uv irradiation on microscale surface,” *Materials*, vol. 10, no. 11, 2017.
- [8] J. Srour and J. Palko, “Displacement damage effects in irradiated semiconductor devices,” *IEEE Transactions on Nuclear Science*, vol. 60, pp. 1740–1766, 06 2013.
- [9] S. R. Messenger, G. P. Summers, E. A. Burke, R. J. Walters, and M. A. Xapsos, “Modeling solar cell degradation in space: A comparison of the nrl displacement damage dose and the jpl equivalent fluence approaches†,” *Progress in Photovoltaics: Research and Applications*, vol. 9, no. 2, pp. 103–121, 2001.
- [10] Y. Lu, Q. Shao, H. Yue, and F. Yang, “A review of the space environment effects on spacecraft in different orbits,” *IEEE Access*, vol. 7, pp. 93473–93488, 2019.
- [11] R. Verduci, V. Romano, G. Brunetti, N. Yaghoobi Nia, A. Di Carlo, G. D’Angelo, and C. Ciminelli, “Solar energy in space applications: Review and technology perspectives,” *Advanced Energy Materials*, vol. 12, no. 29, p. 2200125, 2022.
- [12] T. G. Roberts, “Space launch to low earth orbit: How much does it cost?.” <https://aerospace.csis.org/data/space-launch-to-low-earth-orbit-how-much-does-it-cost/>, 2022. Accessed: 2023-06-13.
- [13] G. Haynes, “Effect of radiation on cerium-doped solar-cell cover glass,” *NASA Technical Note D-6024*, p. 13, 1970.
- [14] R. Francis, C. Sve, and T. Wall, “Thermal cycling techniques for solar panels,” *Crosslink*, vol. 6, no. 3, Fall 2005.
- [15] AZUR SPACE Solar Power GmbH, “TJ Solar Cell 3G30C - Advanced (80µm) datasheet.” <http://www.azurspace.com/index.php/en/products/products-space/space-solar-cells>.
- [16] E. M. Gaddy, “Cost trade between multijunction, gallium arsenide and silicon solar cells,” *Progress in Photovoltaics: Research and Applications*, vol. 4, no. 2, pp. 155–161, 1996.
- [17] M. Reddy, “Space solar cells—tradeoff analysis,” *Solar Energy Materials and Solar Cells*, vol. 77, no. 2, pp. 175–208, 2003.
- [18] J.-F. Guillemoles, T. Kirchartz, D. Cahen, and U. Rau, “Guide for the perplexed to the shockley–queisser model for solar cells,” *Nature Photonics*, vol. 13, p. 501–505, 2019.
- [19] I. M. Peters, C. D. Rodríguez Gallegos, L. Lüer, J. A. Hauch, and C. J. Brabec, “Practical limits of multijunction solar cells,” *Progress in Photovoltaics: Research and Applications*, vol. n/a, no. n/a, pp. 1–10, 2023.

References

- [20] “IEC 62108:2022: Concentrator photovoltaic (CPV) modules and assemblies - Design qualification and type approval,” 2022.
- [21] American Society for Testing and Materials International, “ASTM G173-03,” 2020.
- [22] American Society for Testing and Materials International, “Standard Solar Constant and Zero Air Mass Solar Spectral Irradiance Tables, ASTM E490-00a,” 2019.
- [23] H. Curtis, M. Piszczor, P. Severance, D. Guidice, and D. Olson, “Early results from the PASP Plus flight experiment,” in *Proceedings of 1994 IEEE 1st World Conference on Photovoltaic Energy Conversion - WCPEC (A Joint Conference of PVSC, PVSEC and PSEC)*, vol. 2, (Waikoloa, HI, USA), pp. 2169–2172, IEEE, 1994.
- [24] H. Curtis and D. Marvin, “Final results from the PASP plus flight experiment,” in *Conference Record of the Twenty Fifth IEEE Photovoltaic Specialists Conference - 1996*, pp. 195–198, 1996.
- [25] M. P. Lumb, B. Fisher, K. J. Schmieder, and M. Meitl, “Six-junction (6J) microscale concentrating photovoltaics (CPV) for space applications,” in *2016 IEEE 43rd Photovoltaic Specialists Conference (PVSC)*, pp. 3415–3420, 2016.
- [26] M. Wiesenfarth, D. Iankov, J. F. Martínez, P. Nitz, M. Steiner, F. Dimroth, and H. Helmers, “Technical boundaries of micro-CPV module components: How small is enough?,” *AIP Conference Proceedings*, vol. 2550, 09 2022. 030008.
- [27] C. Domínguez, N. Jost, S. Askins, M. Victoria, and I. Antón, “A review of the promises and challenges of micro-concentrator photovoltaics,” *AIP Conference Proceedings*, vol. 1881, 09 2017. 080003.
- [28] A. Ritou, P. Voarino, and O. Raccurt, “Does micro-scaling of CPV modules improve efficiency? A cell-to-module performance analysis,” *Solar Energy*, vol. 173, pp. 789–803, Oct. 2018.
- [29] A. Bermudez-Garcia, P. Voarino, and O. Raccurt, “Environments, needs and opportunities for future space photovoltaic power generation: A review,” *Applied Energy*, vol. 290, p. 116757, 2021.
- [30] M. Piszczor, C. Swartz, M. O’Neill, A. McDanal, and L. Fraas, “The mini-dome fresnel lens photovoltaic concentrator array: current status of components and prototype panel testing,” in *IEEE Conference on Photovoltaic Specialists*, pp. 1271–1276 vol.2, 1990.
- [31] S. S. Gates, S. M. Koss, and M. F. Zedd, “Advanced tether experiment deployment failure,” *Journal of Spacecraft and Rockets*, vol. 38, no. 1, pp. 60–68, 2001.
- [32] D. Murphy and D. Allen, “SCARLET development, fabrication, and testing for the Deep Space 1 spacecraft,” in *IECEC-97 Proceedings of the Thirty-Second Intersociety Energy Conversion Engineering Conference (Cat. No.97CH6203)*, vol. 4, (Honolulu, HI, USA), pp. 2237–2245, IEEE, 1997.
- [33] J. J. Wachholz and D. M. Murphy, “SCARLET I: Mechanization solutions for deployable concentrator optics integrated with rigid array technology,” 5 1996.
- [34] M. O’Neil, “Stretched Fresnel lens solar concentrator for space power,” 2000. US Patent 6,075,200.
- [35] H. Brandhorst, J. Rodiek, and M. O’Neill, “The stretched lens array’s testing and mission success in harsh environments,” *European Space Agency, (Special Publication) ESA SP*, 01 2008.
- [36] P. Jenkins, D. Bentz, J. Barnds, C. Binz, S. Messenger, J. Warner, M. Krasowski, N. Prokop, D. Spina, M. O’Neill, M. Eskenazi, H. Brandhorst, E. Downard, and K. Crist, “Initials results from the tacsat-4 solar cell experiment,” in *2013 IEEE 39th Photovoltaic Specialists Conference (PVSC)*, (Tampa, FL, USA), pp. 3108–3111, 2013.
- [37] M. O’Neill, A. McDanal, H. Brandhorst, K. Schmid, P. LaCorte, M. Piszczor, and M. Myers, “Recent space pv concentrator advances: More robust, lighter, and easier to track,” in *2015 IEEE 42nd Photovoltaic Specialist Conference (PVSC)*, pp. 1–6, 2015.
- [38] SpaceTech GmbH, “Spacetechn solar arrays product information.” <https://www.spacetechn-i.com/products/solar-arrays>.
- [39] B. Spence and M. Eskenazi, “The cellsaver concentrator solar array system and qualification program,” *Space Power, Proceedings of the Sixth European Conference held 6-10 May, 2002 in Porto, Portugal. Edited by A. Wilson. European Space Agency, ESA SP-502*, p. 451, 2002.

- [40] R. Jain, Y. N. Wong, J. Kesapradist, G. van Ommering, and M. Eskenazi, "New concentrator technology experiment on a geosynchronous satellite," in *3rd World Conference on Photovoltaic Energy Conversion, 2003. Proceedings of*, vol. 1, pp. 865–868 Vol.1, 2003.
- [41] M. Eskenazi, "Design, analysis & testing of the CellSaver concentrator for spacecraft solar arrays," in *Conference Record of the Twenty-Ninth IEEE Photovoltaic Specialists Conference, 2002.*, (New Orleans, LA, USA), pp. 935–938, IEEE, 2002.
- [42] M. Eskenazi, A. Jones, R. Jain, B. Hoang, K. MacDonald, Y. N. Wong, J. Kesapradist, and G. van Ommering, "Preliminary test results for the cellsaver concentrator in geosynchronous earth orbit," in *Conference Record of the Thirty-first IEEE Photovoltaic Specialists Conference, 2005.*, pp. 622–625, 2005.
- [43] A. Bermudez-Garcia, P. Voarino, and O. Raccurt, "Micro-concentrateur à structure alvéolaire," 21/12/2020. French Patent FR2013856.
- [44] C. Domínguez, M. Victoria, R. Herrero, S. Askins, I. Antón, and G. Sala, "Probing the effects of non-uniform light beams and chromatic aberration on the performance of concentrators using multijunction cells," *AIP Conference Proceedings*, vol. 1477, pp. 127–130, 10 2012.
- [45] R. Herrero, M. Victoria, C. Domínguez, S. Askins, I. Antón, and G. Sala, "Understanding causes and effects of non-uniform light distributions on multi-junction solar cells: Procedures for estimating efficiency losses," *AIP Conference Proceedings*, vol. 1679, 09 2015. 050006.
- [46] A. Ritou, P. Voarino, B. Goubault, N. David, S. Bernardis, O. Raccurt, and M. Baudrit, "Mechanical tolerances study through simulations and experimental characterization for a 1000X micro-concentrator CPV module," in *13th International Conference On Concentrator Photovoltaic Systems (CPV-13)*, (Ottawa, Canada), p. 030007, 2017.
- [47] S. Askins and G. S. Pano, *CPV Modules*, ch. 7. John Wiley & Sons, Ltd, 2016.
- [48] Y. D. Zonou, S. Bernabe, D. Fowler, M. Francou, O. Castany, and P. Arguel, "Self-Alignment with Copper Pillars Micro-Bumps for Positioning Optical Devices at Submicronic Accuracy," in *2017 IEEE 67th Electronic Components and Technology Conference (ECTC)*, (Orlando, FL, USA), pp. 557–562, IEEE, May 2017.
- [49] H. Arase, A. Matsushita, A. Itou, T. Asano, N. Hayashi, D. Inoue, R. Futakuchi, K. Inoue, T. Nakagawa, M. Yamamoto, E. Fujii, Y. Anda, H. Ishida, T. Ueda, O. Fidaner, M. Wiemer, and D. Ueda, "A novel thin concentrator photovoltaic with microsolar cells directly attached to a lens array," *IEEE Journal of Photovoltaics*, vol. 4, no. 2, pp. 709–712, 2014.
- [50] N. Hayashi, M. Terauchi, Y. Aya, S. Kanayama, H. Nishitani, and M. Nakagawa, T.and Takase, "Thin concentrator photovoltaic module with micro-solar cells which are mounted by self-align method using surface tension of melted solder," in *13th International Conference On Concentrator Photovoltaic Systems (CPV-13)*, (Ottawa, Canada), p. 080005, 2017.
- [51] E. Ebraert, F. Gao, S. Beri, J. Watté, H. Thienpont, and J. Van Erps, "Design and prototyping of self-centering optical single-mode fiber alignment structures," *Journal of Micromechanics and Microengineering*, vol. 26, p. 065007, June 2016.
- [52] T. Gu, D. Li, L. Li, B. Jared, G. Keeler, B. Miller, W. Sweatt, S. Paap, M. Saavedra, U. Das, S. Hegedus, A. Tauke-Pedretti, and J. Hu, "Wafer integrated micro-scale concentrating photovoltaics," in *13th International Conference On Concentrator Photovoltaic Systems (CPV-13)*, (Ottawa, Canada), p. 080004, 2017.
- [53] S. Cho, W. Choi, S. Han, J. Kim, A. C. Lee, S. D. Kim, S. W. Song, C. Kim, D. Lee, and S. Kwon, "Micro-concentrator photovoltaics using fluidic self-assembly technology," *Advanced Materials Technologies*, vol. 6, no. 12, p. 2100312, 2021.
- [54] E. Virey and Z. Bouhamri, "Microled displays - market, industry and technology trends 2021," 2020.
- [55] S. B. Shetye, *Magnetic self-assembly of small parts*. PhD thesis, University of Florida, 2009.
- [56] Y. Suzuki, A.and Wakazono, D. Nagao, T. Ishikawa, T. Hino, Y. Hashimoto, H. Masuda, S. Suzuki, M. Tamura, T.-I. Suzuki, K. Kikuchi, H. Nakagawa, Y. Okada, M. Aoyagi, and T. Mikawa, "Self-Alignment of Optical Devices With Fiber for Low-Cost Optical Interconnect Modules," *IEEE Photonics Technology Letters*, vol. 20, pp. 193–195, Feb. 2008.

References

- [57] D. Hegemann, H. Brunner, and C. Oehr, "Plasma treatment of polymers for surface and adhesion improvement," *Nuclear Instruments and Methods in Physics Research Section B: Beam Interactions with Materials and Atoms*, vol. 208, pp. 281–286, Aug. 2003.
- [58] L. Sanchez, L. Bally, B. Montmayeul, F. Fournel, J. Dafonseca, E. Augendre, L. Di Cioccio, V. Carron, T. Signamarcheix, R. Taibi, S. Mermoz, and G. Lecarpentier, "Chip to wafer direct bonding technologies for high density 3D integration," in *2012 IEEE 62nd Electronic Components and Technology Conference*, (San Diego, CA, USA), pp. 1960–1964, IEEE, May 2012.
- [59] S. Mermoz, L. Sanchez, L. Di Cioccio, J. Berthier, E. Deloffre, and C. Fretigny, "Impact of containment and deposition method on sub-micron chip-to-wafer self-assembly yield," in *2011 IEEE International 3D Systems Integration Conference (3DIC), 2011 IEEE International*, (Osaka), pp. 1–5, IEEE, Jan. 2012.
- [60] S. Mermoz, L. Sanchez, L. Di Cioccio, J. Berthier, E. Deloffre, P. Coudrain, and C. Fretigny, "High density chip-to-wafer integration using self-assembly: On the performances of directly interconnected structures made by direct copper/oxyde bonding," in *2013 IEEE 15th Electronics Packaging Technology Conference (EPTC 2013)*, (Singapore), pp. 162–167, IEEE, Dec. 2013.
- [61] L. Sun, M.-H. Chen, C.-C. Wei, L. Zhang, and F. Yang, "Effect of thermal cycles on interface and mechanical property of low-Ag Sn1.0Ag0.5Cu(nano-Al)/Cu solder joints," *Journal of Materials Science: Materials in Electronics*, vol. 29, pp. 9757–9763, June 2018.
- [62] Y. Liu and K. Tu, "Low melting point solders based on Sn, Bi, and In elements," *Materials Today Advances*, vol. 8, p. 100115, Dec. 2020.
- [63] The European Parliament and the Council of the European Union, "Directive 2011/65/EU of the European Parliament and of the Council of 8 June 2011 on the restriction of the use of certain hazardous substances in electrical and electronic equipment (recast)." <https://eur-lex.europa.eu/legal-content/EN/TXT/?uri=CELEX:32011L0065>, 2011. Accessed: 2023-05-23.
- [64] Jemin K., Yunseong J., and Kwanhun L., "Comparison with reliability of low Ag solder ball by thermal shock and cycling tests," in *2016 6th Electronic System-Integration Technology Conference (ESTC)*, (Grenoble, France), pp. 1–4, IEEE, Sept. 2016.
- [65] H. Kang, S. H. Rajendran, and J. P. Jung, "Low Melting Temperature Sn-Bi Solder: Effect of Alloying and Nanoparticle Addition on the Microstructural, Thermal, Interfacial Bonding, and Mechanical Characteristics," *Metals*, vol. 11, p. 364, Feb. 2021.
- [66] D. Abdul Ameer Shnawah, M. Faizul Bin Mohd Sabri, I. Anjum Badruddin, and S. Said, "A review on effect of minor alloying elements on thermal cycling and drop impact reliability of low-Ag Sn-Ag-Cu solder joints," *Microelectronics International*, vol. 29, pp. 47–57, Jan. 2012.
- [67] X. Li and Z. Wang, "Thermo-fatigue life evaluation of SnAgCu solder joints in flip chip assemblies," *Journal of Materials Processing Technology*, vol. 183, pp. 6–12, Mar. 2007.
- [68] A. Jouve, L. Sanchez, C. Castan, M. Laugier, E. Rolland, B. Montmayeul, R. Franiatte, F. Fournel, and S. Cheramy, "Self-Assembly Process for 3D Die-to-Wafer using Direct Bonding: A Step Forward Toward Process Automatisation," in *2019 IEEE 69th Electronic Components and Technology Conference (ECTC)*, (Las Vegas, NV, USA), pp. 225–234, IEEE, May 2019.
- [69] M. Mastrangeli, Q. Zhou, V. Sariola, and P. Lambert, "Surface tension-driven self-alignment," *Soft Matter*, vol. 13, no. 2, pp. 304–327, 2017.
- [70] K. Sato, K. Ito, S. Hata, and A. Shimokohbe, "Self-alignment of microparts using liquid surface tension—behavior of micropart and alignment characteristics," *Precision Engineering*, vol. 27, pp. 42–50, Jan. 2003.
- [71] I. Routa, Bo Chang, A. Shah, and Quan Zhou, "Surface Tension-Driven Self-Alignment of Microchips on Low-Precision Receptors," *Journal of Microelectromechanical Systems*, vol. 23, pp. 819–828, Aug. 2014.
- [72] C. Palacio, H. Mathieu, and D. Landolt, "AES, XPS and EELS study of the initial oxidation of polycrystalline chromium," *Surface Science*, vol. 182, no. 1, pp. 41–55, 1987.
- [73] T. Campbell, R. K. Kalia, A. Nakano, P. Vashishta, S. Ogata, and S. Rodgers, "Dynamics of oxidation of aluminum nanoclusters using variable charge molecular-dynamics simulations on parallel computers," *Phys. Rev. Lett.*, vol. 82, pp. 4866–4869, Jun 1999.

- [74] A. Shah, B. Chang, S. Suihkonen, Q. Zhou, and H. Lipsanen, "Surface-Tension-Driven Self-Alignment of Microchips on Black-Silicon-Based Hybrid Template in Ambient Air," *Journal of Microelectromechanical Systems*, vol. 22, pp. 739–746, June 2013.
- [75] A. B. D. Cassie and S. Baxter, "Wettability of porous surfaces," *Trans. Faraday Soc.*, vol. 40, pp. 546–551, 1944.
- [76] T. Koishi, K. Yasuoka, S. Fujikawa, and X. C. Zeng, "Measurement of Contact-Angle Hysteresis for Droplets on Nanopillared Surface and in the Cassie and Wenzel States: A Molecular Dynamics Simulation Study," *ACS Nano*, vol. 5, pp. 6834–6842, Sept. 2011.
- [77] H. L. Skriver and N. M. Rosengaard, "Surface energy and work function of elemental metals," *Physical Review B*, vol. 46, pp. 7157–7168, Sept. 1992.
- [78] L. Vitos, A. Ruban, H. Skriver, and J. Kollár, "The surface energy of metals," *Surface Science*, vol. 411, pp. 186–202, Aug. 1998.
- [79] Z. Moser, W. Gasior, J. Pstrus, and A. Debski, "Wettability studies of pb-free soldering materials," *International Journal of Thermophysics*, vol. 29, pp. 1974–1986, 12 2008.
- [80] J. Abbott and B. Higgins, "Surface tension of a curing epoxy," *Journal of Polymer Science Polymer Chemistry Edition*, vol. 26, p. 1985, 07 1988.
- [81] A. Yakymovych, H. Weber, I. Kaban, and H. Ipser, "Dynamic viscosity of a liquid sn-3.0ag-0.5cu alloy with ni nanoparticles," *Journal of Molecular Liquids*, vol. 268, pp. 176–180, 2018.
- [82] R. Kohli, "Chapter 2 - UV-Ozone Cleaning for Removal of Surface Contaminants," in *Developments in Surface Contamination and Cleaning* (R. Kohli and K. L. Mittal, eds.), pp. 71–104, Oxford: William Andrew Publishing, 2015.
- [83] H. Y. Peng, M. Devarajan, and T. T. Lee, "Comparison of argon and oxygen plasma treatments on led chip bond pad for wire bond application," *International Journal of Scientific & Engineering Research*, vol. 5, p. 5, 2014.
- [84] Z. Zhai and L. Feng, "Effect of oxygen plasma treatment on bonding strength of epoxy coating on steel substrate," *Progress in Organic Coatings*, vol. 131, pp. 36–41, June 2019.
- [85] D. Berman and J. Krim, "Impact of oxygen and argon plasma exposure on the roughness of gold film surfaces," *Thin Solid Films*, vol. 520, pp. 6201–6206, July 2012.
- [86] E. Carrasco, O. de la Fuente, J. Rojo, M. Garcia, and C. de Julian, "Defects study in gold surfaces produced by ion bombardment," *MRS Proceedings*, vol. 40, p. 546, 2006.
- [87] J.-M. Kim, K. Yasuda, K. Fujimoto, and S. Nakata, "Highly Precise Positioning Method by Pull-Up Model Self-Alignment Process Using Liquid Surface Tension.," *Quarterly Journal of the Japan Welding Society*, vol. 20, no. 3, pp. 346–354, 2002.
- [88] C. A. Bower, E. Menard, and P. E. Garrou, "Transfer printing: An approach for massively parallel assembly of microscale devices," in *2008 58th Electronic Components and Technology Conference*, (Lake Buena Vista, FL, USA), pp. 1105–1109, IEEE, May 2008.
- [89] B. Furman, E. Menard, A. Gray, M. Meitl, S. Bonafede, D. Kneeburg, K. Ghosal, R. Bukovnik, W. Wagner, J. Gabriel, S. Seel, and S. Burroughs, "A high concentration photovoltaic module utilizing micro-transfer printing and surface mount technology," in *2010 35th IEEE Photovoltaic Specialists Conference*, (Honolulu, HI, USA), pp. 000475–000480, IEEE, June 2010.
- [90] Koki Company Ltd., "Powerful Wetting Lead Free Solder Paste S3X48-M500C-5," 2013.
- [91] Koki Company Ltd., "Solder paste for wafer bumping S3X-BF70M," 2010.
- [92] Besi Semiconductor Industries N.V., "Datacon 2200 evo advanced." <https://www.besi.com/products-technology/product-details/product/datacon-2200-evo/>. Accessed: 2023-05-23.
- [93] K. Brakke, "The surface evolver version 2.70." <https://facstaff.susqu.edu/brakke/evolver/evolver.html>, 2013. Accessed: 2023-05-23.
- [94] M. F. Arenas and V. L. Acoff, "Contact angle measurements of Sn-Ag and Sn-Cu lead-free solders on copper substrates," *Journal of Electronic Materials*, vol. 33, pp. 1452–1458, Dec. 2004.

References

- [95] H. Takao and H. Hasegawa, "Effect of Au Coating on the Wettability of Cu Substrate by Sn-Ag Eutectic Solder," *Journal of the Japan Institute of Metals*, vol. 63, no. 5, pp. 565–568, 1999.
- [96] N. B. Duong, T. Ariga, L. B. Hussain, and A. B. Ismail, "Wettability of Lead-Free Solders on Gold-Plated Copper Substrates," *MATERIALS TRANSACTIONS*, vol. 49, no. 6, pp. 1462–1466, 2008.
- [97] L. Zhang, C.-w. He, Y.-h. Guo, J.-g. Han, Y.-w. Zhang, and X.-y. Wang, "Development of SnAg-based lead free solders in electronics packaging," *Microelectronics Reliability*, vol. 52, pp. 559–578, Mar. 2012.
- [98] N. Rodrigues, A. C. Ferreira, S. F. Teixeira, D. Soares, J. C. Teixeira, F. Cerqueira, and F. Macedo, "Contact angle measurement of SAC 305 solder: numerical and experimental approach," *Journal of Materials Science: Materials in Electronics*, vol. 27, pp. 8941–8950, Sept. 2016.
- [99] V. Vareilles, E. Kaiser, P. Voarino, M. Wiesenfarth, R. Cariou, F. Dimroth, Y. Veschetti, M. Amara, and H. Helmers, "Experimental and simulative correlations of the influence of solder volume and receptor size on the capillary self-alignment of micro solar cells," *Accepted in the IEEE Journal of Microelectromechanical systems*, 2024.
- [100] E. Kaiser, M. Wiesenfarth, V. Vareilles, M. Schneider-Ramelow, S. Glunz, and H. Helmers, "Forced motion activated self-alignment of micro-cpv solar cells," *Submitted to the IEEE Journal of Photovoltaics*, 2023.
- [101] H. Kim and C. Han, "Analytical and numerical approaches of a solar array thermal analysis in a low-earth orbit satellite," *Advances in Space Research*, vol. 46, pp. 1427–1439, 2010.
- [102] Y. Kim, M. Kim, P. Kim, H. Kim, J. Park, J. Roh, and J. Bae, "Optimal design of a high-agility satellite with composite solar panels," *International Journal of Aeronautical and Space Sciences*, vol. 17, no. Issue 4, pp. 476–490, 2016.
- [103] J. Li and S. Yan, "Thermally induced vibration of composite solar array with honeycomb panels in low earth orbit," *Applied Thermal Engineering*, vol. 71, no. Issue 1, pp. 419–432, 2014.
- [104] "NF T54-606. Structures sandwich à base de plastiques - Essai de flexion," Octobre 1987.
- [105] H. G. Allen, *Analysis and Design of Structural Sandwich Panels*. The Commonwealth and International Library, Oxford: Pergamon Pr, 1. ed ed., 1969.
- [106] H. Allen, "Analysis of sandwich panels: The significance of shear deformation," *Composites*, vol. 1, pp. 215–220, June 1970.
- [107] D. Chen and S. Ozaki, "Analysis of in-plane elastic modulus for a hexagonal honeycomb core: Effect of core height and proposed analytical method," *Composite Structures*, vol. 88, pp. 17–25, Mar. 2009.
- [108] C. Semprimoschnig, D. Pueyo, J. Williamson, C. Mooney, C. Zimmermann, M. Eesbeek, and S. Taylor, "Elastosil s 690 - a space qualified european silicone material," 2009.
- [109] "ASTM D 1894 Standard Test Method for Static and Kinetic Coefficients of Friction of Plastic Film and Sheeting," 2001.
- [110] JMP, "Jmp statistical discovery." https://www.jmp.com/fr_fr/home.html. Accessed: 2023-05-31.
- [111] "ASTM D7250 / D7250M-20, Determining Sandwich Beam Flexural and Shear Stiffness, ASTM International, West Conshohocken, PA, 2020, www.astm.org."
- [112] "ASTM D7249 / D7249M-20, Standard Test Method for Facesheet Properties of Sandwich Constructions by Long Beam Flexure, ASTM International, West Conshohocken, PA, 2020, www.astm.org."
- [113] V. Vareilles, A. Bermudez-Garcia, F. Chabuel, M. Amara, Y. Veschetti, and P. Voarino, "Influence of the thermally induced deflection of a space micro-concentrator photovoltaic array on its optical performances using finite element method," *AIP Conference Proceedings*, vol. 2841, no. 1, p. 030005, 2023.
- [114] D. Y. Liu, "Thermal stress analysis of a trilayer film/substrate system with weak interfaces," *Composites Part B: Engineering*, vol. 43, no. Issue 8, pp. 3445–3452, 2012.
- [115] J. Malzbender, "Stress profile and thermal expansion of layered materials determined from surface stresses," *Applied Physics Letters*, vol. 84, pp. 4661–4662, June 2004.
- [116] H. Torun and H. Urey, "Thermal deflections in multilayer microstructures and athermalization," *Journal of Applied Physics*, vol. 100, p. 023527, July 2006.

-
- [117] C. H. Hsueh, "Modeling of elastic deformation of multilayers due to residual stresses and external bending," *Journal of Applied Physics*, vol. 91, no. 12, p. 9652, 2002.
- [118] R. J. Roark, W. C. Young, R. G. Budynas, and A. M. Sadegh, *Roark's Formulas for Stress and Strain*. McGraw-Hill, 2012.
- [119] Euralliage, "5052 (aw-almg2,5)." <https://www.euralliage.com/5052.htm>, 2013. Accessed: 2023-05-31.
- [120] Toray Composite Materials America, Inc., "M55J High Modulus Carbon Fiber," 2020.
- [121] Y. Nawab, F. Jacquemin, P. Casari, N. Boyard, Y. Borjon-Piron, and V. Sobotka, "Study of variation of thermal expansion coefficients in carbon/epoxy laminated composite plates," *Composites Part B: Engineering*, vol. 50, pp. 144–149, 2013.
- [122] R. Johnson, M. Kural, and G. Macke, "Thermal expansion properties of composites materials," *NASA Contractor Report 165632*, 1981.
- [123] Exelitas Technologies Corp., "Qioptiq Space-Qualified Cover Glass Datasheet." <https://www.excelitas.com/product/space-qualified-cover-glass>, 2023. Accessed: 2023-08-28.
- [124] Corning Incorporated, "Eagle XG Product Information Sheet." <https://www.corning.com/emea/en/products/display-glass/products/eagle-xg-slim.html>, 2019. Accessed: 2023-08-28.
- [125] M.-H. Tan and K.-K. Chong, "Rectifying structural deflection effect of large solar concentrator via correction of sun-tracking angle in the concentrator photovoltaic system," *Solar Energy*, vol. 148, pp. 140–148, May 2017.
- [126] A. Bermudez-Garcia, *Micro-concentrateur ultra-intégré pour les applications spatiales*. PhD thesis, Université Grenoble Alpes, Grenoble, 2022.
- [127] A. Bermudez-Garcia, P. Voarino, and O. Raccurt, "Optical design and optics manufacturing of a highly integrated micro-cpv for space applications," in *Proceedings of the 8th World Conference on Photovoltaic Energy Conversion*, pp. 1142 – 1147, 2022.
- [128] M. Brogren, A. Helgesson, B. Karlsson, J. Nilsson, and A. Roos, "Optical properties, durability, and system aspects of a new aluminium-polymer-laminated steel reflector for solar concentrators," *Solar Energy Materials and Solar Cells*, vol. 82, no. 3, pp. 387–412, 2004.
- [129] C. Kennedy, R. Smilgys, D. Kirkpatrick, and J. Ross, "Optical performance and durability of solar reflectors protected by an alumina coating," *Thin Solid Films*, vol. 304, pp. 303–309, 1997.
- [130] M. DiGrazia and G. Jorgensen, "Reflectech mirror film: Design flexibility and durability in reflecting solar applications," *American Energy Society*, vol. 100, 2010.
- [131] Jet Propulsion Laboratory, "Deep space 1: Advanced technologies: Solar concentrator arrays." <https://www.jpl.nasa.gov/nmp/ds1/tech/scarlet.html>. Accessed: 2023-08-23.
- [132] E. Kaiser, M. Wiesenfarth, V. Vareilles, and H. Helmers, "Impact of pad layouts and solder volume on self-alignment of micro solar cells," in *Submitted to the European Microelectronic Packaging Conference*, (Cambridge, United Kingdom), 2023.
- [133] V. Vareilles, J.-B. Charpentier, P. Voarino, Y. Veschetti, and M. Amara, "Determination of the bending stiffness of a novel highly integrated microconcentrator design for space applications," *IEEE Journal of Photovoltaics*, vol. 12, no. 6, pp. 1495–1502, 2022.
- [134] V. Vareilles, P. Voarino, Y. Veschetti, E. Kaiser, H. Helmers, and M. Amara, "Manufacturing of a novel micro-concentrator prototype and assessment of its electrical performances," in *13th European Space Power Conference (ESPC)*, (Elche, Spain), 2023.

Appendices

A In-plane capillary forces analytical model

A scheme of the capillary self-alignment process is presented in Fig. A.1. The cell of length C_L rests on the solder layer of thickness h and surface tension γ . The solder droplet is confined on the pad of length P_L . Both the cell and the pad have a width W . The length difference between the cell and the pad is noted ΔL .

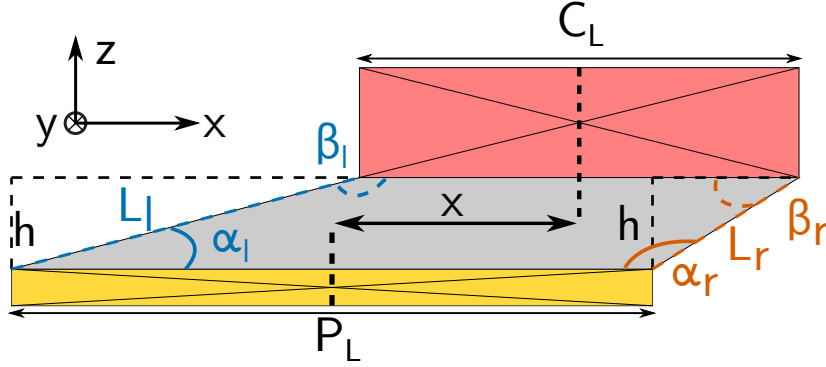


Figure A.1: Scheme of the problem.

One can express the length L_r as a function of the displacement x of the cell:

$$L_r(x) = \sqrt{\left(x - \frac{\Delta L}{2}\right)^2 + h^2}$$

And the length L_l as:

$$L_l(x) = \sqrt{\left(x + \frac{\Delta L}{2}\right)^2 + h^2}$$

The energy of a side i can be expressed as the product of the solder surface tension by the corresponding surface:

$$E_i(x) = \gamma \times W \times L_i(x)$$

On a side i , the capillary force F_i can be expressed as:

$$F_i(x) = \frac{-dE_i(x)}{dx}$$

$$F_l(x) = -\gamma \times W \times \frac{x - \frac{\Delta L}{2}}{\sqrt{\left(x - \frac{\Delta L}{2}\right)^2 + h^2}}$$

$$F_r(x) = -\gamma \times W \times \frac{x + \frac{\Delta L}{2}}{\sqrt{(x + \frac{\Delta L}{2})^2 + h^2}}$$

Considering the total capillary force F_t :

$$F_t(x) = -\gamma \times W \times \left(\frac{x + \frac{\Delta L}{2}}{\sqrt{(x + \frac{\Delta L}{2})^2 + h^2}} + \frac{x - \frac{\Delta L}{2}}{\sqrt{(x - \frac{\Delta L}{2})^2 + h^2}} \right)$$

It is then possible to calculate α_i , respectively β_i , the solder angle on the pad, respectively the cell on a side i .

On the right side:

$$\tan(\alpha_r - \frac{\pi}{2}) = \frac{x - \frac{\Delta L}{2}}{h}$$

$$\beta_r = \pi - \alpha_r$$

On the left side:

$$\cos(\alpha_l) = \frac{x + \frac{\Delta L}{2}}{\sqrt{h^2 + (x + \frac{\Delta L}{2})^2}}$$

$$\beta_l = \pi - \alpha_l$$

The surface S of the solder layer in the Oxy plane is:

$$S = \frac{V}{W}$$

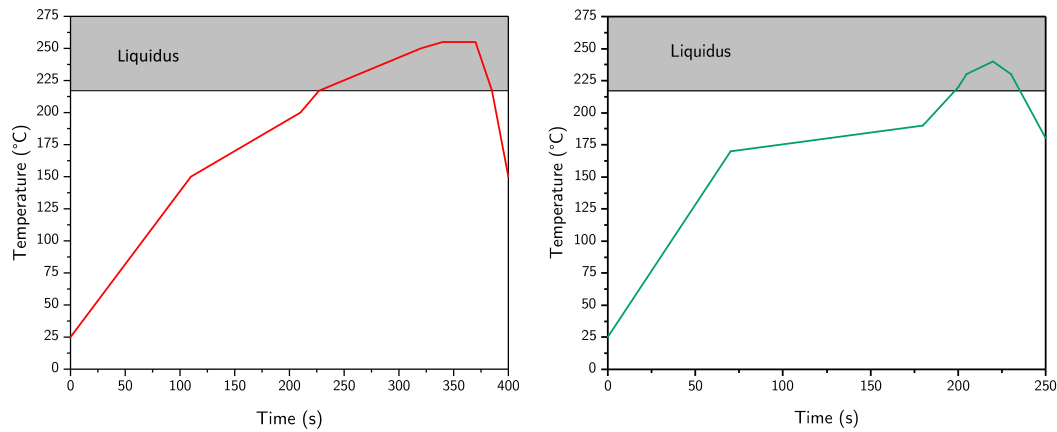
And since the solder layer is a trapezoid:

$$\frac{V}{W} = \frac{h(P_L + C_L)}{2}$$

$$h = \frac{2V}{W(P_L + C_L)}$$

B Micro-solar cells reflow processes

The temperature as a function of the time during the reflow processes used at Leti and ISE are displayed in Fig. B.1(a), respectively Fig. B.1(b).



(a) Temperature profile at Leti used in the self-alignment experiments.

(b) Temperature profile at ISE used to manufacture the prototype.

Figure B.1: Temperature profiles during the micro-solar cells reflow processes.

C Comparison between the two screens used to manufacture the prototypes front glasses

The measured lines and pads dimensions for the two screens are shown in Table C.1 and Table C.2. The mean value and the standard deviation is given. No significant difference in pattern size was observed after characterisation.

Screen	Line opening (μm)	Measured line width (μm)
1	20	56 ± 5
	40	64 ± 6
	60	88 ± 4
2	20	45 ± 8
	40	67 ± 7
	60	92 ± 5

Table C.1: Line openings and actual printed line dimensions for the two screens.

Screen	Receiving pad		Welding pad	
	Length (μm)	Width (μm)	Length (μm)	Width (μm)
1	894 ± 3	698 ± 6	746 ± 8	238 ± 5
2	903 ± 9	695 ± 3	754 ± 14	235 ± 3

Table C.2: Receiving and welding pad dimensions for the two screens.

Figure C.1 shows a microscope picture of a pad for the two screens. Qualitatively speaking, the second one gives better edge definition and was chosen over the first one.

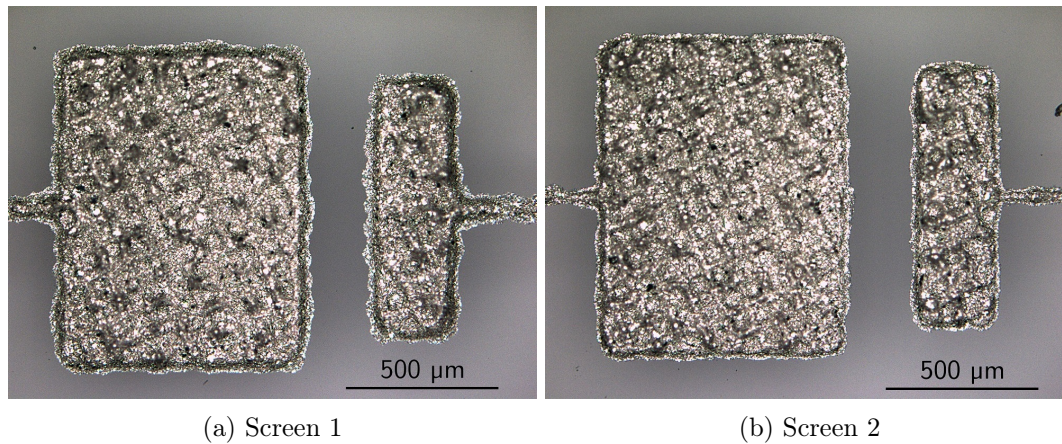


Figure C.1: Pad shape comparison for the two screens.

D Prototype micro-solar cells placement accuracy

The placement accuracy of the micro-solar cells soldered to make the prototypes is shown in Fig. D.1. The in-plane displacement and rotation is given for the pads (crossed boxes) and the cells (boxes without patterns). The position of the design B cell was not measured because it will be aligned in the measurements anyway. Therefore its placement accuracy only affects the shading slightly. The pad position accuracy is rather good, with $\pm 20 \mu\text{m}$ difference from the design. This tolerance affect the cells position: in the end, the cells are positioned with an accuracy of at least $35 \mu\text{m}$ for the in-plane translation. Concerning the in-plane rotation, the cells show a maximum angle of 1.5° . The pads appear more tilted, with an angle reaching 5° . This may be due to a poor recognition of the edges during the characterisation process.

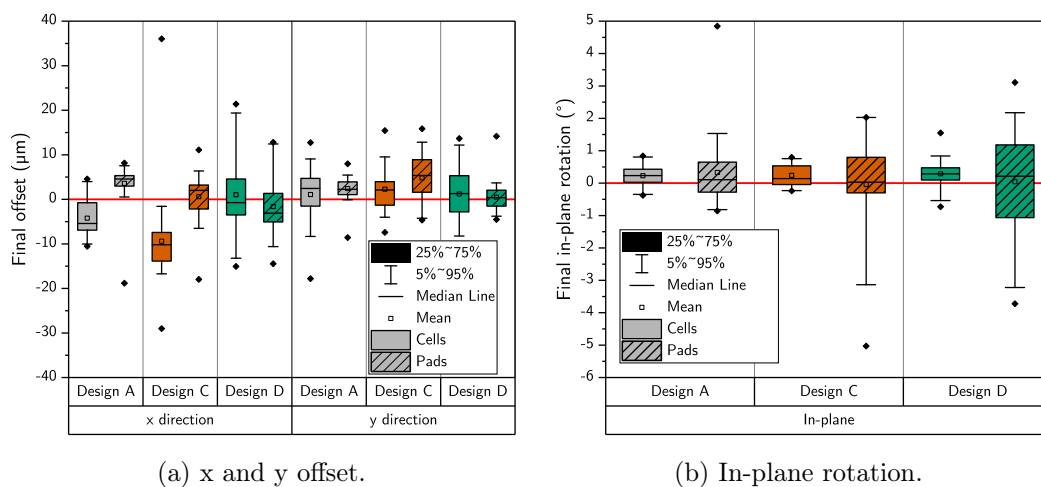


Figure D.1: Final positioning of the cells for the different designs.

E List of scientific contributions

- V. Vareilles, A. Bermudez-Garcia, J. Francois, Y. Veschetti, M. Amara, P. Voarino, and F. Chabuel, "First mechanical study on a lightweight micro-concentrator design for space applications", in *38th European Photovoltaic Solar Energy Conference and Exhibition (EUPVSEC)*, pp. 1101–1105, 2021.
- V. Vareilles, J.-B. Charpentier, P. Voarino, Y. Veschetti, and M. Amara, "Determination of the bending stiffness of a novel highly integrated microconcentrator design for space applications", *IEEE Journal of Photovoltaics*, vol. 12, no. 6, pp. 1495–1502, 2022.
- V. Vareilles, E. Kaiser, P. Voarino, M. Wiesenfarth, R. Cariou, F. Dimroth, Y. Veschetti, M. Amara, and H. Helmers, "Experimental and simulative correlations of the influence of solder volume and receptor size on the capillary self-alignment of micro solar cells", In early access in the *IEEE Journal of Microelectromechanical Systems*, 2024.
- V. Vareilles, A. Bermudez-Garcia, F. Chabuel, M. Amara, Y. Veschetti, and P. Voarino, "Influence of the thermally induced deflection of a space micro-concentrator photovoltaic array on its optical performances using finite element method," *AIP Conference Proceedings*, vol. 2841, p. 030005, 2023.
- V. Vareilles, P. Voarino, Y. Veschetti, E. Kaiser, H. Helmers and M. Amara, "Manufacturing of a Novel Micro-Concentrator Prototype and Assessment of its Electrical Performances", *13th European Space Power Conference*, (Elche, Spain), 2023.
- E. Kaiser, M. Wiesenfarth, V. Vareilles, M. Schneider-Ramelow, S. Glunz, and H. Helmers, "Forced motion activated self-alignment of micro-CPV solar cells", In early access in the *IEEE Journal of Photovoltaics*, 2023.
- E. Kaiser, M. Wiesenfarth, V. Vareilles and H. Helmers, "Impact of Pad Layout and Solder Volume on Self-Alignment of Micro Solar Cells", Oral presentation at the *24th European Microelectronic Conference*, (Cambridge, United Kingdom), 2023.

Résumé détaillé

Introduction

Historiquement, l'énergie PhotoVoltaïque (PV) a été développée pour les applications spatiales. Le premier satellite alimenté par des cellules photovoltaïques est *Vanguard I*, envoyé dans l'espace en 1958 [2]. Aujourd'hui, les applications spatiales se sont grandement diversifiées, que ce soit à des fins militaires, commerciales ou scientifiques. L'énergie solaire est le mode de production d'énergie prédominant pour les missions proches du soleil, jusqu'à Mars environ. La puissance reçue diminue avec le carré de la distance par rapport au soleil et les missions lointaines ne reçoivent que peu d'énergie. Le secteur spatial connaît à l'heure actuelle une forte hausse de la demande de production d'énergie dans l'espace, avec une problématique de bas coûts prédominante. Les panneaux solaires spatiaux standards sont un assemblage de cellules triple jonction sur une structure composite en sandwich avec une âme en nid d'abeille [14]. Ces cellules sont réalisées en matériaux semi-conducteurs III-V sur germanium. Elles permettent d'obtenir un rendement de conversion de 30% en début de vie ainsi qu'une résistance élevée aux radiations rencontrées dans l'espace. Cependant, leur prix est très élevé (environ 50€/W) et représente environ la moitié du prix total du panneau solaire spatial [16]. Afin de diminuer les coûts, la micro-concentration photovoltaïque (micro-CPV) propose d'utiliser des cellules solaires à haut rendement de taille submillimétrique couplées à un système optique de concentration de la lumière. La quantité de matériau III-V nécessaire est ainsi grandement réduite et permet de diminuer le prix du module pour une même surface de collection de la lumière. La micro-CPV est une approche testée en conditions spatiales lors de différents vols et a prouvé sa fiabilité dans un tel environnement [131]. Cependant, cette technologie doit toujours relever les défis liés au spatial, à savoir les contraintes de masse et de volume des objets envoyés. En effet, le coût de lancement de 1 kg peut s'élever à plusieurs milliers d'euros en fonction de l'orbite. Pour espérer remplacer un module PV standard, un micro-concentrateur doit donc intégrer un système optique compact et léger. Un tel design a été proposé et breveté par le CEA-Liten dans le cadre de la thèse d'A. Bermudez-Garcia en 2020 [43]. Un schéma est présenté en Fig. 6.1. Le système optique du design a été étudié en détail [126]. Ma thèse propose de poursuivre l'étude de ce concentrateur en se concentrant sur des aspects différents. Tout d'abord, du fait de la miniaturisation des cellules solaires, un grand nombre de composants doit être positionné avec précision pour réaliser le concentrateur. Les machines utilisées en micro-électronique pour de telles tâches sont adaptées, mais leur précision dépend de leur rapidité. Afin d'augmenter les cadences de positionnement tout en maintenant une précision élevée, des méthodes de positionnement alternatives sont à l'étude, dont l'auto-alignement. D'autre part, la structure du concentrateur va être soumise à d'importantes contraintes ther-

momécaniques, que ce soit pendant le lancement ou une fois les modules en fonctionnement. En particulier, les panneaux sont soumis à des vibrations et à des variations de température. Du fait de la nature asymétrique de la structure du concentrateur, ces deux phénomènes induisent une courbure, ce qui modifie l'angle d'incidence de la lumière du soleil. Le rendement de conversion du module s'en trouve ainsi diminué. Il convient d'alors d'étudier le comportement de la structure afin de comprendre comment la concevoir de manière à limiter ces effets tout en minimisant sa masse. Enfin, la dernière problématique concerne la fabrication et la caractérisation optoélectrique des premiers prototypes.

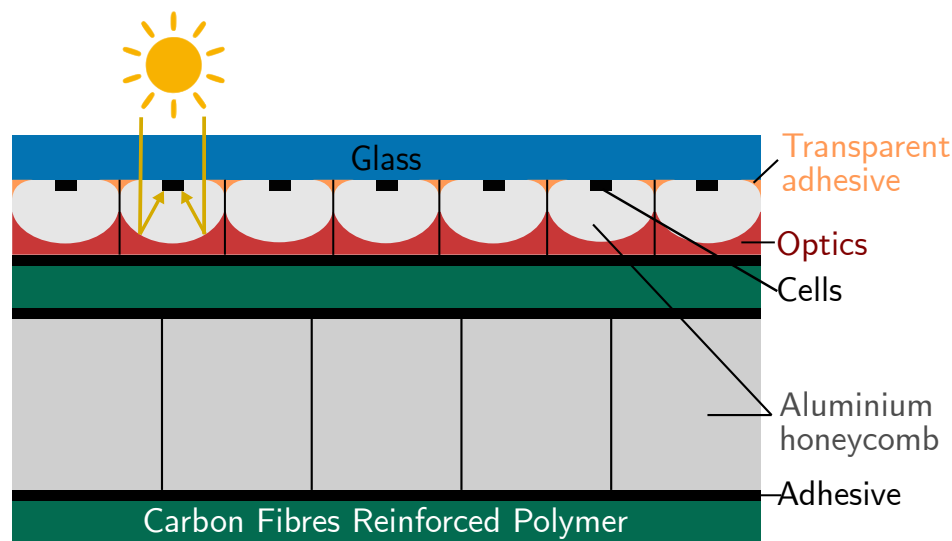


Figure 6.1 : Schéma du design du micro-concentrateur.

Auto-alignement de micro-cellules solaires

Dans le cadre des micro-concentrateurs, les cellules solaires sont généralement positionnées sur leur substrat à l'aide de machines dites de "pick & place". Ces machines peuvent positionner des milliers de composants de taille réduite par heure avec une précision de quelques dizaines de microns. Cependant, elles ne peuvent opérer à leur plus haute vitesse de fonctionnement tout en conservant leur meilleure précision. En effet, les hautes précisions (environ $3\ \mu\text{m}$) sont atteintes grâce à deux étapes de reconnaissance vidéo. La première a lieu lors de la saisie du composant par la machine (étape "pick") pour s'assurer de la manière dont la puce est manipulée par la machine. La seconde s'effectue avant de positionner la puce (étape "place") : la machine vérifie que le bras est positionné au-dessus de l'emplacement souhaité. Il est possible de ne pas effectuer ces étapes de reconnaissance, augmentant la vitesse de positionnement au détriment de sa précision. Afin de diminuer les coûts de fabrication, il est intéressant de conserver une haute précision de placement pour diminuer les pertes optiques dues aux erreurs d'alignement tout en maintenant des cadences de production élevées pour diminuer le temps machine nécessaire à l'assemblage d'un module. Dans cette optique, un état de l'art des procédés d'auto-alignement a d'abord été effectué afin d'identifier la technique la mieux adaptée à la fabrication du micro-concentrateur présenté en introduction. Les contraintes sont

multiples. Le positionnement dans le plan du substrat ainsi que la rotation des cellules doivent être contrôlés pour limiter les pertes optiques. L'utilisation d'un adhésif non-conducteur en face arrière est à proscrire pour ne pas empêcher les connections électriques. Les cellules doivent aussi être fixées définitivement au substrat. Dans le cas des applications spatiales, l'assemblage doit résister à des températures de l'ordre de 100°C. Enfin, le procédé ne doit pas dégrader les performances optiques du substrat en verre, ni augmenter l'ombrage.

Une des approches envisagées est l'auto-alignement, qui désigne un ensemble de technique ayant pour point commun l'assemblage et l'alignement précis de deux solides par eux-mêmes. La méthode retenue est l'auto-alignement par minimisation de la tension de surface (ou auto-alignement capillaire, présenté en Fig. 6.2). Elle a pour avantage de permettre d'atteindre une précision inférieure au micron tout en laissant beaucoup de latitude pour le choix des paramètres du procédé. Afin de répondre aux contraintes de l'application, le choix s'est porté sur l'utilisation d'une brasure fondue. Le procédé d'auto-alignement est alors le suivant :

- Fabrication des pads sur le substrat en verre
- Dépôt de la brasure solide sur les pads
- Positionnement de la cellule sur la brasure
- Refusion : la brasure fond et permet l'auto-alignement

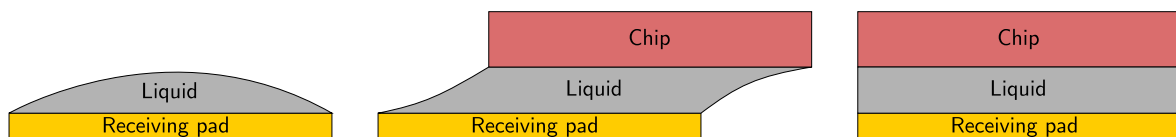


Figure 6.2 : Principe de l'auto-alignement capillaire.

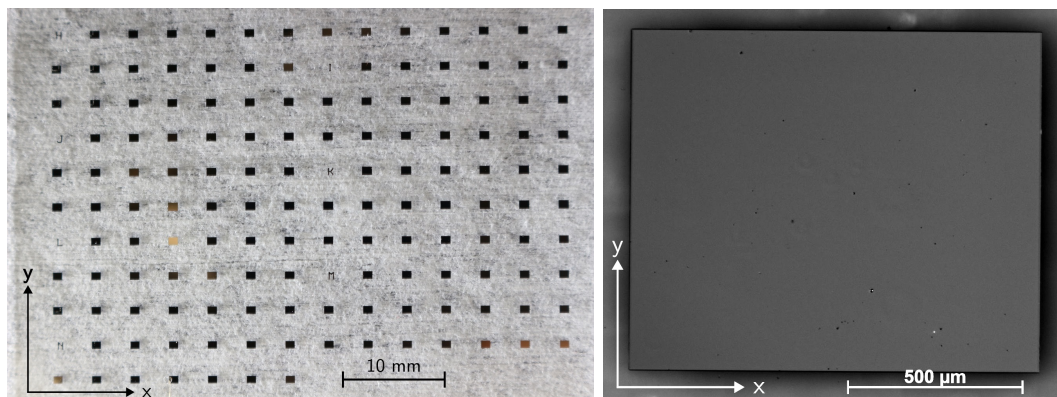
Il est ainsi possible de positionner, fixer et connecter électriquement les cellules en un seul procédé. Le procédé d'auto-alignement capillaire est étudié depuis les années 1990. De nombreuses études sont disponibles sur la forme du pad, son état de surface, les liquides à employer ou encore la forme et dimensions des composants. En revanche, peu de données sont disponibles quant à l'influence du volume de liquide et le placement initial du composant avant refusion. De plus, il est nécessaire de quantifier l'impact de la dimension des pads des cellules utilisées. En effet, les tolérances sur les dimensions des pads par rapport au composant conditionnent le procédé de fabrication utilisable ainsi que les pertes optiques dues aux erreurs d'alignement.

Une campagne expérimentale a été menée au CEA-Leti. Les expériences suivaient le déroulé suivant :

- Nettoyage des substrats avec de l'acétone puis avec de l'isopropanol
- Dépôt d'une crème de brasure SnAg₃Cu_{0.5} (SAC305) par sérigraphie
- Placement des cellules par pick & place
- Refusion

Le but de ces expériences était d'évaluer l'impact du volume de brasure et de la taille des pads, avec des tolérances fines. Pour cela, les pads ont été déposés sur les substrats en verre par

lithographie et évaporation sous vide. Ce procédé permet d'avoir une précision d'un micron sur les dimensions et la position des pads. Les expériences visaient à déterminer l'impact du volume de brasure, du positionnement initial des cellules, de la taille des pads et de la crème de brasure elle-même. Pour cela, deux écrans de sérigraphie ont été utilisés, avec une épaisseur de 100 et 200 μm respectivement pour déposer deux volumes de brasure. Les dimensions des pads correspondaient à la dimension des cellules $\pm 0, 10, 20$ et 50 μm . Deux crèmes de brasure ont été testées, nommées T3 et T6. Elles sont toutes deux composées de particules métalliques et d'un flux, destiné à nettoyer la surface et augmenter la mouillabilité. Les particules de la T6 sont plus petites que celles de la T3. Pour chaque configuration indiquée, 20 cellules ont été positionnées, soit 560 cellules au total. La position finale des cellules a ensuite été caractérisée par traitement d'image avec une résolution d'environ 5 μm . La Figure 6.3 montre une image d'un substrat avec les pads et un gros plan sur un pad individuel.



(a) Photographie d'un substrat. Dimensions des pads comprises entre $835 \times 635 \mu\text{m}$ et $935 \times 735 \mu\text{m}$.

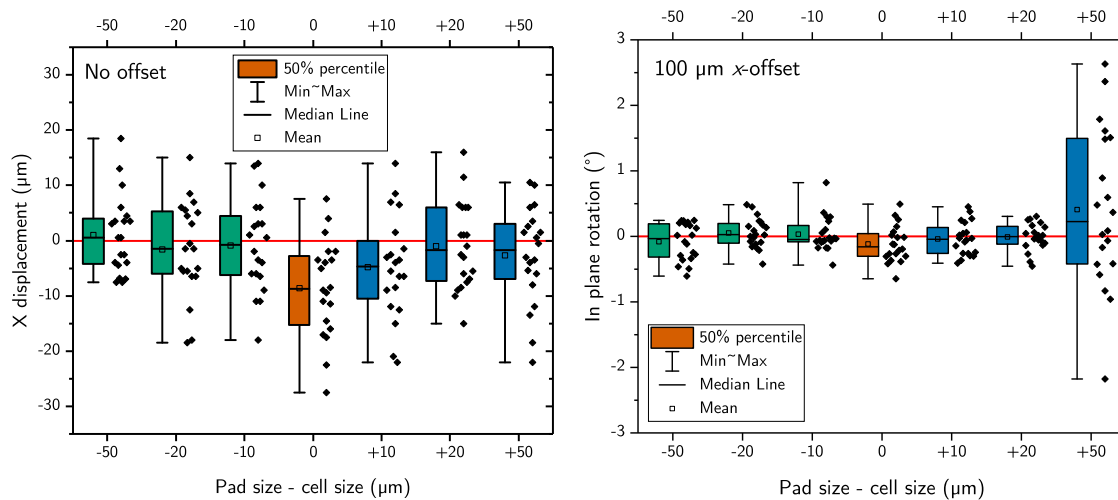
(b) Image microscope d'un pad.

Figure 6.3 : Exemples de plots réalisés par PVD.

En parallèle, un modèle analytique et un modèle numérique ont été développés, pour étudier les forces capillaires s'appliquant sur la cellule lors de l'auto-alignement. Les deux modèles ont donné des résultats concordants, avec un écart relatif d'environ 10% au maximum. Ces études ont mis en avant le rôle important du volume de brasure. Les forces capillaires sont d'autant plus faibles que le volume est important, ce qui décroît la précision d'alignement finale. D'autre part, les forces croissent avec le déplacement de la cellule. De ce fait, un déplacement initial permet d'obtenir des forces élevées dès le début du procédé, ce qui permet de mettre le système en mouvement et améliore également la précision finale. De meilleurs résultats ont été obtenus avec la crème de brasure ayant les particules les plus petites, en raison de sa meilleure mouillabilité. Concernant la taille des pads, les expériences menées au CEA-Liten n'ont pas mis de tendance en évidence. En revanche, les expériences du Fraunhofer ISE ont une précision d'alignement plus élevée lorsque les pads étaient plus petits. De plus, un déplacement initial trop important avait un effet négatif sur l'alignement. La principale hypothèse pour expliquer cet effet repose sur la mouillabilité de la brasure. En effet, pour un même volume de brasure, plus la cellule est éloignée du centre du pad et plus le pad est grand, plus l'angle de mouillage de la brasure est élevé. Ceci entraîne un démouillage pour

des valeurs d'angles trop faibles, inférieures à l'angle de contact théorique. Cependant, des expériences complémentaires seraient nécessaires pour valider cette théorie.

Ces tests ont enfin permis de définir un procédé d'auto-alignement capillaire donnant une précision de positionnement pour 140 cellules de $\pm 35 \mu\text{m}$ concernant les translations dans le plan (Fig. 6.4(a)) et $\pm 1^\circ$ concernant la rotation dans le plan (Fig. 6.4(b)). Une partie de ces résultats est présentée en Fig. 6.4. Il convient d'utiliser l'écran de $100 \mu\text{m}$ d'épaisseur, la crème T6, une tolérance sur la taille des pads de $\pm 20 \mu\text{m}$ et un déplacement initial de $100 \mu\text{m}$. Ces travaux ont fait l'objet de plusieurs communications [132, 100, 99].



(a) Déplacement dans la direction longitudinale de la cellule.

(b) Rotation dans le plan.

Figure 6.4 : Déplacement dans la direction longitudinale de la cellule et rotation dans le plan obtenu avec la crème T6, l'écran de $100 \mu\text{m}$ d'épaisseur et un déplacement initial de $100 \mu\text{m}$.

Influence de la déflexion structurelle sur les performances optiques du concentrateur

En plus des sévères conditions environnementales spatiales, les panneaux solaires doivent faire face aux contraintes additionnelles liées au décollage de l'engin spatial ainsi qu'au déploiement des panneaux. Par ailleurs, des vibrations des panneaux liées à la température sont attendues, dont l'amplitude peut être significative en fonction de la longueur des panneaux. Il n'est malheureusement pas possible d'obtenir des spécifications spatiales définies portant sur la résistance mécanique des panneaux ou le niveau de contraintes attendues. En revanche, en se basant sur l'architecture standard, il est possible de définir une cible de rigidité en flexion à atteindre, correspondant à $5 \times 10^3 \text{N.m}^2$.

Comme détaillé dans la section précédente, le positionnement des cellules sur le verre en face avant du concentrateur est crucial pour réduire les pertes optiques. Un autre point à prendre en considération est l'angle d'incidence de la lumière. L'angle d'acceptance du concentrateur est d'environ 4° , ce qui est compatible avec la précision des trackers, généralement inférieur

à 1°. Cependant, le concentrateur a une structure asymétrique, avec notamment du verre en face avant et un composite en face arrière. Ainsi, les variations de température induisent une courbure de la structure, ce qui entraîne également une augmentation de l'angle d'incidence de la lumière ainsi que des contraintes mécaniques, notamment dans le verre. Maîtriser la courbure d'un concentrateur en vol est donc primordial, d'une part pour limiter les pertes optiques et d'autre part pour éviter l'endommagement des composants, en particulier le verre. Dans le même temps, il convient aussi de minimiser la masse et le volume de la structure afin de limiter les coûts de lancement des panneaux. Les matériaux utilisés pour fabriquer le concentrateur doivent être qualifiés pour les conditions spatiales et il n'y a donc pas de latitude sur leur choix. Il est en revanche possible de soigneusement choisir l'épaisseur des différentes couches qui composent le concentrateur pour modifier sa géométrie. Afin d'atteindre les objectifs énoncés plus haut, le comportement thermomécanique du concentrateur en fonction de sa géométrie est donc étudié. Des tests de flexion ont été réalisés et la courbure en fonction de la température évaluée. Afin de limiter le nombre d'expériences et l'usage de matériaux onéreux, un plan d'expérience a été mis en place au moyen du logiciel d'analyse statistique JMP.

Dans un premier temps, la rigidité en flexion a été étudiée. Le choix de la méthode s'est porté sur des tests 4 points en raison du plus faible niveau de cisaillement pendant l'essai par rapport à des tests 3 points. De plus, les contraintes sont constantes sur une large portion de l'éprouvette de test. En parallèle, un modèle analytique et deux modèles éléments finis (FEM) de ces tests ont été construits. L'un des deux modèles FE prend en compte les frictions liées à l'outillage, l'autre non. Les résultats sont présentés en Fig. 6.5.

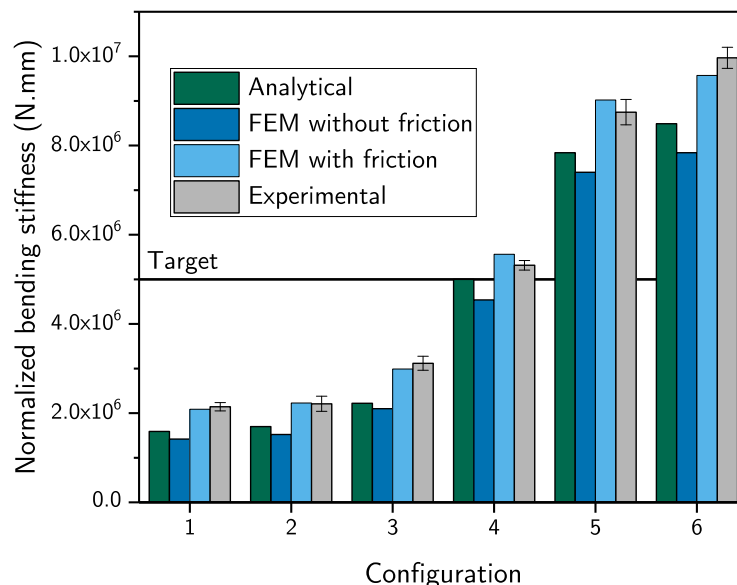


Figure 6.5 : Rigidité en flexion normalisée pour les différentes configurations testées mesurée expérimentalement et déterminée par les modèles analytiques et numériques.

Une différence importante de la rigidité en flexion (30%) entre les résultats expérimentaux et les modèles analytiques et FE sans friction a été observée. Cette différence est due aux

frottements entre l'outillage et les échantillons pendant le test. Une bonne concordance est alors obtenue en rajoutant les frottements dans le modèle FE. Cependant, les modèles analytiques et FE sans friction donnent des résultats similaires, avec un écart relatif de 10% au plus sur la rigidité. A l'inverse des expériences, les simulations permettent d'avoir une idée de la répartition des contraintes mécaniques dans la structure pendant le test. En se basant sur l'ensemble de ces résultats, il est possible de définir la géométrie du concentrateur permettant d'atteindre la cible de rigidité, de répartir les contraintes, limiter celle dans le verre, atteindre la cible de rigidité tout en limitant la masse. Par ailleurs, la répartition des contraintes a indiqué qu'il est nécessaire de considérer les couches composites séparément puisqu'elles n'ont pas la même influence. Ces travaux ont été publiés dans le IEEE Journal of Photovoltaics [133].

Dans un second temps, la déflexion de la structure en fonction de sa géométrie et de la température a été étudiée. Afin de construire le modèle de simulation correspondant, il est nécessaire de connaître le module élastique des matériaux, leur coefficient d'expansion thermique (CTE) ainsi que la température de réticulation des différents polymères, à savoir la résine des composites, les adhésifs composites/nid d'abeille et verre/nid d'abeille. Une série de caractérisations préalables des matériaux constituant le concentrateur a d'abord été réalisée. Les modules élastiques en fonction de la température ont été relevés dans les données constructeurs ou déterminés par test de traction ou analyse mécanique dynamique (DMA). Les CTEs ont été relevés dans les données constructeur ou déterminés expérimentalement par le biais de la mesure de la déflexion de structure bilames. Les températures de réticulation ont été déterminées par mesure calorimétrique différentielle (DSC). Les résultats ont permis de construire un modèle par éléments finis de la courbure du concentrateur en fonction de la température. Les résultats prédits par le modèle ont ensuite été comparés à des mesures expérimentales. Plusieurs structures ont été testées : CFRP/nid d'abeille, CFRP/nid d'abeille double et enfin la structure complète. Les deux premières structures ont montré une déflexion en fonction de la température similaire à celle prédite par le modèle. Par ailleurs, la déflexion était linéaire sur la plage de température étudiée (30-105°C). Cependant, l'écart relatif entre expériences et simulations est plus élevé pour la double structure. La déflexion en fonction de la température de la structure complète est présentée en Fig. 6.6. Le comportement est linéaire pour les basses températures (-50 à 80° environ), puis la pente de la courbe diminue brutalement et la déflexion se stabilise à une valeur différente suivant les éprouvettes. Ce comportement est dû au module élastique de l'adhésif verre/nid d'abeille qui s'effondre à haute température. Il n'assure alors plus son rôle structurel et le verre glisse par rapport au nid d'abeille. Le modèle numérique permet de reproduire cette tendance. En revanche, l'écart entre la déflexion prédite et mesurée est important. Pour un écart de température par rapport à celle de fabrication de 100°C environ, un facteur 2 subsiste entre le modèle et les expériences. Néanmoins, le but de l'étude est principalement d'obtenir les tendances de variations de la courbure liée à la géométrie, pas d'avoir une valeur de courbure bien définie. De plus, l'ordre de grandeur est similaire, il est donc possible d'évaluer si une géométrie est inadaptée. A noter qu'un adhésif ayant une température de fonctionnement supérieur à 100°C serait nécessaire pour une application spatiale afin d'éviter le glissement observé entre le verre

et le nid d'abeille.

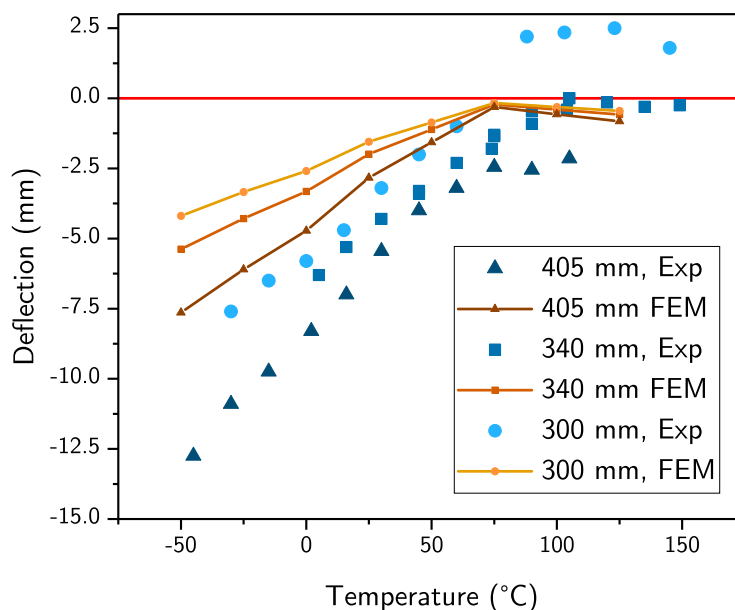


Figure 6.6 : Déflexion expérimentale et calculée avec le modèle par éléments finis pour la structure complète et trois tailles d'éprouvette différentes.

A l'aide d'un nouveau plan d'expérience réalisé avec le modèle de simulation numérique, la déflexion de la structure en fonction de la température et de sa géométrie a alors pu être étudiée. Les variables choisies étaient les mêmes que pour l'étude de rigidité, cependant les couches composites ont été considérées séparément comme préconisé plus haut. De nouveau, le design a été optimisé afin de limiter la courbure, la contrainte dans le verre et la masse. En prenant en compte les deux études (rigidité et courbure), les géométries du concentrateur les mieux adaptées ont été déterminées, c'est à dire celles permettant d'atteindre la cible de rigidité tout en conservant une courbure, un niveau de contrainte dans le verre et une masse faible. En considérant des matériaux spatiaux, il est cependant difficile d'estimer la masse réelle du système. De plus, la longueur maximale de panneau admise afin de ne pas dépasser l'angle d'acceptance des optiques (4.2°) à ces extrémités a été définie pour les configurations choisies. Un résumé des résultats est présenté en Table 6.1.

t_{Nb} (mm)	t_{Nt} (mm)	t_g (mm)	t_{ct} (mm)	t_{bt} (mm)	$i(L = 2m)$ (°)	$L(i = 4.2^\circ)$ (m)	D ($N.m^2$)
15	3	0.1	0.2	0.8	3.3	2.5	8×10^3
20	3	0.1	0.2	0.8	3.0	2.7	14×10^3
20	3	0.3	0.2	0.8	2.4	3.7	19×10^3

Table 6.1 : Pour trois géométries, angle d'incidence maximum pour un panneau de 2 m et longueur maximale pour un angle d'incidence inférieur à 4.2° .

Dans les trois cas, la cible de rigidité est largement atteinte et le verre est en compression avec une contrainte ne dépassant pas -75 MPa. La taille de panneau maximale est compatible

avec le standard, dépassant 2 m. Cependant, des pertes optiques sont à prévoir dans tous les cas, il serait intéressant de développer des méthodes afin d'obtenir un panneau plan en fonctionnement pour améliorer les performances électriques du concentrateur. Ces travaux ont fait l'objet d'une communication à la conférence CPV-18 en 2023 [113].

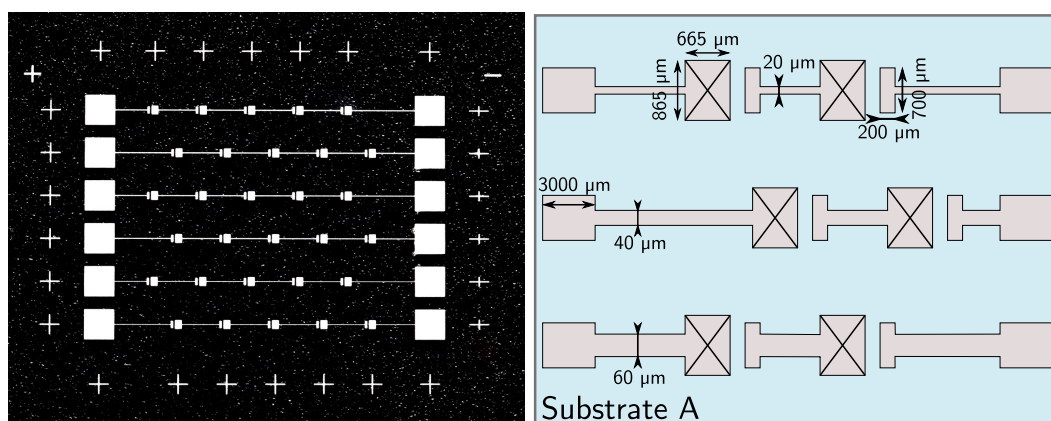
Fabrication et caractérisation opto-électrique de prototypes

Après avoir étudié une méthode de positionnement et d'assemblage des micro-cellules solaires et l'influence de la géométrie de la structure sur les performances optiques du concentrateur, le dernier objectif de la thèse est de fabriquer et caractériser un prototype du micro-concentrateur. La partie structure et optique est fabriquée indépendamment de la partie substrat.

La structure nid d'abeille composite carbone est d'abord laminé à 150°C. Ensuite, les optiques en silicone sont moulées à l'intérieur des cellules du nid d'abeille. La silicone liquide est mise sous vide pour la dégazer afin d'éviter la formation de bulles. Elle est maintenue à la forme parabolique désirée à l'aide d'un moule en acier inoxydable. La réticulation est faite à température ambiante. Puis, une couche réfléchive en argent est déposée par évaporation sous-vide. Afin d'obtenir une bonne qualité de la couche, les optiques en silicone sont préalablement placées sous vide pendant au moins 72h pour les dégazer.

Les substrats sont fabriqués en parallèle des optiques. Tout d'abord, les pistes électriques sont réalisées par sérigraphie avec une pâte d'argent. Cette technique est utilisée pour sa bonne précision géométrique. Lors du retrait de l'écran, la pâte de sérigraphie s'affaisse et dépasse d'environ 40 μm du motif original. Les motifs de l'écran sont donc conçus en prenant en compte cet affaissement.

Différents designs d'interconnexions ont été conçus. Le design A est présenté en Fig. 6.7 et comporte des pistes électriques de différentes largeurs (20, 40 et 60 μm) pour tester les effets de résistance série. Chaque piste connecte cinq cellules en série.



(a) Photographie d'un substrat de design A. (b) Schéma des principales caractéristiques du design A.

Figure 6.7 : Exemple de substrat de design A.

Le design B est constitué d'une seule cellule pour faciliter les caractérisations et permettre une étude de tolérancement. Le design C comporte six strings en parallèle. Chaque string est constitué de cinq cellules en série. Le design D a des interconnexions similaires. En revanche, les pistes électriques sont remplacées par des fils pour diminuer l'ombrage. Une brasure SAC305 est ensuite déposée sur les plots par un système de dispense en pression. Les cellules sont par la suite placées par pick & place. L'ensemble passe alors dans un four pour refusion. L'étape suivante est de connecter la face avant des cellules aux pistes en argent. Ceci est réalisé par wire-bonding, procédé qui consiste à souder un fil d'or de 25 μm en appliquant une pression et une force ultrasonique. Il n'a cependant pas été possible de souder les fils directement sur les fils en argent. En effet, l'argent s'oxyde et la pâte est friable. Il a ainsi été nécessaire de découper puis de braser des morceaux de métal avec un revêtement en or sur les pistes. Les fils ont été soudés entre les cellules et ces morceaux. Un exemple de wire-bonding est visible dans la Figure 6.8 pour le substrat A (à gauche) et le substrat D (à droite).

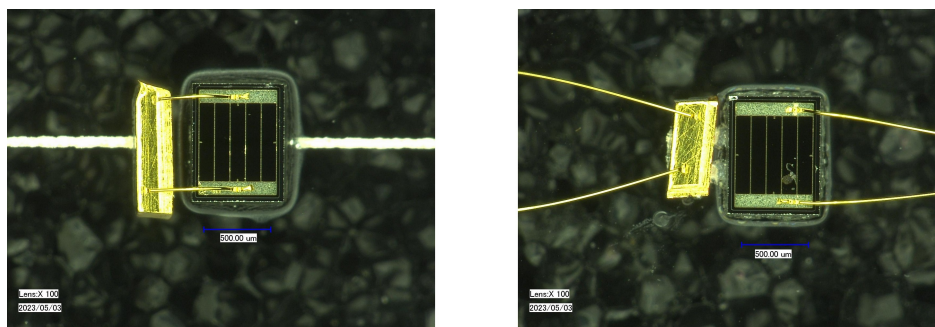


Figure 6.8 : Photographie d'une interconnexion par wire-bonding pour les designs A, B, C (à gauche) et D (à droite).

Une photographie de l'ensemble optique/substrat est présentée en Fig. 6.9.

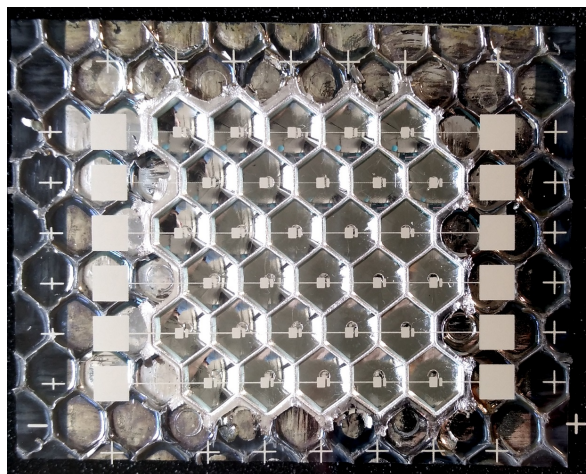


Figure 6.9 : Photographie d'un ensemble substrat-optiques. Le substrat est ici simplement posé sur le réseau de miroir.

Afin d'évaluer les pertes résistives liées à la largeur des pistes électriques, des mesures courant-tension sous obscurité (DIV) ont été réalisées. Une différence de résistance série est

visible pour les lignes de 20 μm à partir de 2 mA. Cette valeur est proche du courant attendu pour une cellule en conditions spatiales. Cette différence s'accroît à mesure que le courant augmente. En revanche, il ne semble pas y avoir de différence notable entre les lignes de 40 et 60 μm . Les lignes de 40 μm semblent donc être un bon compromis entre ombrage et pertes résistives.

Les caractéristiques I-V des substrats B (1 cellule), C (30 cellules) et D (25 cellules) seuls ont été mesurées en intérieur. La mesure n'était pas calibrée, l'irradiance exacte n'est pas connue. En revanche, il est possible de comparer les substrats entre eux. La densité de courant est identique pour les 3 substrats, les différentes interconnexions n'ont pas d'influence sur cette caractéristique. Le facteur de forme est élevé, entre 84 et 89%. En revanche, le substrat C a une tension de circuit ouvert plus faible que celle attendue d'environ 2 V. Ceci est dû à la présence d'un shunt sur un des strings de cellules.

Les performances électriques du concentrateur avec 1 cellule (design B) et 30 cellules (design C) ont été mesurées en extérieur. Le substrat et les optiques étaient montés sur un jeu de trois platines micrométriques afin de contrôler leur alignement. L'ensemble était lui-même placé sur un tracker deux axes au Fraunhofer ISE. Un rendement de conversion de 21% a été obtenu avec le substrat B en prenant en compte l'irradiance directe uniquement (Fig. 6.10).

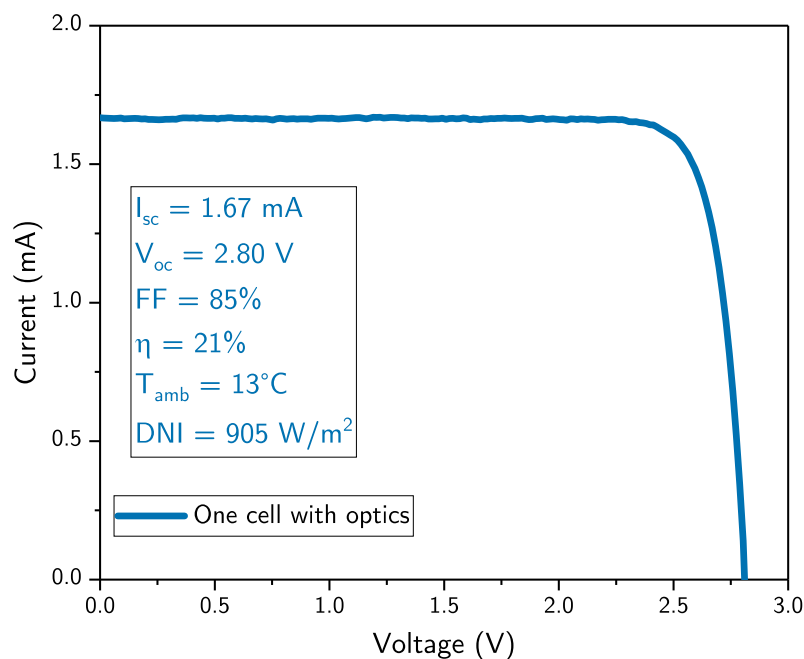


Figure 6.10 : Courbe courant tension pour le substrat B mesurée à l'extérieur le 21 avril 2023 à Freiburg en Allemagne.

A l'aide des platines micrométriques, une étude de l'impact du désalignement cellule-optique a été conduite. Les résultats sont visibles en Fig. 6.11. Pour les translations dans le plan du substrat, la petite direction des optiques est la plus critique. Un déplacement de 150 μm conduit à 10% de pertes de courant, contre 200 μm pour la grande direction. En considérant les tolérances d'auto-alignement obtenu dans le chapitre correspondant ($\pm 35 \mu\text{m}$),

les pertes optiques dues au désalignement ne dépassent pas 3%. La translation hors-plan a un impact plus fort encore. Un déplacement de 100 μm est suffisant pour atteindre le même niveau de perte. L'épaisseur de brasure sous la cellule et de l'adhésif utilisé pour fixer le substrat en verre sur le nid d'abeille est donc à contrôler minutieusement.

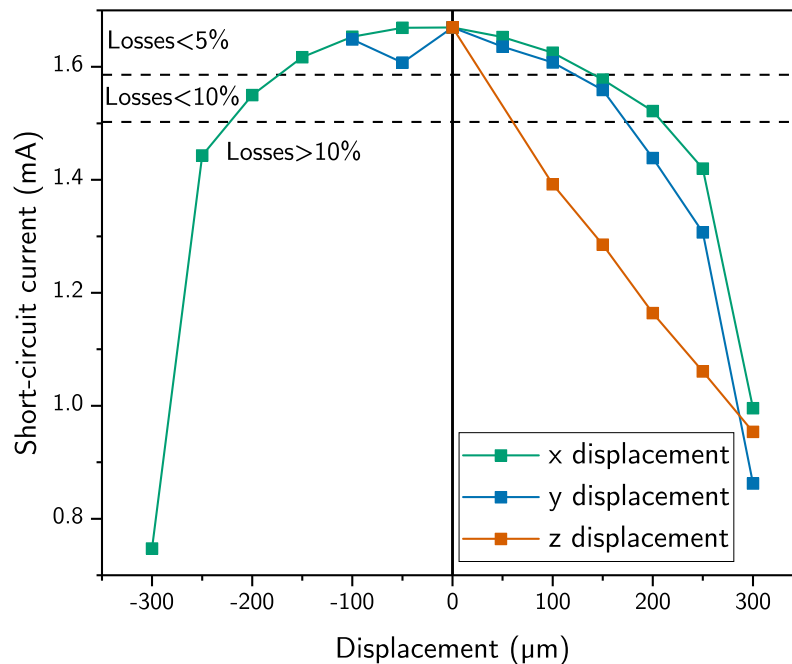


Figure 6.11 : Influence de la position de la cellule par rapport à l'optique sur le courant de court-circuit du design B. Les mesures ont été effectuées le 21 avril 2023 à Freiburg en Allemagne.

La caractérisation du substrat C s'est avérée difficile en raison de l'absence de contrôle de la rotation du substrat par rapport aux optiques. Faute de pouvoir aligner correctement l'ensemble des cellules avec les miroirs, le courant mesuré est bien plus faible qu'attendu. Comme indiqué précédemment, la tension est également plus faible. Néanmoins le rendement maximum obtenu était de 12.7% pour ce substrat C.

Pour déterminer des pistes d'amélioration des performances électriques, une première étude des pertes optiques avaient été réalisée par A. Bermudez-Garcia *et al* [126]. Le rendement optique théorique estimé était de 74%. Les prototypes ayant été fabriqués au cours des travaux présentés ici, une estimation plus précise des pertes optiques était possible, notamment concernant l'ombrage. L'ombrage tel que définie par le design est l'ombrage réel mesuré est détaillé dans la Fig. 6.12. L'ombrage dû aux parois du nid d'abeille, du pad d'accueil cellule, des pistes électriques et du pad nécessaire au wire-bonding a été déterminé par trois méthodes. La première consistait à utiliser les dimensions telles que conçues, la seconde à utiliser les dimensions mesurées au profilomètre et la dernière reposait sur un traitement d'image. Les résultats sont présentés en Fig. 6.12. L'ombrage est compris entre 8 et 9.2%. L'ombrage réel est comme attendu plus élevé que l'ombrage conçu. En particulier, les parois du nid d'abeille causent plus d'ombrage qu'attendu et en représente environ la moitié. La deuxième cause la

plus importante est le pad d'accueil cellule, qui ne peut pas être plus petit à moins d'utiliser des cellules plus petites. Les lignes de 20 μm de large permettent de gagner un peu d'ombrage mais augmente les pertes résistives et sont fragiles, les lignes de 40 μm leur sont préférables. Remplacer les lignes conductrices par des fils (design D) ne permet de diminuer l'ombrage de 0,7% environ mais rend la fabrication plus difficile.

Par ailleurs, les pertes optiques dues au miroir en argent ont été estimées en se basant sur la réflectivité mesurée d'une couche d'argent déposée sur un substrat plat en silicone. La réflectivité de 80.8% est bien plus faible que l'état de l'art (95%), le dépôt n'ayant pas été optimisé au cours de ces travaux. En appliquant un revêtement anti-réfléctif sur le verre, en affinant les parois du nid d'abeille et en utilisant un revêtement d'argent de meilleure qualité, il est possible d'améliorer le rendement optique jusqu'à 77%.

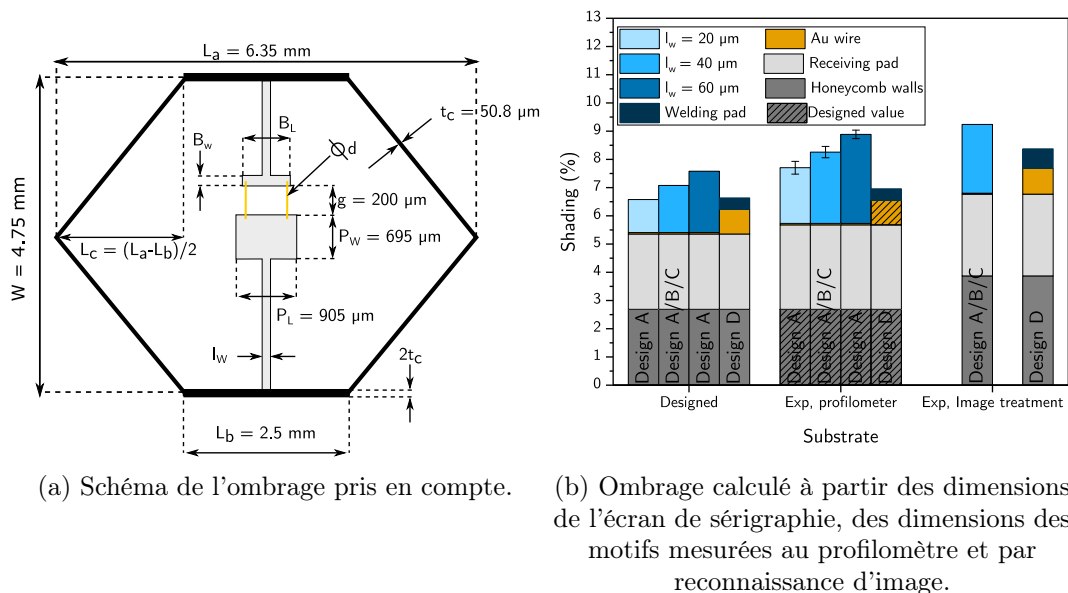


Figure 6.12 : Schéma de l'ombrage considéré (gauche) et valeurs calculées (droite).

Conclusion et perspectives

Les applications spatiales requièrent de plus en plus d'énergie électrique pour la propulsion, les constellations de satellites et les missions d'exploration en espace lointain. La micro-concentration photovoltaïque peut être une solution pour fabriquer des générateurs solaires hautement performants en diminuant l'usage des cellules solaires à base de matériaux III-V extrêmement coûteux. Prometteuse, cette technologie doit relever les défis posés par les contraintes de masse et de volume dans l'espace. Cette thèse s'articule autour d'un micro-concentrateur innovant, basé sur un réseau de miroirs hexagonaux intégrés dans un nid d'abeille. Les cellules solaires sont fixées sur un substrat en verre placé sur le réseau optique. Cet assemblage est monolithique, compact et léger.

Cependant, l'assemblage avec un positionnement à quelques dizaines de microns de milliers de micro-cellules représente un défi. La précision requise est importante et le temps

d'assemblage doit être le plus faible possible pour diminuer les coûts. Pour ce faire, l'auto-alignement capillaire est une solution prometteuse, étudiée également pour les applications micro-électroniques. Ensuite, la structure du concentrateur, asymétrique, va être soumise à des contraintes thermiques et mécaniques. En particulier, le concentrateur va se courber avec les changements de température, modifiant l'angle d'incidence de la lumière et diminuant les performances optiques. De plus, le substrat en verre portant les cellules pourrait être endommagé par les contraintes. Dans cette optique, il est important de bien comprendre le comportement thermomécanique de la structure pour éviter ces écueils.

Enfin, la fabrication du micro-concentrateur en elle-même comporte de nombreux défis et chacune des étapes nécessitent d'être précisément définie au vu des faibles dimensions du dispositif. Les objectifs de cette thèse étaient donc les suivants :

- Comprendre les mécanismes limitant l'auto-alignement capillaire
- Identifier les moyens d'amélioration de ce procédé
- Comprendre l'influence de la géométrie de la structure du concentrateur sur sa rigidité en flexion et sa courbure en fonction de la température
- Définir des directives de conception afin de minimiser la courbure, les contraintes mécaniques dans le verre et la masse de l'ensemble
- Fabriquer les premiers prototypes du design en définissant les techniques nécessaires
- Réaliser les premières caractérisations électro-optiques du micro-concentrateur

Tout d'abord, l'auto-alignement capillaire des micro-cellules a fait l'objet d'une étude en collaboration avec le Fraunhofer ISE. Une campagne expérimentale a été effectuée afin d'étudier l'influence du volume de brasure utilisé, de la taille des pads d'accueil cellule et du positionnement initial de la cellule. D'autre part, des modèles de simulations analytique et numérique des forces capillaires s'appliquant sur la cellule durant l'auto-alignement ont été développés. L'ensemble a permis de mettre en lumière le rôle du volume de brasure, qui en augmentant diminue fortement les forces capillaires, diminuant la précision d'alignement. Par ailleurs, la taille des pads n'a pas eu d'influence significative sur les expériences du CEA-Liten. En revanche, des pads plus petits ont donné de meilleurs résultats pour le Fraunhofer ISE. Cette différence est à l'heure actuelle expliquée par un démouillage possible sur des pads trop grands, bien que des études complémentaires soient nécessaires pour confirmer cette hypothèse. D'autre part, un déplacement initial des cellules de 100 μm donne une meilleure précision d'alignement et une plus faible dispersion des résultats. Ceci est dû aux forces capillaires étant plus élevées au début du procédé. Cependant, un déplacement initial trop important finit par diminuer grandement la précision de l'alignement. Au final, une précision d'alignement de $\pm 30 \mu\text{m}$ a été obtenue pour 140 cellules positionnées, avec une rotation dans le plan inférieure à 1° à l'exception des 20 cellules placées sur les plus grands pads.

Dans un second temps, le comportement thermomécanique a fait l'objet de deux études. La première portait sur la rigidité en flexion de la structure et la deuxième sur la courbure en fonction de la température. Dans les deux cas, des expériences et des simulations ont été réalisées afin de déterminer l'influence de la géométrie du concentrateur sur sa rigidité, sa

courbure, la répartition des contraintes et sa masse. Des plans d'expériences ont été construits afin de limiter le nombre d'essais ou le temps de calcul. Dans le cas de l'étude de rigidité en flexion, les simulations des tests de flexion 4-points ont permis de mettre en évidence une surestimation des valeurs mesurées expérimentalement due aux frottements entre l'outillage et les éprouvettes. De plus, un modèle analytique simple adaptable à de multiples structures sandwichs a été développé. Dans le cas de l'étude de la courbure, de nombreuses caractérisations matériaux ont été nécessaires afin de construire un modèle simulant la courbure du concentrateur en fonction de la température. Le modèle présente un écart important avec les expériences, mais permet tout de même d'évaluer les tendances. En prenant en compte les résultats des deux études, des directives de conception ont été établies. Les géométries les plus intéressantes au regard des objectifs mentionnés plus haut ont été déterminées. La longueur maximale de panneau à ne pas dépasser de manière à ce que l'angle d'incidence ne dépasse pas l'angle d'acceptance du système optique a aussi été calculée. Finalement, les géométries retenues sont compatibles avec des panneaux de 2 à 4 m environ, ce qui est cohérent avec les standards spatiaux.

Enfin, les premiers prototypes du micro-concentrateur ont été fabriqués et caractérisés. Les pads d'accueil cellule et les pistes électriques sont déposées par sérigraphie sur le substrat en verre. Différents designs d'interconnexions ont été testés afin d'évaluer les pertes optiques et résistives dues aux pistes électriques. Une largeur de 40 μm a été retenue pour obtenir un compromis ombrage/résistance mécanique/résistance électrique. Des caractérisations électriques en extérieur ont pu être réalisées au Fraunhofer ISE. Un rendement de conversion de 21% a été obtenu avec un design comportant une seule cellule connectée et une optique, en considérant l'irradiance directe mesurée et la surface d'une optique. L'étude du courant de court-circuit du dispositif en fonction du désalignement cellule/optique a montré une haute tolérance aux translations dans le plan. Un désalignement de 30 μm , correspondant à la précision d'auto-alignement, n'entraîne des pertes optiques que de 3% environ. L'étude des pertes optiques a montré que le rendement optique du module actuel est d'environ 60% et pourrait être amélioré de manière à atteindre 77% en ajoutant un revêtement anti-réfléctif, en diminuant l'ombrage et en améliorant le revêtement réfléchissant du miroir. Ces travaux ont fait l'objet d'une présentation orale à la conférence ESPC en 2023 et de la publication d'actes associés [134].

En perspectives, la caractérisation électrique des prototypes est difficile à l'échelle multicellule. Un moyen de contrôler la rotation du substrat devrait être intégré pour ce type de mesure. De plus, l'alignement est long et probablement imparfait. Un moyen d'aligner rapidement le verre et la structure devra être développé. Concernant la fabrication des substrats portant les cellules, la fiabilité des pistes de sérigraphie et des interconnexions par wire-bonding est à tester, notamment en cyclage thermique. Par ailleurs, le wire-bonding peut être considéré comme trop lent au vu de la densité de cellules à connecter et une autre méthode serait préférable. Par exemple, des techniques basées sur la sérigraphie d'encres conductrices sont envisageables. Les aspects thermiques de la structure n'ont été que partiellement étudiés.

En particulier, le modèle de la déflexion n'incluait qu'un chargement thermique simplifié, il est nécessaire de s'intéresser à la température dans toute la structure afin de mieux prévoir la courbure du concentrateur en vol. D'autre part, la température en fonctionnement de la cellule doit être déterminée pour s'assurer qu'elle est acceptable. Enfin, l'auto-alignement capillaire est une technique intéressante pour l'assemblage de composants. Les simulations seules n'ont pas permis de trancher définitivement sur l'intégralité des phénomènes observés expérimentalement. Des expériences complémentaires sont nécessaires pour valider les hypothèses avancées.



FOLIO ADMINISTRATIF

THESE DE L'INSA LYON, MEMBRE DE L'UNIVERSITE DE LYON.

NOM : VAREILLES

DATE de SOUTENANCE : 15/12/2023

Prénoms : Victor

TITRE : Micro-concentrateur photovoltaïque hautement intégré pour les applications spatiales

NATURE : Doctorat

Numéro d'ordre : 2023ISAL0106

Ecole doctorale : 160 EEA

Spécialité : Électronique, micro et nanoélectronique, optique et laser

RESUME : Les applications spatiales requièrent de plus en plus d'énergie électrique pour la propulsion, les constellations de satellites et les missions d'exploration en espace lointain. La micro-concentration photovoltaïque peut être une solution pour fabriquer des générateurs solaires hautement performants en diminuant l'usage des cellules solaires à base de matériaux III-V extrêmement coûteux. Prometteuse, cette technologie doit relever les défis posés par les contraintes de masse et de volume dans l'espace. Cette thèse s'articule autour d'un micro-concentrateur innovant, basé sur un réseau de miroirs hexagonaux intégrés dans un nid d'abeille. Les cellules solaires sont fixées sur un substrat en verre placé sur le réseau optique. Cet assemblage est monolithique, compact et léger. La première partie détaille l'auto-alignement capillaire nécessaire pour positionner à quelques dizaines de microns plusieurs dizaines de milliers de micro-cellules par mètre carré. Des simulations validées par l'expérience sont effectuées pour déterminer l'influence du volume de liquide, de la taille des récepteurs et du positionnement initial des cellules, permettant d'atteindre une précision inférieure à 30 μm . La deuxième partie se consacre au comportement mécanique du composite sous contrainte thermique. Un modèle par éléments finis permet de concevoir un micro-concentrateur en limitant sa courbure tout en minimisant sa masse. Enfin, la troisième partie met en avant les différentes étapes de fabrication du prototype et notamment la réalisation des récepteurs déposés par sérigraphie sur le verre support, l'interconnexion des cellules et leur brasure. Un premier rendement d'un mono-module de 21 % a été obtenu sous une irradiance directe de 903 W/m^2 à une température ambiante de 13°C. Pour une erreur de positionnement de 50 μm de la cellule par rapport à l'optique, les pertes n'excèdent pas 5 %.

Ce travail peut s'appliquer également aux modules photovoltaïques terrestres à base de composite, et de connectiques électriques spécifiques sur substrat verre.

MOTS-CLÉS : Micro-concentrateur, photovoltaïque, espace

Laboratoire (s) de recherche : CEA-Liten & INL

Directeur de thèse: Mohamed AMARA

Président de jury : Samuel Rivallant

Composition du jury : Yvan Cuminal (Rapporteur), Anne Kaminski-Cachopo (Rapporteuse), Samuel Rivallant (Examinateur), César Dominguez-Dominguez (Examinateur), Mohamed Amara (Directeur de thèse), Yannick Veschetti (Co-directeur de thèse)

